Application of the authigenic $^{10}Be/^{9}Be$ dating to constrain the age of a long-lived lake and its regression in an isolated intermontane basin: The case of Late Miocene Lake Turiec, Western Carpathians

Michal Šujan[1,*], Kishan Aherwar[1], Rastislav Vojtko[1], Régis Braucher[2], Katarína Šarinová[3], Andrej Chyba[4], Jozef Hók[1], Anita Grizelj[5], Radovan Pipík[6], Bronislava Lalinská - Voleková[7], Barbara Rózsová[1], Aster Team[2,**]

1 – Department of Geology and Paleontology, Faculty of Natural Sciences, Comenius University in Bratislava, Ilkovičova 6, 842 15 Bratislava, Slovakia; michal.sujan@uniba.sk

2 – CNRS-IRD-Collège de France-INRAE, CEREGE, Aix-Marseille Univ., 13545 Aix-en-Provence, France; braucher@cerege.fr

3 – Department of Mineralogy, Petrology and Economic Geology, Faculty of Natural Sciences, Comenius University in Bratislava, Ilkovičova 6, 842 15 Bratislava, Slovakia; katarina.sarinova@uniba.sk

4 – Institute of Chemistry, Slovak Academy of Sciences, Dúbravská cesta 9, 845 38 Bratislava, Slovakia; andrej.chyba@savba.sk

5 – Croatian Geological Survey, Sachsova 2, 10 000 Zagreb, Croatia; agrizelj@hgi-cgs.hr

6 – Earth Science Institute, Slovak Academy of Sciences, Ďumbierska 1, 97411 Banská Bystrica, Slovakia; pipik@savbb.sk

7 – SNM-Natural History Museum, Vajanského náb. 2, P.O. BOX 13, 810 06 Bratislava, Slovakia; bronislavalalinska@gmail.com

* – corresponding author

** – AsterTeam: Georges Aumaître, Karim Keddadouche, Fawzi Zaidi

The manuscript is a preprint submitted to EarthArXiv.

The manuscript is a pre-proof peer reviewed version, which has been accepted on 24 July 2023 in the Palaeogeography, Palaeoclimatology, Palaeoecology journal.

Journal version: https://doi.org/10.1016/j.palaeo.2023.111746

Abstract

The depositional record of intermontane basins provides a valuable archive of the temporal evolution of orogenic belts; their common isolated nature may, however, hinder the efficient usage of standard approaches to constrain the age of a basin fill. In this paper the authigenic $^{10}Be/^{9}Be$ dating method is employed and tested to construct an age model of the existence and regression of Lake Turiec, which appeared during the Late Miocene in the intermontane Turiec Basin, Central Western Carpathians (Central Europe). The initial authigenic $^{10}Be/^{9}Be$ ratio, essential for the dating method, was analyzed on five sites of the Pleistocene-Holocene age, and back-calculation of the paleo-initial ratio was performed using lacustrine succession dated by magnetostratigraphy. Noteworthy, the initial ratio appears to be affected mainly by (post)depositional settings, and not by different provenance of the analyzed sediment. The sedimentological analysis of the Upper Miocene outcrops allowed the definition of the facies associations of an alluvial fan, a braided river, a fan delta and an open lake. The distribution of facies associations in the basin fill implies an increase in sediment supply to accommodation rate ratio due to the replacement of the open lake environment by the interconnected alluvial fan-braided river-fan delta system. Authigenic $^{10}Be/^{9}Be$ dating yielded ages of the lacustrine succession reaching ~10.7–7.8 Ma, while the age of the fan delta succession, considered as the timing of the regression, was established to ~6.7 Ma. The deposition of alluvial fans dominated the basin after the regression of the lake, possibly up to ~4.0 Ma. The abrupt increase in sediment supply to the accommodation ratio at ~6.7 Ma was caused by the uplift of the Malá Fatra Mts. at the western margin of the Turiec Basin, which had previously formed a moderate topography. The timing of this process generally coincides with the overall decrease in accommodation rates in the region due to the inversion of the Pannonian Basin System. The endorheic character of the basin before ~6.7 Ma prevented the transport of the sediment denudated from the recently most uplifted parts of the Western Carpathians and carried towards the Pannonian Basin System, while the present-day source-to-sink system could only be formed later. This implies a low sediment supply and restricted denudation rate not only from the morphostructures surrounding the basin, but also from the Tatra Mts. and Nízke Tatry Mts. during the period ~10.0–6.7 Ma. The research supports the suitability of intermontane basins for authigenic $^{10}Be/^{9}Be$ dating in a setting of high accommodation rates and limited redeposition of older muddy sediment. However, a special attention has to be paid to the depositional settings during determination of initial $^{10}Be/^{9}Be$ ratios.

Keywords: cosmogenic nuclides, authigenic $^{10}Be/^{9}Be$ dating, facies analysis, lake regression, Western Carpathians, paleoenvironment

1. Introduction

Intermontane basins comprise an essential part of the structure of orogenic belts worldwide (e.g., Burbank, 1983; Gibling et al., 1985; Chaimov et al., 1992; Streit et al., 2017; Paknia et al., 2021). Their formation mirrors changes in the geodynamic phases of orogenic belts, which are recorded by the lithology and geometry of the resulting sedimentary fill of the basins. The analysis of such basin fill is therefore potentially the source of a wealth of information for geodynamic, paleogeographic and morphotectonic studies.

A position in the interior of an orogen may lead to the establishment of an endorheic drainage pattern and a decrease in precipitation caused by orographic rainfall barriers (Sobel et al., 2003; Trexler et al., 2012). Low precipitation and high uplift rates enhance the formation of an internal drainage and thus reduce the connectivity of an intermontane basin with a drainage network of

the orogenic belt and foreland (Sobel et al., 2003; Garcia-Castellanos, 2006). On the other hand, an outflowing lake connected with the regional drainage and underfilled with sediment could form, but its persistency is limited by potential breakage of topographic barriers, especially in humid conditions, limited water depth and low uplift rates of its margins (Sobel et al., 2003; Bridgland et al., 2020; Freitas et al., 2022).

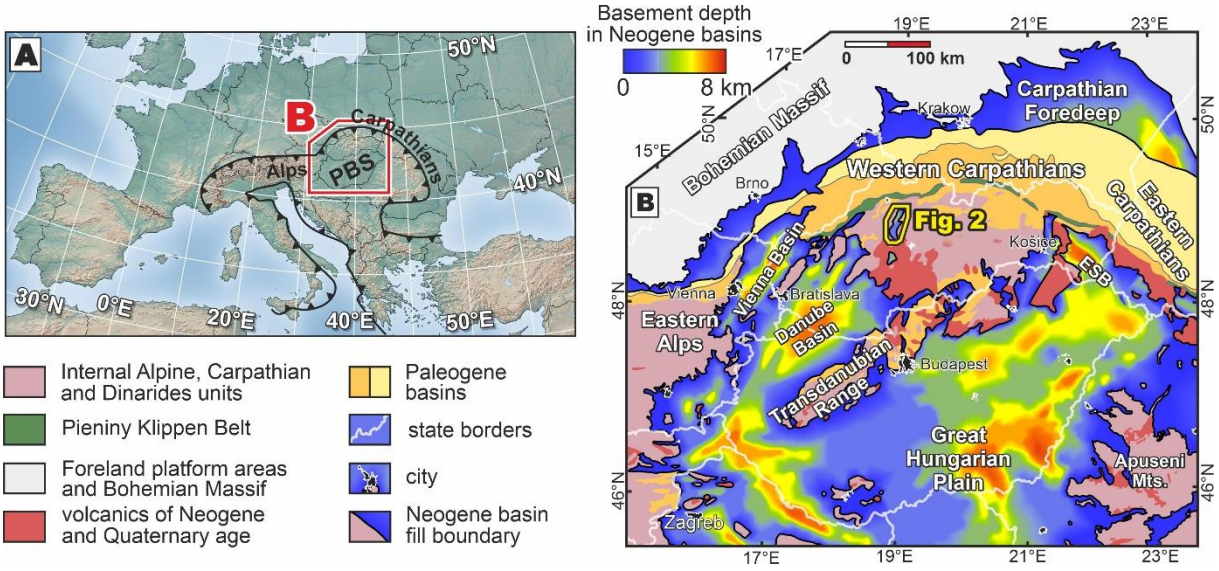

Fig. 1. Location of the Turiec Basin. A: Location within the Alpine-Carpathian orogen in Central Europe. B: The Turiec Basin in the Central Western Carpathians. The map is modified from Šujan et al. (2021b).

Another major factor related to the role of an intermontane basin in the drainage network of an orogenic belt is the redistribution of sediment and its transient storage. The depositional record of such a basin provides a valuable archive of changes in the drainage of rivers, which in turn affects the switching of provenance in the more distal settings of foredeep and back-arc basins. Moreover, the connectivity of an intermontane basin with the regional drainage network exerts a first-order control factor over its accommodation rates, since endorheic periods cause increased sediment storage due to the local base-level rise, while the re-establishment of connectivity is followed by incision and sediment removal (Schildgen et al., 2016; Geurts et al., 2018; Ballato et al., 2019; Paknia et al., 2021).

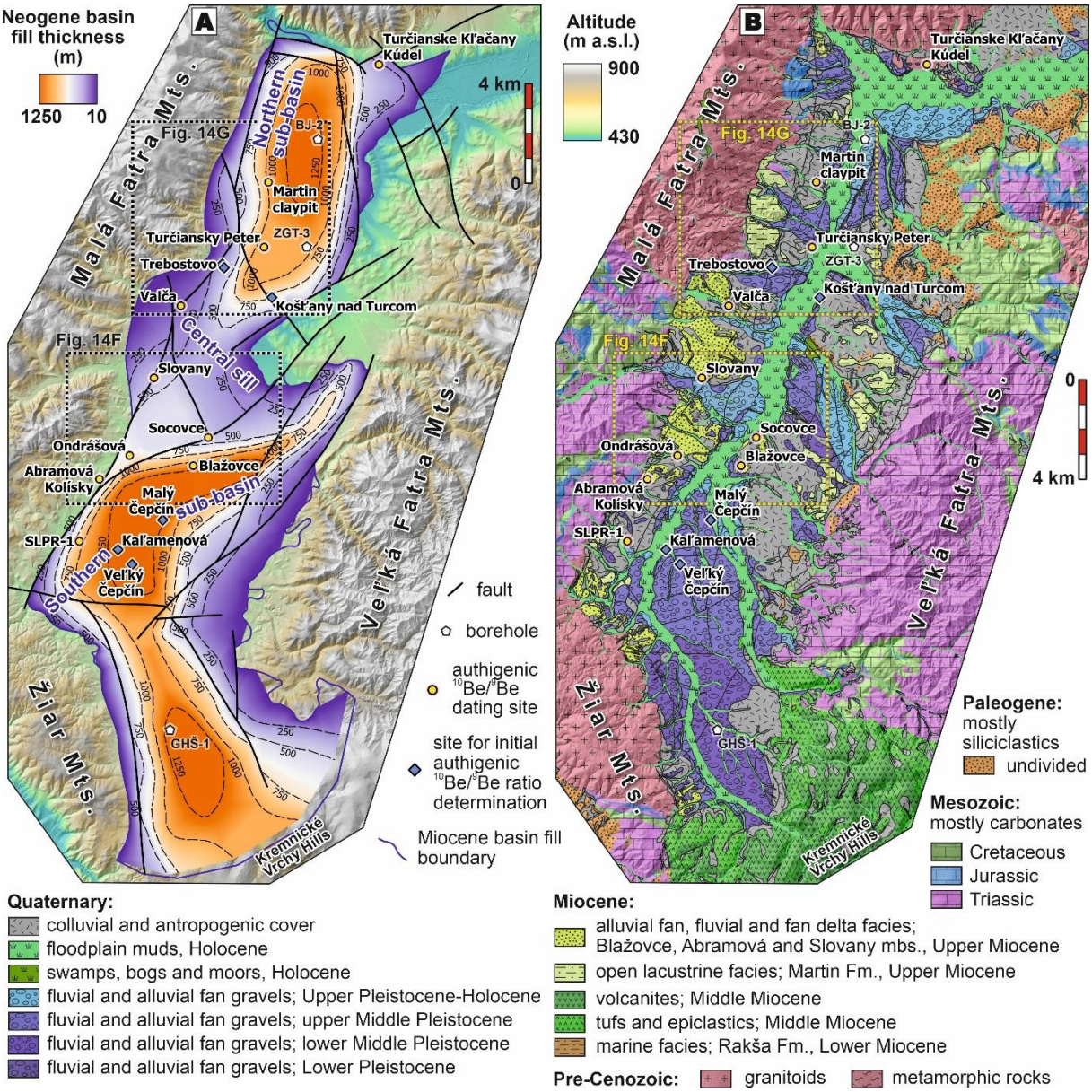

Fig. 2. Location of the studied sites of the Turiec Basin. A: The thickness of the Neogene basin fill. Isobaths and generalized fault network according to Zbořil et al. (1985) are based on wells, vertical resistivity sounding and gravimetric data. It shows general geometry of the basin, however, specific blocky pattern of the halfgraben may differ in detail. B: Geology of the Turiec Basin and surrounding mountains according to the Geological map of Slovakia (2013). The Lidar DEM data were provided by the Geodesy, Cartography and Cadaster Authority of the Slovak Republic.

A position within an orogenic belt commonly leads to the isolation of water bodies formed in intermontane basins from the world's oceans, indeed, frequently even from basins in adjacent regions. The freshwater, brackish and occasionally endemic character of the biota complicates the age determination through biostratigraphy (Harzhauser and Mandic, 2008; Pipík et al., 2012; Magyar, 2021). The frequent presence of hiatuses related to base-level changes may obscure the interpretation of magnetostratigraphic records (Langereis et al., 2010).

This study provides geochronological proxies for the fill of the intermontane Turiec Basin in the Western Carpathians (Fig. 1A, B) intending to constrain the existence and especially the

regression of long-lived Lake Turiec. Despite the lacustrine deposition of long duration, forming a muddy succession up to 900 m thick, the specific history of this basin in the heart of the Western Carpathians was a puzzle due to the scarce geochronological proxies (Kováč et al., 2011). The integration of authigenic $^{10}Be/^{9}Be$ dating, the facies analysis of outcrops, geochemistry and basin analysis shed light on the timing of the existence and regression of the lake, as well as its geodynamic context.

Moreover, this study intends to test the applicability of the authigenic $^{10}Be/^{9}Be$ dating method in the conditions of an intermontane basin. The great potential of the method relies in the possibility to obtain depositional ages for a ubiquitous clay by analysis of the ratio of the cosmogenic radionuclide ^{10}Be produced in the atmosphere, and of stable ^{9}Be derived from weathering of rocks (Bourlès et al., 1989; Lebatard et al., 2008; Willenbring and von Blanckenburg, 2010). However, several effects such as sediment provenance changes, sediment source proximity variation, changes in denudation rate, redeposition of older material or post-depositional alteration may affect the applicability of the method due to the different origin of the isotopes accumulated in the authigenic phase (e.g., Wittmann et al., 2017; Šujan et al., 2023). Hence, a thorough facies analysis was performed, important to constrain such variations in the successions to be dated. A complex approach to the verification of the initial $^{10}Be/^{9}Be$ ratio included in this study aims at resolving the relevance of the mentioned processes in the interest of future utilization of the method in comparable settings.

2. Geological setting

2.1 Structure and stratigraphy of the intermontane Turiec Basin

The Turiec Basin is located within the Central Western Carpathians (CWC) in Central Europe (Fig. 1A, B). The Western Carpathian mountain range comprises the northernmost segment of the European Alpides (Schmid et al., 2008). The internal part of the Western Carpathians, including the CWC, experienced thick- and thin-skinned thrusting in Late Jurassic and Cretaceous times, while the external zones of the continuously propagating orogen underwent thrusting during Paleogene and Neogene and finally collided with the European margin in the Late Miocene. (Hók et al., 2014; Plašienka, 2018). The Paleogene evolution of the CWC was determined by the Paleocene-Middle Eocene exhumation and the Late Eocene to Oligocene existence of the fore-arc type Central Carpathian Paleogene Basin (CCPB) (Králiková et al., 2014a; Kováč et al., 2016). Another phase of exhumation and partial denudation of the Paleogene successions followed in the earliest part of the Early Miocene (Aquitanian) (Králiková et al., 2014a; Kováč et al., 2017b). The first transgression of the Central Paratethys Sea towards the CWC appeared in Early-Middle Miocene times (Kováč et al., 2017a; Kováč et al., 2017b), while its specific timing is a matter of ongoing debate and may well prove to be diachronous (Kováč et al., 2018). The Miocene areal volcanism in the CWC was associated with the formation of the Central Slovakia–Northern Hungary Volcanic Field (SHVF; Konečný et al., 2002; Pécskay et al., 2006). The crustal stretching due to the upwelling asthenospheric mantle and the activity of the Central Slovak Fault System (CSF) during the Middle-Late Miocene has been considered a cause of the formation of the basin-and-range structure of the CWC (Nemčok and Lexa, 1990; Kováč and Hók, 1993). This process led to the formation of intermontane basins, one of which is the Turiec Basin (Kováč et al., 2011; Pulišová and Hók, 2015; Wysocka et al., 2018). The mantle upwelling and subduction pull also caused the rifting of the Pannonian Basin System, which took place simultaneously during ~16–9.5 Ma (Horváth et al., 2006; Šujan et al., 2021b).

The Turiec Basin comprises a half-graben, oriented north-south, ca. 40 km long and 10 km wide, and dipping westwards, where it is bounded by the horsts of the Žiar and Malá Fatra Mts. (Fig. 2). The Veľká Fatra Mts. form the eastern margin and the Middle Miocene volcanic Kremnické Vrchy Hills (a part of the SHVF) limit the southern portion of the basin. These horsts, as well as the basement of the basin, are composed of the paleo-Alpine nappe stack, including a Variscan crystalline basement and Mesozoic, mostly carbonatic sedimentary cover of the Tatric Unit, overlain by the Fatric Unit, comprising Triassic to Lower Cretaceous sequences, and by the Hronic nappe system of predominantly Triassic sequences (Plašienka et al., 1997; Plašienka, 2003; Froitzheim et al., 2008; Havrila, 2011) (Fig. 2B). The nappe structure is sealed by flysch-type Paleogene sediments, which represent erosive remnants of the CCPB cropping out on the eastern and southern margins of the basin.

The late Cenozoic fill of the Turiec Basin reaches an overall thickness of up to 1250 m (Zbořil et al., 1985; Kilényi and Šefara, 1991) (Fig. 2A). It is present in two main depocenters, one to the north (boreholes BJ-2 and ZGT-3) and one to the south (borehole GHŠ-1) (Gašparik, 1972; Fendek et al., 1990; Bielik et al., 2013) (Fig. 2A). The lithostratigraphy of the Miocene basin, according to Kováč et al. (2011) and taking into consideration the refinements made in this paper, is depicted on Fig. 3. The volcano-sedimentary andesite complex of the Turček Formation appears in the southern portion of the basin and consists of andesite lava flows, tuffs, tuffite layers, and clays with a tuff admixture. It has been considered to belong to the Serravallian (Late Badenian) stage (Konečný et al., 1983; Konečný et al., 1995; Chernyshev et al., 2013; Králiková et al., 2014a). The Turček Formation is overlain by the Budiš Member, which has a suggested latest Middle Miocene to early Late Miocene age. It comprises sediments of alluvial fans, with deposition dominated by subaerial gravity flows, and is present only in the southern portion of the basin (Kováč et al., 2011).

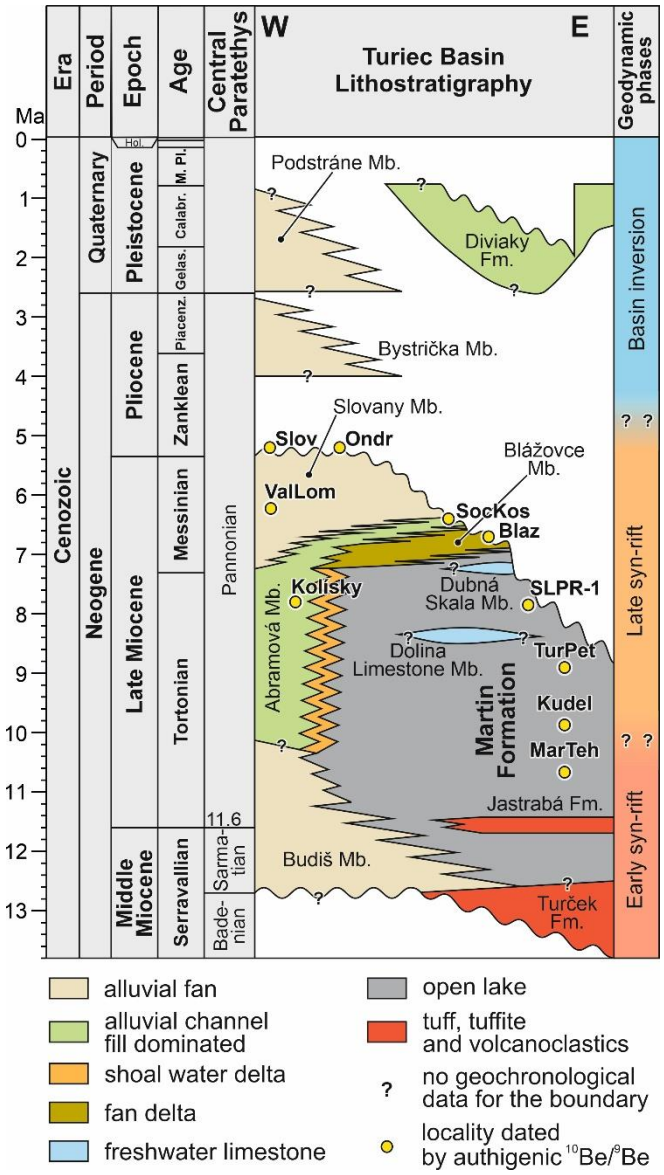

Fig. 3. Lithostratigraphic scheme of the Turiec Basin according to Kováč et al. (2011) and the refinements presented in this study. The stratigraphic position of the studied sites is shown. The timing of geodynamic phases is approximate.

The Budiš Member intercalates with the open lacustrine Martin Formation (Fig. 3). The deposition in the long-lived Lake Turiec likely started in the Serravallian (Sarmatian) and appeared mostly during the Tortonian to Messinian (Pannonian) (Pipík, 2002; Kováč et al., 2011; Pipík et al., 2012) (Fig. 3). The Martin Formation comprises a major part of the syn-rift basin fill reaching a thickness of up to 900 m, and consists predominantly of open lacustrine muds with intercalations of sands deposited by storm or gravity currents. The bathymetric differences of the paleolake are implied by the frequent occurrence of coal seams, water plants and plant detritus, by endemic mollusk and ostracod fauna (Pipík et al., 2012; Neubauer et al., 2015), as well as by the presence of freshwater limestone beds (Fendek et al., 1990; Kováč et al., 2011). The lowermost part of the Martin Formation intercalates with tuffs and tuffites of the Jastrabá Formation, which has been dated by K/Ar and Rb/Sr methods to 12.2–11.4 Ma – around the Middle to Late Miocene boundary (Lexa et al., 1998; Chernyshev et al., 2013). The Turček and Jastrabá fms., together with the Budiš Mb., are considered as deposited during the basin's early rifting stage (Kováč et al., 2011). The Jastrabá Fm. appears stratigraphically below all sites dated in this study and provides their lowermost age constraint. Márton et al. (2022)

achieved magnetostratigraphic dating of the Martin Fm. to 7.7–8.1 Ma in a 100 m long core in the borehole SLPR-1 (Fig. 2, 3). The biostratigraphic age estimates for the Martin Fm. to the Late Miocene (apart from its basal part) are based on endemic mollusk and ostracod fauna and hence are tentative (Kováč et al., 2011; Pipík et al., 2012; Neubauer et al., 2015).

The Martin Formation intercalates with the Abramová Member towards the subaerially exposed southwestern margin of the basin (Fig. 3). It includes gravels of subaerial gravity currents and traction currents in shallow channels, sandy beds, as well as muddy overbank deposits. The clast material is derived solely from the Triassic carbonates of the Hronic Unit. The Abramová Member's depositional environment coexisted for an unknown period with the lacustrine environment of Lake Turiec. The Martin Formation also intercalates with the freshwater limestones of the Dolina Limestone and Dubná Skala members (Kováč et al., 2011).

Following this period of relative stability in depositional environments, fan deltas and alluvial fans prograded from the basin margin to the basin center, marking a significant increase in the sediment supply to accommodation rate ratio (Fig. 3). The alluvial fan and fan delta deposits were previously included in a single lithostratigraphic unit of the Blažovce Member (Kováč et al., 2011); however, the stratigraphy observed in this study implies that the riverine environment of the Abramová Member formed a feeder system, transporting material from alluvial fans of the Slovany Member to fan deltas of the Blažovce Member. The alluvial fan deposits include mostly gravels, intercalations of sands and fine sandy muds of subaerial gravity flow origin (e.g, Ondrašová, Slovany, Valča sites). Fan deltas exhibit a much more complicated stratigraphy, with a wide range of depositional processes, including subaerial and subaquatic gravity flows, channelized traction currents and low-density turbidity currents (Blažovce site). The clast material is again dominated by the carbonates of the Hronic Unit (Kováč et al., 2011).

The Late Miocene sedimentary fill described here generally represents a complete cycle of a tectonic sequence *sensu* Matenco and Haq (2020). While the regressive facies of the sequence are frequently exposed in the central and southern parts of the basin, the subsequent inversion and incision is likely responsible for their denudation and absence in the northern sub-basin (Fig. 2B). The Late Miocene tectonic sequence is overlain discordantly by the alluvial fans of the Bystrička Member of a supposed Late Pliocene age, and by the supposed Early Pleistocene Podstráne Member and the Diviaky Formation. The mentioned lithostratigraphic units differ from the fill of the older basin in having clasts with a more varied petrographic composition, including younger Mesozoic lithotypes and rocks derived from the crystalline basement (Buday, 1962; Minár and Bizubová, 1994; Kováč et al., 2011).

The central zones of the mountains surrounding the Turiec Basin include a planation surface, which appears at altitudes from ca. 700 m a.s.l. (Žiar Mts.) to ca. 1500 m a.s.l. (Malá and Veľká Fatra Mts.) (Lukniš, 1962). This surface, originally called the "Mid-Mountain level", was until recently considered a tectoplain – a polygenetic planation surface created in extensional settings within an orogen (Mazúr, 1963; Minár, 2003). One might expect it to have been formed concurrently with the fine-grained sedimentation of the Tortonian (Pannonian) Martin Formation (Kováč et al., 2011; Minár et al., 2011). The basin fill is deformed by a network of faults with normal to transtensional kinematics, and the faults were active during and/or after the Late Miocene depositional cycle associated with the existence of Lake Turiec (Zbořil et al., 1985; Kováč et al., 2011) (Fig. 2A).

2.2 Paleoenvironmental insight of Lake Turiec from the biota

The isolation of long-lived Lake Turiec led to the development of rich endemic ostracod fauna, which has been extensively studied in past decades, as summarized in Pipík et al. (2012). An overview of the spatial distribution of various fossil associations allows us to specify the

paleoenvironmental conditions of the paleolake. The variation in the initial authigenic $^{10}Be/^{9}Be$ ratio could be attributed to the diversity of paleoenvironments described below.The earliest existence of a lacustrine environment of the Martin Fm. in the Turiec Basin can be estimated to the Serravallian (Sarmatian) (Fig. 3), as may be inferred from the rare ostracod valves of freshwater *Darwinula stevensoni*, *Candona*, *Cypria* and the brackish *Mediocypris* and *Leptocythere* (Kováč et al., 2011). After what was probably a short-lived connection between Lake Turiec with Lake Pannon in the early Late Miocene disappeared, the basin changed from reduced salinity to a freshwater neutral to alkaline lake (Pipík et al., 2012; Ognjanova-Rumenova and Pipík, 2015). Abundant and diverse endemic fauna and flora from the Upper Miocene beds (Márton et al., 2022), such as pollens, macroflora, ostracods, gastropods, bivalves, fish otoliths, and sponges of the family *Spongillidae*, document a topographically, bathymetrically and biologically well-structured terrestrial and aquatic ecosystem and testify to the long-term isolation of the former Lake Turiec. This long isolation led to the evolution of endemic ostracod species, which display a gradual evolution from simple and smooth elongated to complex and ornamented valves; it also permits the relative stratigraphic correlation and reconstruction of paleoecological evolution of the freshwater Turiec Basin fill (Pipík et al., 2012).

The ostracod fauna revealed that shallow environments classified as littoral and not exceeding 40 m depth prevailed in the northern sub-basin of Lake Turiec, reaching only up to 10 m depth at the Martin – claypit site (Fig. 2). The central and southern parts of the basin were dominated by a relatively deep-water zone with depth exceeding 40 m, if the present-day level of thermocline in European lakes is assumed (Pipík et al., 2012). The facies observed in the southern sub-basin indicate a depth less than 100 m.

The shallow lacustrine and littoral deposits of the Martin Formation, which form the main volume of the basin fill, display a broad diversity of ecological conditions and biotope richness (Pipík, 2002; Pipík, 2004; Pipík, 2005). The shallow lacustrine environments in the northern depocenter included marshes with slowly flowing water (ostracod *Ilyocypris*) covered by water plants (*Nelumbium*, *Potamogeton*, and *Myrica*) and coastal humid forest (gastropods *Carychium*, *Succinea*, *Goniodiscus*, and *Vertigo*), oxbows (ostracod *Vestalenula*), and ephemeral, seasonal water bodies in inland. The humid forest growing around a swampy stagnant bay was a feature of the eastern margin. The southwestern margin formed a shallow, littoral zone with the input of gravel from the southwest. The coast was covered by wetland passing into forest, with thermophilic trees and highland vegetation further inland (Kováč et al., 2011; Pipík et al., 2012).

The sublittoral grey calcareous muds of the Martin Formation in the southern sub-basin (Fig. 2), which contain various amounts of sand, silt, and organic matter intercalations concentrated in thin layers, were deposited in a stable, cold environment below the thermocline (~40 m), without significant ecological variation and annual fluctuations in temperature. This biotope was characterized by an endemic, species-rich ostracod association dominated by benthic *Candoninae* (Pipík and Bodergat, 2007). The degree of diversity in the benthic ostracods suggests oxidizing conditions at the water-sediment interface.

The $^{87}Sr/^{86}Sr$ isotopic ratios of faunal shells (bivalves and ostracods), investigated by Pipík (2001) and Pipík et al. (2012) are depicted with their sampling locations in Fig. 18 of the accompanied Data in Brief paper (Šujan et al., submitted). The Martin – claypit site (three samples) in the northern sub-basin yielded higher values reaching 0.708206–0.70832. Three samples from an outcrop at the central sill separating both depocenters provided the Sr isotopic ratio interval of 0.7081699–0.708181. 10 samples from the southern sub-basin, gained from a HGB-3 borehole parallel to the SLPR-1 core and from two outcrops, yielded a wide range of 0.708079–0.708341. The observed Sr isotope variability in the Turiec Basin likely results from

temporal switching of the main sediment input between lithologically diverse exposed rocks, including metamorphosed Paleozoic basement, Upper Devonian to Lower Carboniferous granites, Mesozoic carbonates, and Paleogene flysch-like deposits (Pipík et al., 2012). No spatial trends could be stated, since it is unlikely that the existing measurements represent one time interval across the basin.

3. Methods

Detailed description of the material and methods is available in the accompanied Data in Brief paper (Šujan et al., submitted). Raw datasets are included in the data repository (Šujan et al., 2022).

3.1 Facies analysis and stratigraphy

The standard facies analysis of clastic sediments includes a description of grain size, structure, texture, the geometry and size of the strata, and a visualization of information gained in logs and schemes (Stow, 2005; Miall, 2006). This facies analysis was applied to nine outcrops, located in Fig. 2. The granulometry and rounding of clasts of gravelly facies were analysed by sieving eight samples from the Blažovce, Ondrašová, Valča, and Slovany outcrops, while the granulometry of muddy facies was investigated in eight samples from the Blažovce site using laser diffraction with a Malvern Mastersizer 3000 facility.

The correlation of the facies associations determined on outcrops was performed using the lithological profiles of 45 boreholes. The orientation of the geological sections was selected taking into consideration the best possible representation of the geological structure in the area of studied outcrops in terms of the availability of borehole data. These data were obtained from documents located in the Geofond archive of the State Geological Survey of Dionýz Štúr, and are listed in Table 1 of Šujan et al. (submitted). The lithology was unified using a code of 15 lithological classes, including a distinction between subaerial and subaquatic muddy lithotypes (Fig. 2 in Šujan et al., submitted). The precision of the lithological log descriptions generally permitted us to distinguish units up to a thickness of 0.5 m, while thinner strata are identified only occasionally. The criteria used to distinguish the facies associations defined in the outcrops and used for correlation in borehole geological sections are included in Table 2 of Šujan et al. (submitted). The fault network disrupting the basin fill indicated by Zbořil et al. (1985) was considered during correlation (Fig. 2A). While the generalized geological sections are presented here, the detailed lithological profiles of the borehole logs are included in Figs. 3–5 of Šujan et al. (submitted). The reader is asked to note that inconsistencies might appear between the isopach map on the Fig. 2A (based on interpolation of well and geophysical data in Zbořil et al., 1985) and the geological sections due to generalization and different type of data used. The geological sections include a dip of the tilted blocks towards NWW estimated to 1.5° according to Kováč et al. (2011).

3.2 Authigenic $^{10}Be/^{9}Be$ dating

3.2.1 Principles of the method

The cosmogenic nuclide ^{10}Be is produced in the atmosphere by the interaction of cosmic rays with nuclides of oxygen and nitrogen. The stable isotope of beryllium, ^{9}Be, is derived from parent rock by the decomposition of primary minerals by chemical weathering (Measures and Edmond, 1983; Brown et al., 1992). Meteoric ^{10}Be is transferred to the Earth's surface in soluble form by precipitation (Raisbeck et al., 1981), and ^{9}Be is dissolved in a water column of the hydrosphere (Measures and Edmond, 1983; Brown et al., 1992). Authigenic rims form

around sediment particles during their transport in a water column, predominantly composed of oxyhydroxides of iron and manganese (Bourlès et al., 1989; Willenbring and von Blanckenburg, 2010; Wittmann et al., 2012; Singleton et al., 2017). This authigenic phase is the main carrier of ^{9}Be and ^{10}Be isotopes, and is the place where the authigenic $^{10}Be/^{9}Be$ ratio forms. The continuous growth of authigenic rims has been suggested for sedimentary particles during their transport through large, continental slope systems (Wittmann et al., 2017). Hence, the authigenic phase records changes in the $^{10}Be/^{9}Be$ ratio of a water column of shifting depositional environments, through which a particle is carried. In general, the inner authigenic rim precipitated in riverine and deltaic environments preserves the $^{10}Be/^{9}Be$ characteristics of continental erosion (higher input of ^{9}Be), whereas the outer rim incorporates a ratio with an open-ocean composition (lower input of ^{9}Be). The effect of different water masses mixing in the water column on the $^{10}Be/^{9}Be$ ratio was recently observed in the Pear River Estuary (Kong et al., 2021).

The development of the leaching procedure by Bourlès et al. (1989) to extract the authigenic phase of beryllium isotopes from sediments has already been in use for several decades. The method, initially developed for dating marine sediment, is applicable to continental environments, as well, and with promising results (Barg et al., 1997; Lebatard et al., 2008; 2010; Novello et al., 2015; Simon et al., 2020; Šujan et al., 2016; 2020). The principle for age calculation is based on the radioactive decay of ^{10}Be, and this is given by the equation $N = N_0 \times e^{-\lambda t}$, where N is the authigenic $^{10}Be/^{9}Be$ ratio measured in the sample to be dated, N_0 is the initial authigenic $^{10}Be/^{9}Be$ ratio during deposition, λ is the radioactive decay constant of ^{10}Be and t is the time elapsed since deposition. Determination of the initial ratio is thus essential to obtain reliable depositional ages, but the difference in the sources of both isotopes adds complexity to this requirement. Initial authigenic ratios vary significantly in recent continental sediments, between 3.5×10^{-8} and 1.55×10^{-10} (Brown et al., 1992; Graham et al., 2001; Wittmann et al., 2012), and in the case of oceanic sediments, values range between 0.5×10^{-8} and 30×10^{-8} (Yokoyama et al., 1978; Krishnaswami et al., 1982; Ku et al., 1982; Measures and Edmond, 1982; Sharma and Somayajulu, 1982; Inoue et al., 1983; Kusakabe et al., 1987; Sharma et al., 1987; Bourlès et al., 1989; Henken-Mellies et al., 1990; Ku et al., 1990; Kusakabe et al., 1991; Brown et al., 1992; Measures et al., 1996; von Blanckenburg et al., 1996; Carcaillet et al., 2004; Lachner et al., 2013; von Blanckenburg and Bouchez, 2014). It is thus necessary to determine a regional authigenic N_0 linked to a given deposited sediment. Then the radioactive decay of ^{10}Be can be used to calculate the age of the deposits – if two conditions are met: (1) the initial authigenic ratio N_0 is determined accurately, and (2) the samples selected must have remained closed to the entry or loss of both isotopes, that is, the only factor contributing to the change in $^{10}Be/^{9}Be$ ratio since deposition was the radioactive decay of ^{10}Be. Two approaches which aim at determining a robust initial ratio are (1) by measuring recent sediment samples which are deposited in a similar environment and drainage basin as the sediment to be dated, or (2) by the analysis of independently dated samples representing a similar depositional environment and drainage basin as the samples to be dated. Changes in other aspects such as sediment provenance, climate and denudation rate should certainly be considered.

3.2.2 Strategy for the initial $^{10}Be/^{9}Be$ ratio determination

It has been suggested that, considering the half-life of ^{10}Be, a depositional record with an age of < 200 ka is suitable for the determination of the initial ratio (e.g, Lebatard et al., 2008). The Turiec Basin accumulated various facies during this period. Five sites were selected for determination of the initial authigenic $^{10}Be/^{9}Be$ ratio from alluvial muddy strata, representing

diverse rock provenance demonstrated by petrography of the genetically related gravelly beds (Fig. 2B):

(1) the late Middle Pleistocene (late Riss) alluvial fan Veľký Čepčín, comprising similar ratio of carbonate and andesite gravel clasts in the lower portion, with increasing dominance of carbonate pebbles upwards (7 Samples);

(2) the Late Pleistocene river terrace Malý Čepčín, consisting mostly of andesites (2 samples);

(3) the Holocene well-drained floodplain of the Turiec river at Košťany nad Turcom, having petrographic composition of gravel with prevalence of carbonates and up to a one third of granitoids (3 samples);

(4) the Holocene poorly-drained floodplain of the Turiec river at Kaľamenová, bearing pebbles of andesites and granitoids in similar proportion (3 samples);

(5) the Holocene well-drained floodplain of a small tributary at Trebostovo comprising exclusively granitoids (4 samples).

The age of the sites and petrological composition had been established by previous research, employing exposure cosmogenic nuclide dating and geological mapping (Tužinský et al., 1967; Gašparík and Halouzka, 1993; Kováč et al., 2011; Holec and Braucher, 2014; Sládek et al., 2022). The sites represent different sediment supply to accommodation rate ratios, with the alluvial fan having the highest sediment supply and rapid burial forming a topographic elevation, while the Holocene floodplain accumulated in a topographically low-lying location with a reduced sediment supply. The aim was to determine the natural authigenic $^{10}Be/^{9}Be$ variability in the basin in different paleoenvironmental conditions and provenance of the sites analysed.

Moreover, eight samples of muddy open lake facies were taken from the borehole core SLPR-1, independently dated by magnetostratigraphy to 7.7–8.1 Ma (Márton et al., 2022) (Fig. 2). This age range was used to back-calculate the initial ratio, relevant for open lake deposits of Lake Turiec, since comparable facies are not present in Late Pleistocene-Holocene successions of the basin. The initial ratios were calculated for the lower and upper age constraint (7.7 and 8.1 Ma) for every sample using the radioactive decay equation and the measured natural $^{10}Be/^{9}Be$. The paleo-initial ratio for individual sample was than calculated as the mean value with uncertainty representing the calculated range (N_0 for 7.7 and 8.1 Ma) plus the analytical uncertainty. The single paleo-initial ratio for the SLPR-1 core was finally obtained as a weighted mean of the individual sample values.

3.2.3 Sampling strategy for dating

In total, 31 samples were collected from nine outcrops (Fig. 2A). The outcrops were selected to represent different facies associations (section 4.1) including alluvial fans (the Ondrášová, Valča and Slovany sites), braided rivers (the Socovce and Abramová sites), a fan delta (Blažovce site), and open lakes (the Martin - claypit, Turčiansky Peter and Kúdel sites), to determine the temporal relationship of the depositional systems. Two to seven samples (3 on average) were collected from each site from different layers within an outcrop to discriminate outliers and to find out the degree of paleoenvironmental variability of the beryllium isotopic ratio. In order to trace this variability, rather than collecting multiple samples from a single layer, sampling several layers in a superposition was preferred.

3.2.4 Sample processing

Sample preparation was performed at the Department of Geology and Paleontology laboratory, Faculty of Natural Sciences, Comenius University in Bratislava, based on Bourlès et al. (1989)

and Carcaillet et al. (2004) and tested by Šujan et al. (2018) for the facility at the faculty. The samples were dried in an oven at a temperature of 60°C and crushed, then the extraction procedure was applied to ~2.25 g of a sample using 0.04 M NH_2OH–HCl in a 25°% acetic acid leaching solution (Bourlès et al., 1989). An aliquot of ~2 ml was taken from the leached solution for measurement of ^{9}Be concentration in an ICP-MS, and this was performed at the Institute of Chemistry, at the Slovak Academy of Sciences. To minimize the error in the measurement of the ^{9}Be concentration by the matrix effect, the linear regression method was used (Tan and Horlick, 1987). The same aliquot solution also underwent measurements of selected element concentrations. An amount of ~450 μg of beryllium carrier solution was added to the remaining leached solution (Scharlau, 1000 ppm; $^{10}Be/^{9}Be$ ratio of 7–8 × 10^{-15} (Merchel et al., 2021)). Spiked samples were evaporated, and beryllium was separated from other elements in the sample using column chromatography (Merchel and Herpers, 1999). The precipitate that now remained, containing only beryllium, was washed with pH 8 water and left overnight for ageing (Merchel et al., 2019). The final precipitate was dissolved in a few drops of HNO_3, dried and heated to 800 °C for 1 h. The resulting BeO was mixed with niobium powder and pressed into cathodes for accelerator mass spectrometer (AMS) measurements. $^{10}Be/^{9}Be$ isotopic ratios were measured at the French national AMS facility ASTER, CEREGE (Aix-en-Provence, France). The measurements were calibrated directly against the STD11 in-house standard ($^{10}Be/^{9}Be$ value of (1.191 ± 0.013) ×10^{-11}) (Braucher et al., 2015). Analytical uncertainties (reported as 1σ) include uncertainties associated with AMS counting statistics, chemical blank measurements and the AMS internal error (0.5%).
Each $^{10}Be/^{9}Be$ sample ratio was corrected using its corresponding chemical blank (one chemical blank was processed every seven analyzed samples). The $^{10}Be/^{9}Be$ blank ratios ranged from 6.61 × 10^{-15} to 9.62 × 10^{-15}.

3.3 Geochemistry and mineralogy

3.3.1 Whole rock geochemistry

Whole rock XRF analyses (major oxides) were made from eight samples selected as representative of dating sites (except Slovany), and from four samples selected as representative of Quaternary sites (except Trebostovo), which were used for calibration of the authigenic $^{9}Be/^{10}Be$ initial ratio. Hence, each sample represents one studied site.

XRF measurements were carried out at the laboratory of the Slovak National Museum in Bratislava, Slovakia, using an ARL Quant'X (Thermo Scientific Inc., USA) EDXRF spectrometer. Excitations rays are produced by an air-cooled X-ray tube and the X-rays emitted are detected by means of a Peltier cooled Si (Li) detector, and a pulse processor. The XRF data were calibrated and matrix-corrected using Uniquant software (Ver 5.46), on the basis of a set of fundamental parameters and unique algorithms. Certified reference materials (NSC DC73043, CRM016-50, BCR-176R and BCR-320R) were also integrated with Uniquant data processing. All the measurements were performed in a vacuum.

Additionally, five whole rock samples from the Blažovce quarry were analyzed using ICP-ES (major oxides) and ICP-MS (trace elements) in the Bureau Veritas mineral laboratories (Canada, Vancouver). The samples were pulverized and dissolved using Lithium Borate Fusion. The content of TOC, C and S was analyzed using the LECO Carbon-Sulfur analyzer. Enrichment factors were calculated as $X_{EF} = (X_{sample}/ Al_{sample})/(X_{UCC}/Al_{UCC})$, where the normalization values UCC follow McLennan (2001). The CIA index (Nesbitt and Young, 1982) was calculated using a simplification developed by McLennan (1993).

3.3.2 Mineralogy of whole rock and clay fraction

Twelve silty mud samples collected from the outcrops were analyzed using the X-ray diffraction (XRD) method at the Croatian Geological Survey, Zagreb. XRD patterns were recorded on random mounts of whole rock samples and oriented mounts of the <2 μm fraction using a PANalytical vertical goniometer (type X`Pert) equipped with a Cu-tube and under the following experimental conditions: 45 kV, 40 mA, PW 3018/00 PIXcel detector, primary beam divergence 1/4° and continuous scan (step 0.02 °2θ/s). Preparation for the XRD analyses included: sample grinding for whole rock analyses, sieving the samples through the 63 μm sieve to remove part of carbonate content and then separation of the <2 μm fraction from the sample by centrifugation (Krumm, 1994) for oriented mounts (glass slides). Oriented samples of the <2 μm fraction were recorded after the treatments described in Šujan et al. (submitted). The identification of clay minerals was performed according to Starkey et al. (1984) and Moore and Reynolds (1997). The X-ray interpretation was performed using High Score Plus (PANalytical, 2016) calculation and the database of the International Centre for Diffraction Data (2022).

3.3.3 Authigenic phase ICP-MS of Fe, Mn and Al

The aliquots taken for the analysis of beryllium concentration in all dating samples were subject to the measurement of their iron and manganese concentration using ICP-MS, since these elements are expected to form the major portion of the oxy-hydroxides leached from the authigenic phase (Wittmann et al., 2012). The analyses were performed specifically to observe variations in elemental concentrations in correlation with beryllium and the $^{10}Be/^{9}Be$ ratio as a potential indicator of post-depositional growth of the authigenic rims, since this is a possible effect modifying the authigenic $^{10}Be/^{9}Be$ record due to various duration of a soil profile exposure (Tsai et al., 2008; Graly et al., 2010; Willenbring and von Blanckenburg, 2010; Bacon et al., 2012; Dixon et al., 2018).

4. Results

4.1 Facies associations on outcrops

Facies analysis allowed us to distinguish 27 distinct lithofacies, which are listed in Table 1, together with a description and interpretation of the depositional processes in play in each case. The stacking patterns of the observed lithofacies implied their grouping into four facies associations (Table 2), and these are described and interpreted below.

Table 1: List of lithofacies documented on the outcrops in the Turiec Basin, their properties and interpreted depositional processes.

Code	Lithology, structure, texture and geometry	Depositional processes
Gm, GSm	massive matrix-supported gravel to gravelly coarse- to medium-grained sand, granules, pebbles and boulders, poorly sorted, angular to subangular, forming tens of centimeters to meters thick, possibly amalgamated bodies	subaerial debris flow (Nemec and Steel, 1984; Pierson and Costa, 1987; Brenna et al., 2020)
Gmg	massive normally graded clast- to matrix-supported gravel, sandy matrix, granules to pebbles, fewer boulders, forming tens of centimeters to meters thick horizontal tabular bodies	hyperconcentrated flow (Pierson and Costa, 1987; Brenna et al., 2020)

Gmgr	massive reverse graded clast- to matrix-supported gravel, sandy matrix, granules to pebbles, fewer boulders, angular to subangular, forming tens of centimeters to meters thick horizontal tabular bodies	subaerial debris flow (Nemec and Steel, 1984; Pierson and Costa, 1987; Brenna et al., 2020)
Gk	massive clast-supported gravel, moderately to well sorted, subangular to rounded, granules and pebbles, forming ~0.5–1.0 m thick amalgamated tabular and lenticular bodies, frequently amalgamated, infrequent muddy-sandy intraclasts	debris flood (Church and Jakob, 2020; Brenna et al., 2020)
Gkg	massive normally graded clast-supported gravel, moderate to well sorted, angular to subangular, matrix almost absent, granules to pebbles, fewer boulders, forming tens of centimeters thick horizontal tabular bodies	hyperconcentrated flow (Church and Jakob, 2020; Brenna et al., 2020)
GFp	clast-supported gravel, poorly imbricated, pebbles, fewer granules, moderate to well sorted in a single bed, subangular to rounded, inclined layers of sandy mud a few centimeters thick forming foreset-like intercalations	shallow traction current, accretion of a bar in poorly topographically defined shallow channel, periodical variation of transport capacity (Šujan et al., 2021a)
Gt	clast-supported gravel arranged into inclined beds a few centimeters thick, tangential contacts with base, granules to pebbles, moderately to well sorted in a single bed, subangular to rounded, arranged into lenticular bodies a few meters thick with a concave erosional base	channelized traction current, accretion of a bar (Boothroyd and Ashley, 1975; Nemec and Postma, 1993; Gobo et al., 2016; Martini et al., 2017)
Gh	clast-supported gravel arranged into subhorizontal beds a few centimeters thick, granules to pebbles, subangular to rounded, forming tens of centimeters thick horizontal tabular bodies	sheet flow (Blikra and Nemec, 1998; North and Davidson, 2012)
Gh-for	clast-supported gravel arranged into planar beds a few centimeters thick, granules to pebbles, forming tens of centimeters thick 10–20° inclined tabular bodies within 5–7 m thick clinoforms	stratified subcritical high-density turbidity current on a fan delta foreset (Postma and Cartigny, 2014)
Gk-for	massive clast-supported gravel, granules to pebbles, less boulders, forming tens of centimeters thick 10–20° inclined tabular bodies within 5–7 m thick clinoforms	grainflow on a fan delta foreset (Lowe, 1976; Nemec and Steel, 1984; Mulder and Alexander, 2001)
Gmg-for	massive normally graded clast- to matrix-supported gravel, granules to pebbles, fewer boulders, forming tens of centimeters thick 10–20° inclined tabular bodies within 5–7 m thick clinoforms	hyperconcentrated flow on a fan delta foreset (Mulder and Alexander, 2001; Tallling et al., 2012)
Gmh	massive clast-supported gravel, granules to pebbles, fewer boulders, forming tens of centimeters thick stacked tabular bodies, shape frequently curved and deformed	stratified subcritical high-density turbidity current on a fan delta bottomset (Postma and Cartigny, 2014) deformed by loading of a prograding delta front (Longhitano, 2008)
Gmm	massive matrix-supported gravel, granules to pebbles, fewer boulders, forming ca. 10 cm thick isolated tabular bodies	hyperconcentrated flow (Mulder and Alexander, 2001) or non-cohesive debris flow (Tallling et al., 2012) on a fan delta bottomset
Sl-for	medium- to coarse-grained sand, in ca. 1 cm thick planar beds with wavy undulations, infrequent granules, strata arranged in tens of centimeters thick 10–20° inclined tabular bodies within 5–7 m thick clinoforms	low-density subcritical turbidity current (Postma and Cartigny, 2014) or hyperpycnal flow (Mulder et al., 2003) on a fan delta foreset

Sw	medium- to coarse-grained sand, forming wavy stratification with concave and convex shapes, in lenses or tabular bodies ca. 5 cm thick, usually in between gravelly bodies	suspension fallout from a supercritical traction current (Fielding, 2006; Cartigny et al., 2014)
Sm	massive medium- to coarse-grained sand, forming tens of centimeters thick tabular bodies or lenses, may contain muddy intraclasts	rapid deposition from a waning flow with high sediment concentration (Mulder and Alexander, 2001; Baas et al., 2016)
Sh	horizontally laminated fine-grained sand, loading-related faulting and deformations appear	low-density subcritical turbidity current (Postma and Cartigny, 2014) or hyperpycnal flow (Mulder et al., 2003) on a fan delta bottomset, deformed by loading of a prograding delta front (Longhitano, 2008)
Sl	medium- to fine-grained sand, in ca. 1 cm thick planar beds, strata arranged in tens of centimeters thick tabular bodies	low-density subcritical turbidity current (Postma and Cartigny, 2014) or hyperpycnal flow (Mulder et al., 2003) on a shallow lake bottom
SFr	unidirectional ripple cross-stratified muddy sand	slow traction current (Allen, 1982; Yawar and Schieber, 2017)
Srw	symmetrical ripple cross-stratified fine- to medium-grained sand	oscillatory traction current (Dumas et al., 2005; Amoudry et al., 2013)
Shc, SFhc	hummocky cross-stratified sand or muddy sand	storm wave oscillatory traction current (Dumas and Arnott, 2006; Jelby et al., 2020)
St	trough cross-stratified fine-grained sand in lenticular bodies	traction current forming 3D dunes (Allen, 1982; Leclair and Bridge, 2001)
SFd	beds of laminated sand and sandy mud, arranged in folds, deformed penecontemporaneously	deformation of sediment due to slumping or loading of a prograding delta front (Longhitano, 2008; Owen et al., 2011)
SFh, FSh	horizontally laminated very fine-grained muddy sand to sandy mud, deformations and loading-related faulting appear	low-density subcritical turbidity current (Postma and Cartigny, 2014) or hyperpycnal flow (Mulder et al., 2003) on a shallow lake bottom
Fl, FSl	laminated light brown to reddish mud or sandy mud	deposition from a slow traction current or suspension in a proximal floodplain or on an alluvial fan (Aslan and Autin, 1999; Yawar and Schieber; 2017)
Fm, FSm	massive light grey, light brown to reddish mud to muddy sand	deposition from a suspension of a high mud-concentrated waning flow in an oxbow lake, on a proximal floodplain or an alluvial fan (Toonen et al., 2011; Baas et al., 2016)
Fh	horizontally laminated grey to blue mud, occasional mollusc shells	slow traction current on a lake bottom (Allen, 1982; Yawar and Schieber, 2017)
Fmb, SFmb	massive dark grey to blue mud, presence of mollusc and trace fossils	primary processes questionable, structures reworked by bioturbation (Scott et al., 2012), deposition likely by suspension settling in a calm

		water column (Potter et al., 1980, 2005),

4.1.1 FA1: Alluvial fan deposits

Description:

The first facies association was documented on the Valča, Ondrašová, and Slovany outcrops (Fig. 4). Relatively extensive outcrops reaching stratigraphic thickness 8–19.5 m allow a quantitative evaluation of the lithofacies (Table 4 in Šujan et al., submitted). The lithofacies assemblage is dominated by gravelly or sandy-gravelly tabular bodies, forming 80.3°% (Valča), 89.7°% (Ondrašová) and 80.8°% (Slovany) of the stratigraphic sections. The remaining part of the outcrops comprise tabular or lenticular bodies of sandy muds or muds reaching thicknesses of generally < 30 cm.

The Valča site consists of the most variable lithofacies (Fig. 4 A1, A2). Massive matrix-supported gravels or gravelly sands with a low level of sorting (Gm, GSm, Sm) alternate with normally or reverse graded gravels (Gmg, Gmgr) and with clast-supported gravel with poorly developed imbrication and foreset-like sandy mud intercalations (GFp). While Gm, GSm, and Sm lithofacies attain only a relatively low average thickness (AT = 0.27 m) and high abundance (16), Gmg, Gmgr, and GFp lithofacies occur much less frequently and with a relatively high average thickness of AT = 0.95–1.41 m. The gravelly units mentioned above are separated by frequent massive sandy muds or muds (FSm. Fm) with AT = 0.18 m and by less frequent laminated sandy muds (FSl) with AT = 0.15 m.

The Ondrašová section is less complex, consisting mostly of massive matrix-supported gravels and gravelly sands (GSm, Gm) with AT = 0.98 m, divided by massive sandy muds or muds (FSm, Fm) reaching AT = 0.09 m or by laminated muds (Fl) attaining AT = 0.18 m (Fig. 4B).

The Slovany outcrop is predominantly comprised of massive matrix-supported gravel (Gm; AT = 0.63 m) and reverse graded gravel (Gmgr; AT = 1.75 m) (Fig. 4C). The gravelly units are separated by massive sandy muds and muds (FSm, Fm; AT = 0.34 m) and by laminated sandy muds (FSl; AT = 0.19 m). The muddy horizons below the reverse graded gravels exhibit penecontemporaneous deformations resembling flame structures (Fig. 4C).

A relatively poorly sorted (3.1–3.3 phi) fraction with a content of 5–10 % muddy to fine-grained sandy is documented in the lithofacies Gm by cumulative granulometric curves seen in Fig. 6 of Šujan et al. (submitted). The GSm lithofacies contains a significantly higher proportion of fine-grained sand and mud. A bimodal character is implied by the cumulative granulometric curve of the GFp lithofacies, with higher content of medium-grained sand. Following Folk and Ward (1957), the sorting of all samples reaches values of 3.11–3.44 and may therefore be classified as very poorly sorted (Table 5 in Šujan et al., submitted). Gravels from all three sites exhibit a sub-angular to sub-rounded nature, with a less frequent presence of rounded clasts in the grain size classes between 16 mm and 64 mm (Figs. 7–10 in Šujan et al., submitted). The petrography of the gravel clasts is monotonous on the basis of macroscopic evaluation, with the presence of light and dark limestones, and somewhat less frequent dolomites. Clasts from the Valča site are yellow to reddish in color by secondary precipitation (Fig. 8 in Šujan et al., submitted).

Interpretation:

The most common lithofacies, those with massive matrix-supported gravel to gravelly sand and characterized by poor sorting (Gm, GSm) may be interpreted as subaerial debris flow (Nemec

and Steel, 1984; Pierson and Costa, 1987; Brenna et al., 2020). The reverse graded massive clast- to matrix-supported gravel (Gmgr) was also likely formed by the process of subaerial debris flow (Pierson and Costa, 1987; Brenna et al., 2020). On the other hand, the appearance of the massive normally graded clast- to matrix-supported gravel (Gmg) implies its origin as hyperconcentrated flow (Pierson and Costa, 1987; Brenna et al., 2020). A debris flow represents the gravitational movement of a highly-concentrated shearing mixture of debris and water (Van Dine, 1985; Blikra and Nemec, 1998), whereas a hyperconcentrated flow is characterized by a high concentration of sediment transported in suspension and by rapid and intense deposition from suspension fallout (Pierson and Costa, 1987; Pierson, 2005; Church and Jakob, 2020). The GFp lithofacies, composed of clast-supported, poorly imbricated gravel with the presence of foreset-like inclined muddy intercalations may be interpreted as a deposit of a traction current in a shallow channel (Šujan et al., 2021a), as distinct from the gravity flows mentioned above. The overall volumetric dominance of subaerial surge-type flows in the depositional record of FA1 indicates its origin as formed by alluvial fans, with a lower proportion of deposition in shallow channels (Blikra and Nemec, 1998; Plink-Björklund, 2021; Šujan, 2021) (Table 2). Some of the massive matrix-supported gravel units (Gm, GSm) reach considerable thicknesses – up to 3.15 m and are likely composed of several amalgamated depositional events. Massive sandy mud and mud layers (FSm, Fm) represent abrupt suspension fallout deposition from a surge-type flow with a high concentration of fine-grained sediment (Baas et al., 2016), which is likely associated with slopewash processes on the surface of an alluvial fan (Nemec and Kazanci, 1999). The very small proportion of laminated sandy mud or laminated mud layers (FSl, Fl), reaching 3.8–7.0 %, implies minor deposition from slow traction currents or even from suspension in a standing water column (Aslan and Autin, 1999; Yawar and Schieber, 2017).

Table 2: Facies associations defined based on lithofacies stacking patterns observed on the outcrops in the Turiec Basin.

Facies association	Sedimentary environment	Facies	Processes
FA1	Alluvial fan	Gm, GSm, Gmg, Gmgr, GFp, Sm, FSm, Fm, FSl	unconfined subaerial gravity flows, less frequent channelized episodic floods and traction currents
FA2	Braided river	Gk, Gm, SGm, Gkg, Gh, Sm, Fl	episodic floods and traction currents in shallow channels, overbank well-drained floodplain deposition, less frequent unconfined subaerial gravity flows
FA3	FA3a: Fan delta topset	Gh, Gt, Gmg, Gm, Sw, FSl	channelized traction current or shallow unconfined traction current, less frequently unconfined subaerial gravity flows
	FA3b: Fan delta foreset	Gh-for, Gmg-for, Gk-for, Sl-for	high sediment-concentrated gravity currents on a fan delta slope, mass-wasting and slope processes
	FA3c: Fan delta bottomset	FSh, SFh, Fh, FSd, Fm, Sl, Sw, Gmh, Gmm	high sediment-concentrated gravity currents on the toe of a fan delta slope, low sediment-concentrated turbidity currents in transition to open lake environment, deformations due to loading of the prograding delta
FA4	Open lake	Shc, FShc, FSh, SFh, Fmb, SFmb, FSr, Sm, St	deposition below normal weather wave base, oscillatory storm wave currents alternate with deposition from suspension, slow bottom currents or distal hyperpycnal flows

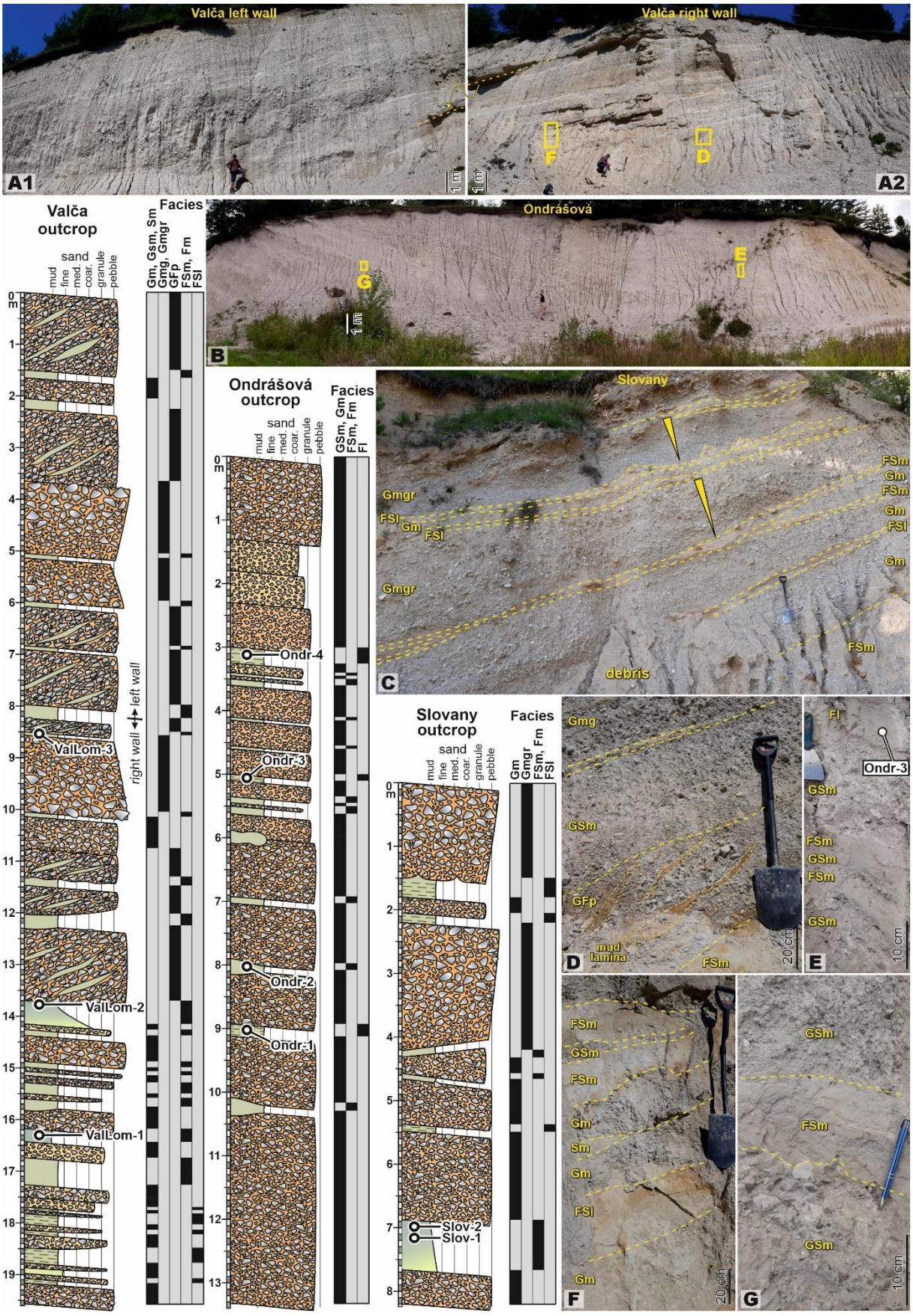

Fig. 4. Alluvial fan facies association documented on the sites Valča, Ondrašová and Slovany, with photo-documentation of stratal geometry (A–C) and lithofacies (D–G). Lithofacies codes are explained in Table 1. Location in Fig. 2.

4.1.2 FA2: Braided river deposits

Description:

Facies association 2 was documented on the Abramová – Kolísky and Socovce sites. The scale and character of the outcrops allow only for a qualitative facies analysis. The Abramová – Kolísky site may be regarded as the type locality of the Abramová Member (Kováč et al., 2011). A major part of the Abramová – Kolísky site consists of massive clast-supported gravel with moderate to well sorting, 20–30 cm thick (Gk), forming amalgamated bodies. The boundaries of individual, likely lenticular bodies can be observed locally by tracing a change in the prevailing grain size (Fig. 5). The Gk facies include deformed sandy-muddy intraclasts in its uppermost portion (Fig. 5D). A significant proportion of the stratigraphic section is formed by massive normally graded clast-supported gravel (Gkg), locally divided by planar beds of clast-supported gravel few centimeters thick (Gh) (Fig. 5D, E). The boundaries of tabular bodies are undulating. On the other hand, laminated light brown to reddish mud (Fl) comprises around one-third of the observed stratigraphic column (Fig. 5C). The transition upwards from gravelly to muddy facies is associated with the presence of 10–20 cm thick massive medium- to coarse-grained sand units (Sm) with an undulating erosional base and lenticular shape (Fig. 5C).

The Socovce site comprises a cliff of significantly lithified gravels reaching a thickness of ~13m (Fig. 6A, C). The lithification makes it difficult to clean the outcrop and carry out quantitative observations, nevertheless, lithofacies of massive matrix-supported gravel (Gm) and massive clast-supported gravel with moderate to well sorting (Gk) prevail (Fig. 6C). A muddy section was observed ca. 1 m above the cliff composed dominantly of laminated light brown to reddish mud (Fl) with occasional layers of massive sand a few centimeters thick (Fig. 6B).

Interpretation:

The sorting and texture of the Gk lithofacies implies its origin as a deposit of debris flood (Brenna et al., 2020; Church and Jakob, 2020). Debris flood is characterized by a water-driven flood with high bedload transport inducing full mobility of almost all grain sizes, usually confined in a steep channel, and by the deposition of bedload-carpet accretion (Manville and White, 2003; Church and Jakob, 2020). It may be contrasted with debris flow associated with the unconfined deposition of a gravity-driven non-Newtonian mixture of water and sediment (Van Dine, 1985). Debris floods are typical of mountain streams with high sediment supply and more frequent flash flood events (Brenna et al., 2020). The presence of the Gkg lithofacies records deposition of fewer frequent hyperconcentrated flows (Brenna et al., 2020; Church and Jakob, 2020). Sheet flow appeared sporadically, as evidenced by the gravelly subhorizontal beds of the Gh lithofacies (Blikra and Nemec, 1998; North and Davidson, 2012). In contrast to the previously mentioned gravelly facies, the frequently present lithofacies Fl indicate sedimentation from very slow traction currents ($<0.25\ m \cdot s^{-1}$) or from a suspension in a standing water column. The massive sand of the Sm lithofacies implies a rapid deposition from a highly sediment-saturated flow (Mulder and Alexander, 2001; Baas et al., 2016). The association of depositional processes points to an alternation of channelized traction current and surge-type flows, unconfined subaerial gravity flows and overbank calm deposition of mud, implying a depositional environment of a proximal braided river with a small catchment prone to significant yearly discharge variability (Miall, 2006; Fielding et al., 2018; Paseban et al., 2018) (Table 2).

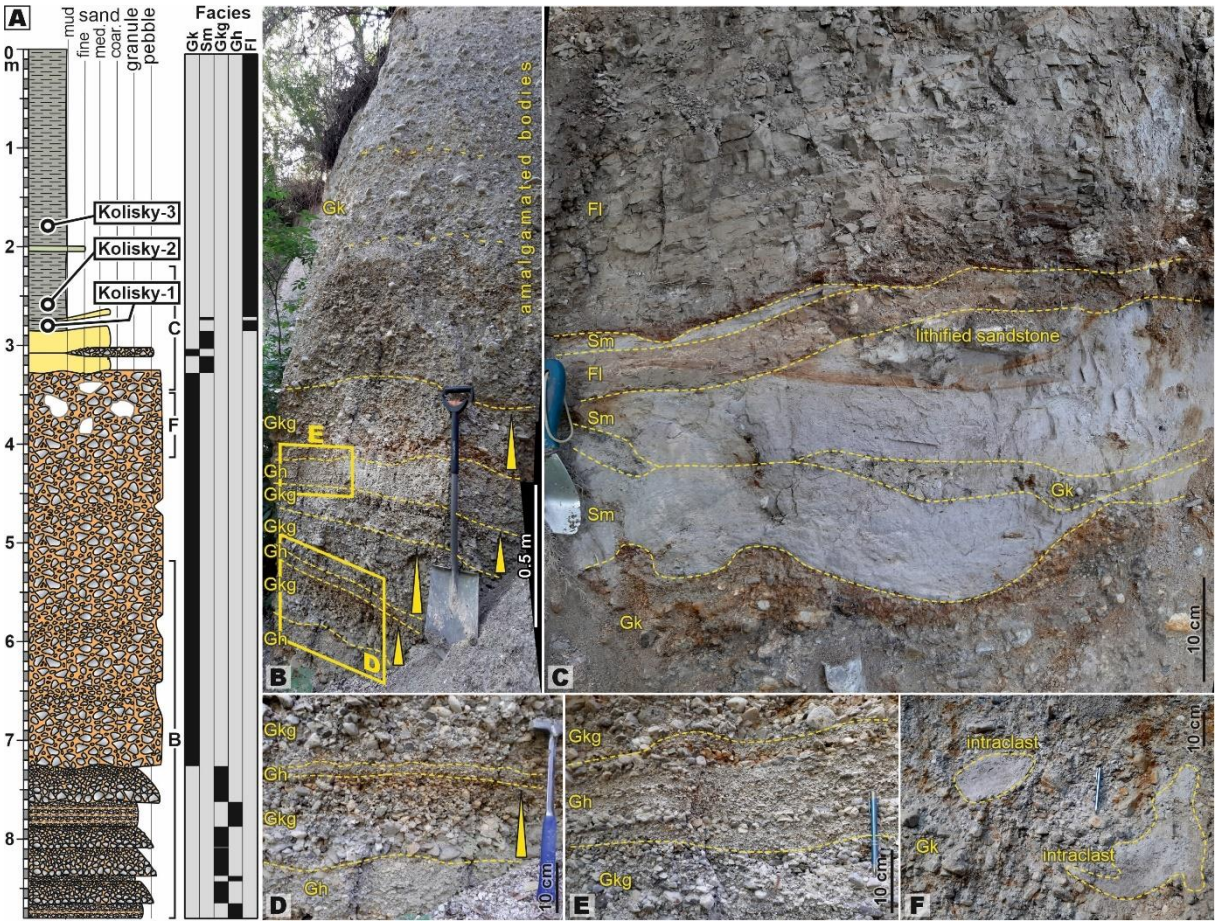

Fig. 5. Braided river facies association documented on the Abramová – Kolísky site (A), with photo-documentation of stratal geometry (B) and lithofacies (C–F). Lithofacies codes are explained in Table 1. Location in Fig. 2.

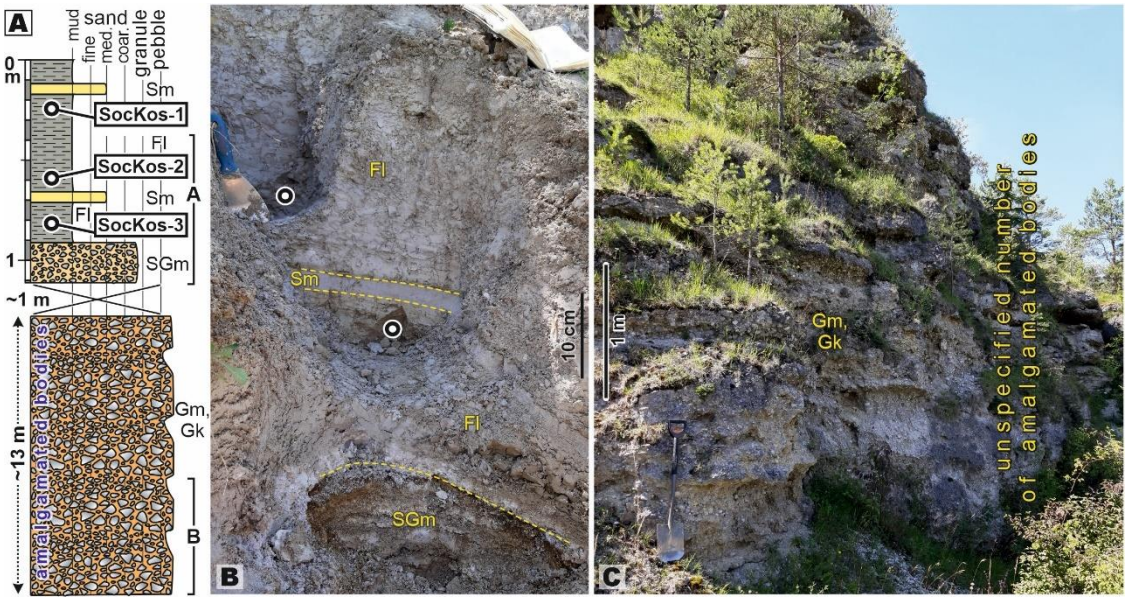

Fig. 6. Braided river facies association documented on the site Socovce (A), with photo-documentation of the dating sampling point (B) and amalgamated lithofacies with indistinct boundaries due to intense lithification (C). Lithofacies codes are explained in Table 1. Location in Fig. 2.

4.1.3 FA3: Fan delta deposits

Description:

The fan delta facies association was documented at a single site within the Blažovce gravel quarry. The outcropping succession reaches a thickness of 27 m and is exposed continuously on three main levels, with only ca. 2.5 m of covered interval (Fig. 12 in Šujan et al., submitted). The outcrops expose an alternation of three distinct facies sub-associations, marked as FA3a (topset), FA3b (foreset) and FA3c (bottomset) (Table 2). The Blažovce quarry is the type locality of the Blažovce Member (Kováč et al., 2011).

The sub-association FA3a (topset) is dominated by clast-supported gravel arranged into subhorizontal beds a few centimeters thick (Gh) (Fig. 7A–D) and by lenticular bodies a few meters thick with concave bases, which are composed of inclined gravelly beds with tangential contacts towards the base (Gt) (Fig. 7E). Lithofacies of massive normally graded clast- to matrix-supported gravel (Gmg) or massive matrix-supported gravel (Gm) are present less frequently, both up to few tens of centimeters thick (Fig. 8B). Intercalations between the gravelly bodies are formed occasionally by wavy laminated sandy layers a few centimeters thick (Sw) (Fig. 8B) or by laminated sandy mud (FSl) (Fig. 7E, F). The overall geometry of the FA3a strata is subhorizontal.

On the other hand, the strata of facies sub-association FA3b (foreset) are inclined at an angle, ranging between 12–25° (Figs. 8A, 9A, B, Fig. 13 in Šujan et al., submitted). The thickness of the foresets may attain 7 m (Fig. 8A), though some were observed of only 0.5–1.5 m in thickness (Fig. 7A, D). The most frequent facies forming the foresets is clast-supported gravel arranged into planar beds a few centimeters thick (Gh-for) (Figs. 7A, D; 8B), which are less frequently substituted by massive clast-supported gravelly beds some tens of centimeters thick, usually more coarse-grained (Gk-for) (Fig. 8C). The lower parts of the thicker (>3 m) foresets frequently comprise massive normally graded clast- to matrix-supported gravels (Gmg-for), especially on the transition towards the bottomsets (Fig. 8D). A relatively rare foreset facies is composed of medium- to coarse-grained sand with floating granules and forms ca. 1 cm thick planar beds, which exhibit wavy undulations (Figs. 8C; 9A). The orientation of the foreset inclination exhibits a relatively high degree of variability from west to south-southeast, with a maximum towards southwest (Fig. 13 in Šujan et al., submitted).

The bottomset facies sub-association FA3c attains sub-horizontal bedding (Fig. 9A, C) or very gentle inclination (Fig. 10). The transition from foreset to bottomset is locally tangential with the direct continuation of the beds from inclined to sub-horizontal geometry (Fig. 9A). The most frequently observed lithofacies is composed of horizontally laminated very fine-grained muddy sand to sandy mud with the frequent presence of small-scale blind faults and deformations, and with internal erosional contacts (FSh, SFh) (Figs. 8D; 9C; 10C). These layers are commonly intercalated with: (1) horizontally laminated grey to blue plastic mud (Fh) some centimeters thick(Fig. 10B), (2) tabular bodies of deformed massive clast-supported gravel (Gmh) or massive matrix-supported gravel some tens of centimeters thick (Gmm) (Fig. 10B, C), (3) beds of sand and mud deformed in folds (SFd) (Fig. 8D), or (4) laminated medium- to coarse-grained sand (Sl) (Fig. 10B). The tangential transition from foreset to bottomset is locally associated with stratified wavy sand (Sw) a few centimeters thick (Fig. 8D). An interval of massive light brown mud with reddish bands several meters thick was observed (Fm) onlapping on the slope of underlying foreset facies (Fig. 7C, D). The boundaries of individual beds are frequently undulate and locally exhibit truncation (Fig. 10B, C).

The average grain size of gravelly facies is -0.9 to -2.9 phi (granule to pebble), and exhibits a similar degree of sorting to the alluvial fan deposits, with values of 3.20–3.27 phi (Folk and

Ward, 1957), an exception being the topset Gt lithofacies, which reaches 2.37 phi (Table 5, Fig. 6 in Šujan et al., submitted). The proportion of the fine sandy to muddy fraction decreases in comparison to the alluvial fan strata. Nevertheless, the rounding of the clasts is similar to the alluvial fan facies, only with a slightly lower proportion of sub-angular specimens in favor of the rounded ones (Fig. 10 in Šujan et al., submitted). A visual evaluation of petrographic composition does not indicate any difference between this and alluvial fan gravel samples (Figs. 7–10 in Šujan et al., submitted). Laser diffraction granulometry of the muddy Fh facies indicates the dominance of fine-grained silt (peak 10–11 μm), with a low proportion or absence of fine sand and a low proportion of the clay fraction (Fig. 11 in Šujan et al., submitted). The percentual proportion of grain sizes of the Fm lithofacies exhibits a very similar pattern, with an increased clay content in the case of two samples. Two samples representing the FSh lithofacies contain different proportions of sand (6.2°% and 20.7°%), and fine- or medium-grained silt comprises the maximum volume (16 μm and 33 μm). All analyzed samples of muddy facies display poor sorting according to Folk and Ward (1957), with values in the range of 1.08–1.61 phi (Table 5 in Šujan et al., submitted).

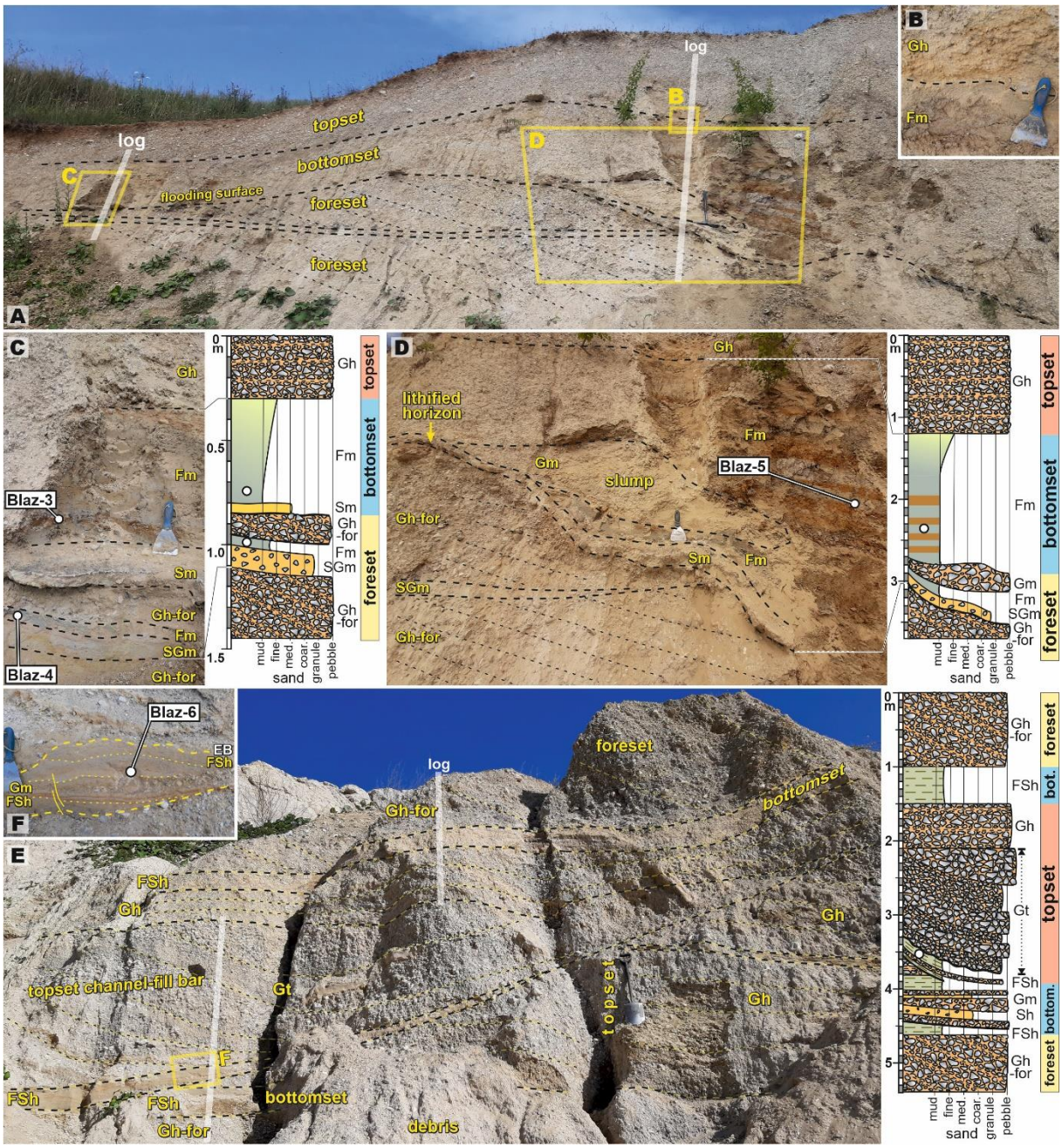

Fig. 7. Outcrops of the Blažovce site showing FA3a facies sub-associations (topset), FA3b (foreset) and FA3c (bottomset) of a fan delta. (A) The inclined gravelly foreset beds are overlain by massive muds of bottomset facies (C, D), and capped by the subhorizontal gravels of the topset (B). (E) The topset facies commonly include large, concave lenses of tangentially stratified gravels a few meters thick and 10–15 m wide, which may include lenses of sandy mud (E). For location within the quarry, see Fig. 12 in Šujan et al. (submitted).

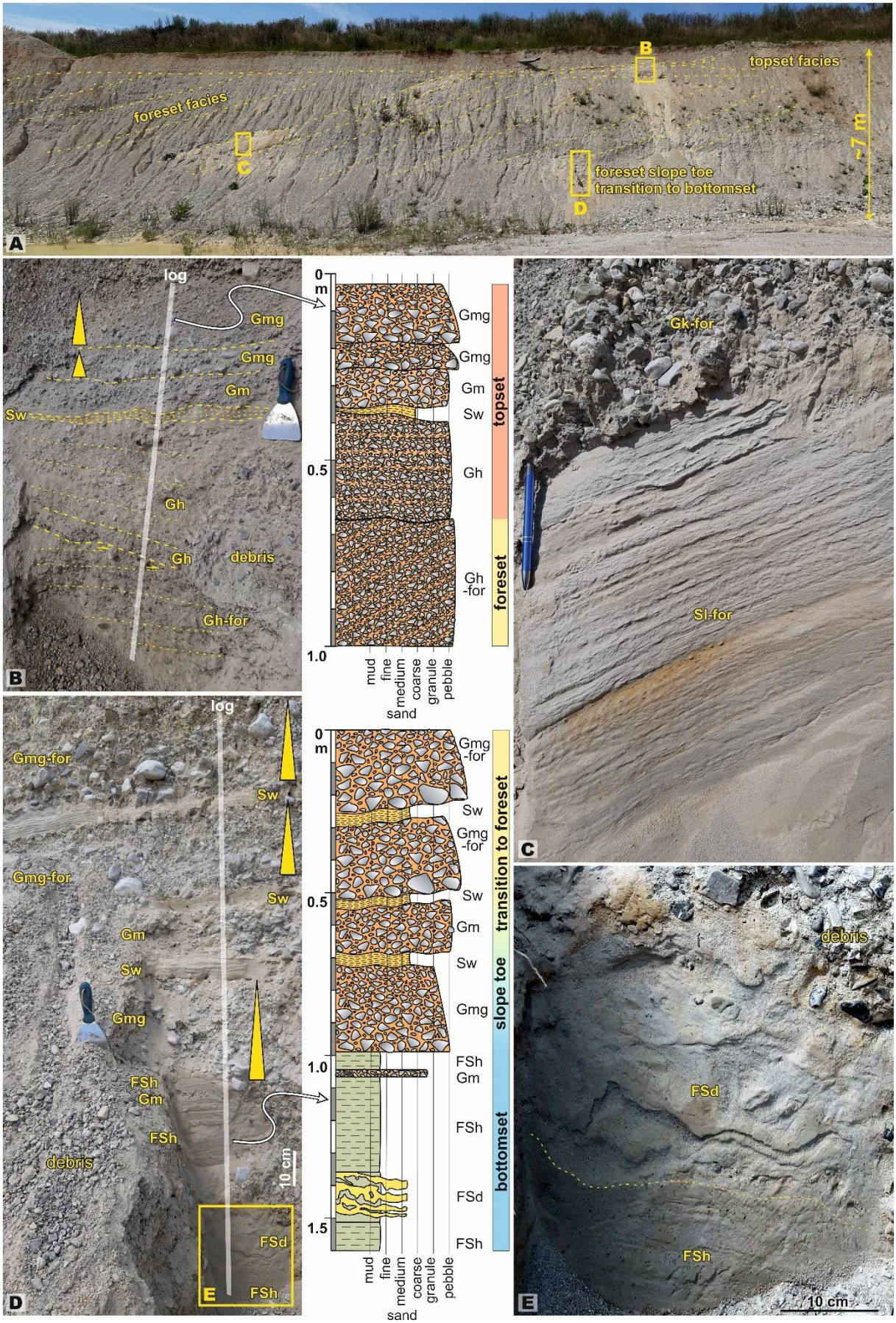
A
B
topset facies
foreset facies
C
~7 m
foreset slope toe
transition to bottomset
D
B
log
Gmg
Gmg
Gm
Sw
Gh
Gh
debris
Gh-for
0
m
0.5
1.0
Gmg
Gmg
Gm
Sw
Gh
Gh
-for
topset
foreset
mud
fine
medium
coarse
granule
pebble
sand
C
Gk-for
Sl-for
D
log
Gmg-for
Sw
Gmg-for
Sw
Gm
Sw
Gmg
FSh
Gm
FSh
debris
10 cm
FSd
E
FSh
0
m
0.5
1.0
1.5
Gmg
-for
Sw
Gmg
-for
Sw
Gm
Sw
Gmg
FSh
Gm
FSh
FSd
FSh
transition to foreset
slope toe
bottomset
mud
fine
medium
coarse
granule
pebble
sand
E
debris
FSd
FSh
10 cm

Fig. 8. Outcrops of the Blažovce site showing mainly the facies sub-association FA3b (foreset) of a fan delta. (A, B) Note the transition from subhorizontal topset facies to the below-lying ca. 7 m thick inclined foresets formed by gravels and sands (C), which decrease the slope angle at the point of contact with bottomset sandy and muddy facies (D), including beds deformed by slumping (E). For location within the quarry, see Fig. 12 in Šujan et al. (submitted).

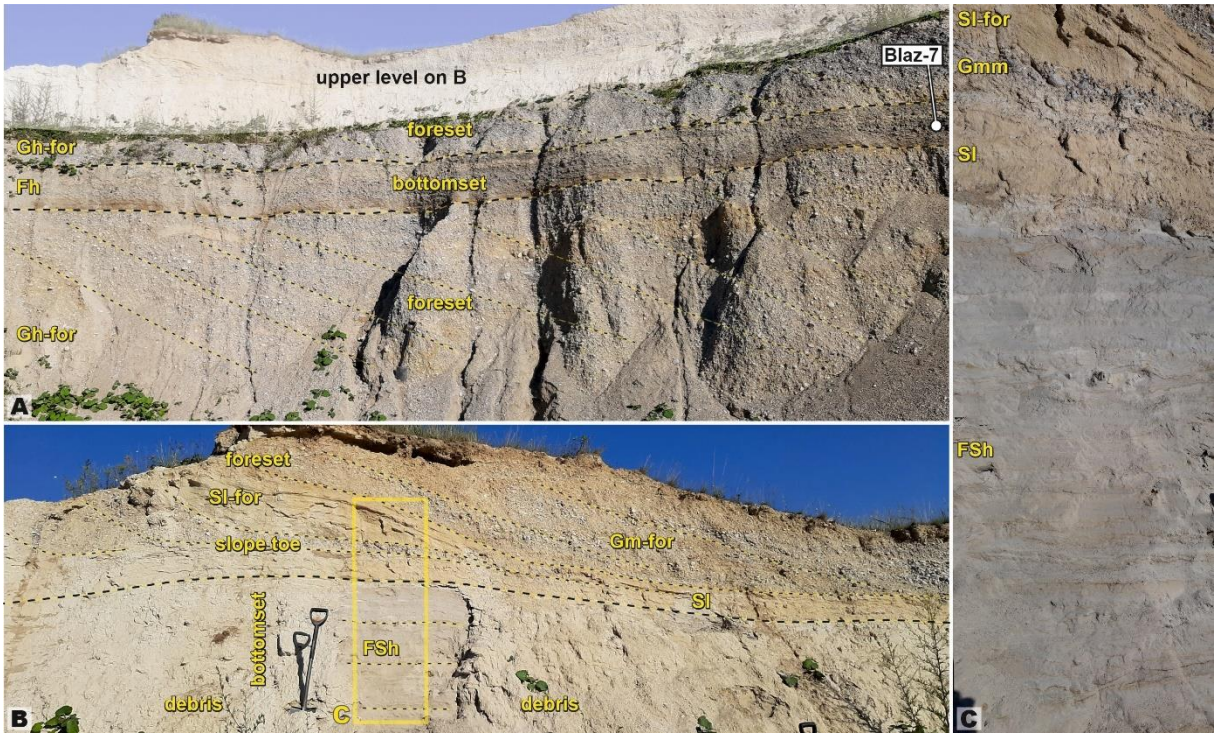

Fig. 9. Outcrops of the Blažovce site showing facies sub-associations FA3b (foreset) and FA3c (bottomset) of a fan delta. (A) Note the sharp angular contact between foreset and bottomset facies. (B) Alternatively, a tangential transition from foreset to bottomset facies was observed. (C) Grain size contrast between bottomset sandy muds and foreset sands and gravels. For location within the quarry, see Fig. 12 in Šujan et al. (submitted).

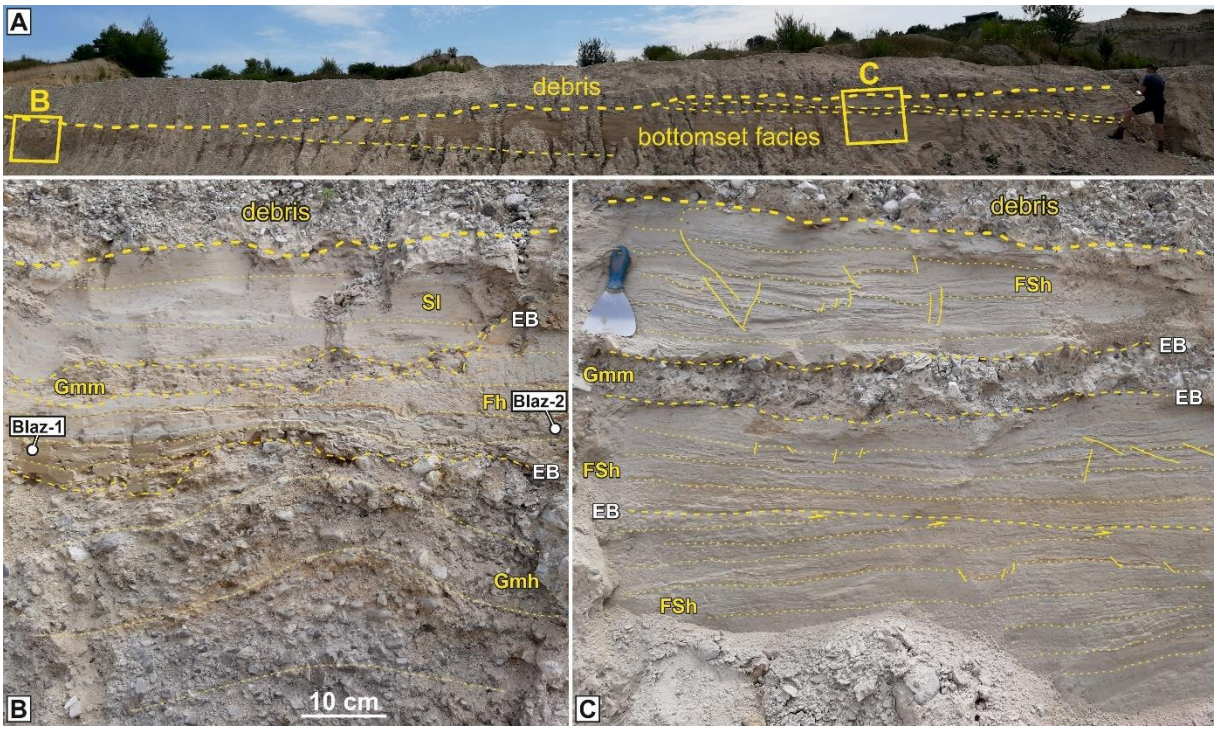

Fig. 10. Outcrops of the Blažovce site showing facies sub-association FA3c (bottomset) of a fan delta. (A) The subhorizontal beds include layers of sands, muddy sands and muds, frequently deformed by compactional small-scale faults associated with loading, which alternate with gravelly layers (B, C). For location within the quarry, see Fig. 12 in Šujan et al. (submitted).

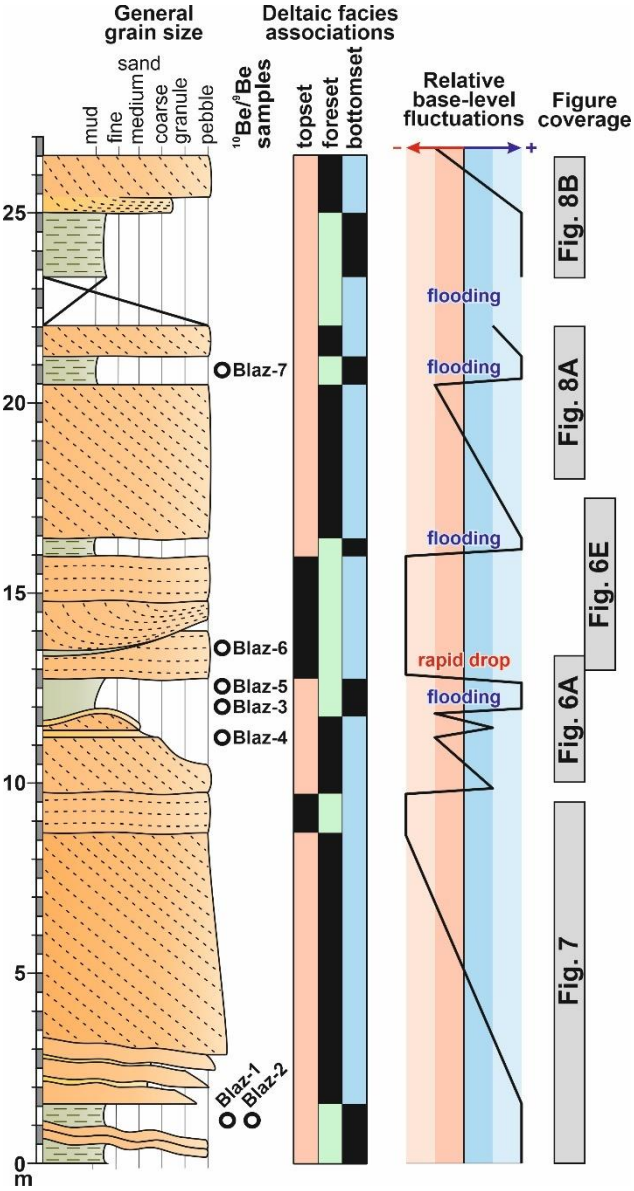

Fig. 11. Synthetic generalized log of the Blažovce stratigraphic section, including interpretation of the water level changes based on the variation between topset, foreset and bottomset facies, as well as on the thickness of individual foresets. Location in Fig. 2.

Interpretation:

The topset facies FA3a are dominated by deposition from (1) a very shallow traction current of sheet flow, forming the horizontal gravelly beds of lithofacies Gh (Blikra and Nemec, 1998; North and Davidson, 2012), and by (2) a bar in a channel a few meters deep, prograding trough deposition from a confined traction current (Boothroyd and Ashley, 1975; Nemec and Postma, 1993; Gobo et al., 2015; Martini et al., 2017) (Table 1). Less frequent deposition appeared from subaerial gravity currents, either as a hyperconcentrated flow forming the Gmg lithofacies (Pierson and Costa, 1987; Brenna et al., 2020), or as a debris flow leading to the accumulation of the Gm lithofacies (Nemec and Steel, 1984; Pierson and Costa, 1987; Brenna et al., 2020). A relatively infrequent deposition appeared as suspension fallout from a supercritical traction current forming the wavy laminated sands of the Sw lithofacies (Fielding, 2006; Cartigny et al., 2014).

The presence of the foreset slope significantly affected the range of depositional processes, which were dominated by gravity currents. The Gh-for lithofacies, composed of inclined gravelly clast-supported beds, represents the result of a stratified high-density turbidity current, while the diagnostic criterion for its subcritical nature is the overall absence of backset (antidune or cyclic step) geometry (Postma and Cartigny, 2014) (Table 1). Increased concentration of clasts in a sediment-water mixture led to the occurrence of hyperconcentrated flows depositing the Gmg-for lithofacies (Mulder and Alexander, 2001; Talling et al., 2012) and grain flows forming the Gk-for lithofacies (Lowe, 1976; Nemec and Steel, 1984; Mulder and Alexander, 2001). Overall, a lower concentration of sediment and prevailing sandy fraction during floods resulted in low-density subcritical turbidity currents (Postma and Cartigny, 2014), or hyperpycnal flows (Mulder et al., 2003), and formed the stratified sands of lithofacies Sl-for.

The transition of the foreset towards the bottomset on the slope-toe comprises a significant reduction of slope angle, which caused a decrease in the inertia of gravity flows. Hence, the high sediment-concentrated gravity flows did not reach far toward the basin floor and formed a significantly lower proportion of the bottomset succession in comparison to the foreset strata. These gravity flows are represented by the stratified subcritical high-density turbidity currents of the Gmh lithofacies (Postma and Cartigny, 2014) as well as the Gmm lithofacies, formed by hyperconcentrated flows (Mulder and Alexander, 2001) or non-cohesive debris flows (Talling et al., 2012) (Table 1). The bottomset succession is dominated by the lithofacies FSh and SFh, associated with low-density subcritical turbidity currents (Postma and Cartigny, 2014) or hyperpycnal flows (Benvenuti, 2003; Mulder et al., 2003), which persisted with much higher inertia after reaching the slope-toe in comparison to the coarse-grained gravity currents and proceeded towards the bottomset (Olariu et al., 2010). The occasional presence of the wavy laminated sands of the Sw lithofacies implies the occurrence of a supercritical low-density turbidity current (Postma and Cartigny, 2014). The massive muds of the Fm lithofacies may reasonably be expected to have been formed by deposition from suspension from a standing water column or a waning flow with a high mud concentration (Baas et al., 2016). Laminated muddy strata (Fh) are considered to be a result of slow traction currents (Allen, 1982; Yawar and Schieber, 2017). The gravity-current origin of the Fh, FSh and Fm muddy lithofacies is also implied by their poor sorting (Table 5 in Šujan et al., submitted).

The association of facies described here implies the depositional environment of a fan delta (e.g., Nemec and Steel, 1984; Benvenuti, 2003; Longhitano, 2008; Budai et al., 2021). The depth of the water column changed through time, as illustrated in the synthetic generalized log in Fig. 11, reaching 0.5–7 m according to the clinoform heights. The changes in water level were likely associated with the filling of the accommodation space by a fan delta progradation and repeated floodings, with a base-level rise in the order of 1–5 m, which appeared at least four times in the observed depositional record. Hence, the foresets reaching only 0.5–1.0 m may represent a mouth bar rather than a fully developed fan delta slope (Benvenuti, 2003). Furthermore, a water-level drop was observed in the 12.75 m of the stratigraphic log, recorded by a change from bottomset facies directly to topset (Fig. 11). The gravelly bottomset strata exhibit frequent undulation, while muddy strata are deformed by small-scale blind faults. Additionally, sandy-muddy horizons deformed by slumping were observed. All these features represent the common result of mass wasting on a fan delta foreset-to-bottomset transition and loading related to fan delta progradation (Postma, 1984; McConnico and Bassett, 2007; Longhitano, 2008). Peak discharges during floods were likely associated with foreset deposition from turbidity currents, while grain flow and debris flow processes were perhaps triggered by a delta brink failure (Gobo et al., 2015). The abandonment of the shallow foreset seen in Fig. 7A, which is overlaid by massive bottomset muds accumulated by suspension fallout from a calm water column, was likely related to the autogenic lateral migration of a delta lobe (Van

Dijk et al., 2009; Paola, 2016; Hajek and Straub, 2017). The clast lithology and rounding of the fan delta facies are very similar to what was observed in the case of alluvial fan facies (Figs. 7–10 in Šujan et al., submitted), implying that these environments once comprised the sediment-feeder components of a single source-to-sink system.

4.1.4 FA4: Open lake deposits

Description:

The outcrops of the Martin Formation available for study are small exposures providing only a point-like qualitative sedimentological insights. The muddy succession of the Martin Formation was defined based on fossil fauna and observations from the Martin claypit, along with the cores of boreholes drilled in the Turiec Basin (Pipík, 2004; Kováč et al., 2011; Pipík et al., 2012; Neubauer et al., 2015). However, the originally >20 m high outcrop of the claypit is now covered by a landfill, and only a 1.2 m thick section in a nearby gully remains exposed and therefore available to study (Figs. 2, 12A, Fig. 14 in Šujan et al., submitted). The facies are dominated by mud, sandy mud, and muddy sand. It is most commonly massive, with preserved bioturbation marks, and articulated mollusc shells appear in it (Fmb, SFmb lithofacies) (Fig. 12B–D). Sandy mud or muddy sand appears also as a horizontally laminated lithofacies, the FSh and SFh. Muddy sand with lamination including concave and convex geometries, forming lenses a few centimeters thick divided by erosional surfaces also of concave and convex shapes was observed; this resembles hummocky-cross stratification (SFhc; Fig. 12C). Another horizon of muddy sand includes unidirectional ripple-cross stratification of the lithofacies SFr (Fig. 12B). The lithological boundaries are either smooth and transitional or sharp and bioturbated (Fig. 12B-D). A vertical change along the section from massive to more stratified and more coarse-grained strata is evident (Fig. 12A).

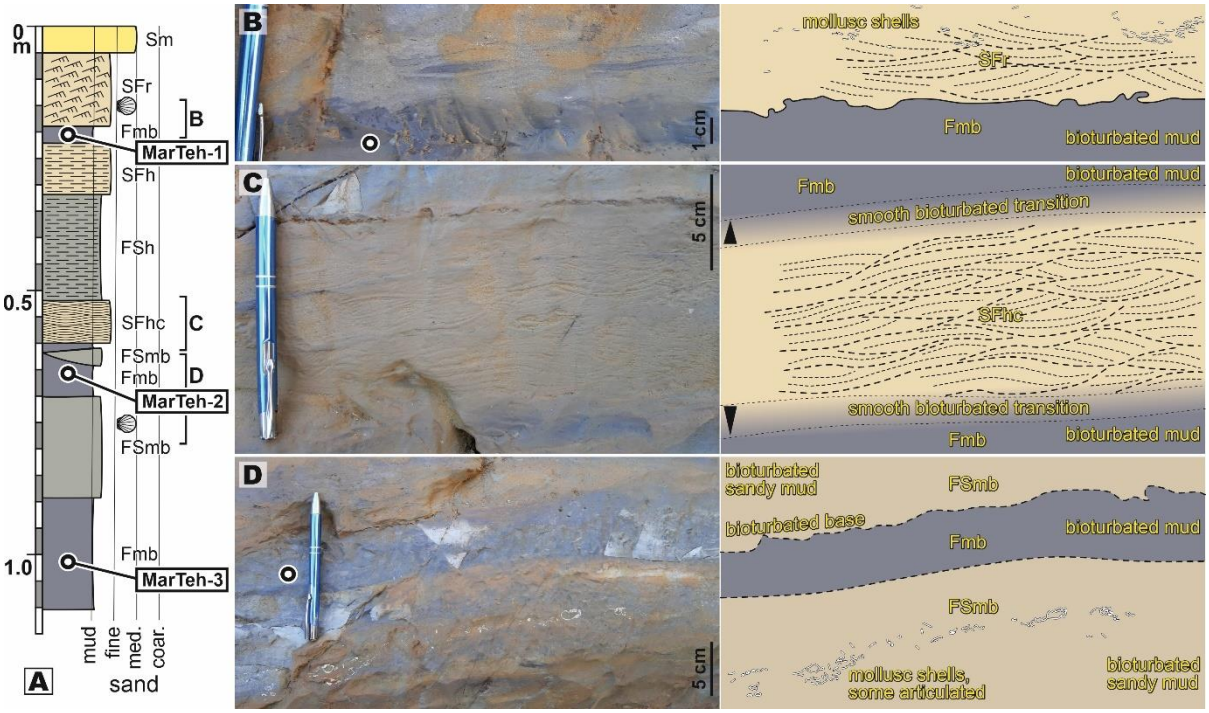

Fig. 12. Outcrop located in a gully nearby the Martin claypit, exposing the open lacustrine facies of the Martin Formation. Correlation to the original section of Pipík (2004) in Fig. 14 of Šujan et al. (submitted). Location in Fig. 2.

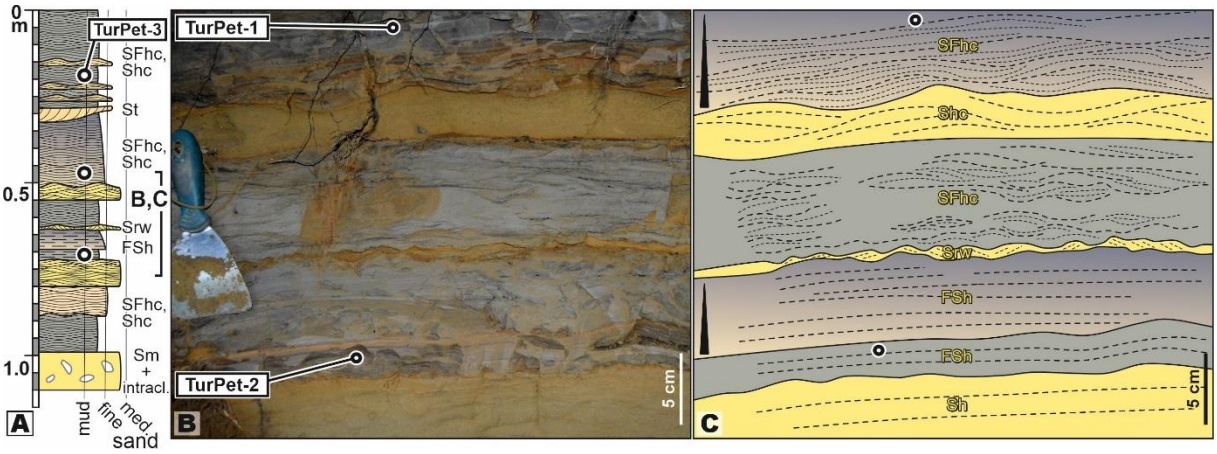

Fig. 13. Outcrop located in a river cut near Turčiansky Peter, exposing the open lacustrine facies of the Martin Formation. Location in Fig. 2.

Another small area of exposure of the Martin Formation was documented in the cut of the riverbank near Turčiansky Peter (Figs. 2, 13A). The lithological boundaries of the muddy sand, sandy mud and sandy strata are sharp and erosional. The dominant lithofacies of sand and muddy sand attain a concave and convex geometry of lamination with internal erosional surfaces typical of hummocky-cross stratification (SFhc, Shc; Fig. 13B, C). The horizontally laminated sandy mud of the lithofacies FSh appears less frequently, together with occasional symmetrical sandy ripples (Srw) and trough cross-stratified sands (St) (Fig. 13). Massive sand with muddy intraclasts of the Sm lithofacies was also observed.

The last exposure of the Martin Formation included in this study is present in a cut of a small creek called Kúdel near Turčianske Kľačany (Fig. 2, Fig. 15 in Šujan et al., submitted). The outcrop exposes massive grey mud, covered by a subrecent accumulation from the creek and by recent soil.

Interpretation:

Massive muds of the Fmb lithofacies do not have preserved primary structures, likely due to extensive bioturbation; their deposition by suspension settling from a calm water column (Potter et al., 1980; Potter et al., 2005), or by slowly flowing traction currents could nevertheless be expected (Yawar and Schieber, 2017). Laminated muds and sandy muds of the Fh and FSh lithofacies are interpreted as deposits of slow traction currents (Yawar and Schieber, 2017), hyperpycnal flows (Mulder et al., 2003), or distal low-density turbidity currents (Postma and Cartigny, 2014; Boulesteix et al., 2019). Hummocky cross-stratification is considered to be a result of deposition from storm wave oscillatory traction currents (Dumas and Arnott, 2006; Jelby et al., 2020). Unidirectional traction currents formed a minor proportion of the successions studied, either as ripples (SFr) or as subaqueous dunes of the St lithofacies (Allen, 1982; Leclair and Bridge, 2001). Calm-weather oscillatory flow forming symmetrical ripples also appeared (Dumas et al., 2005; Amoudry et al., 2013). This association of depositional processes implies an open basin environment affected by temporally variable siliciclastic input from a river delta and by wave reworking of sediment (Table 2). The Martin – claypit succession formed under the influence of a much-reduced regime of wave activity compared to the Turčiansky Peter site.

4.2 Stratigraphy based on borehole correlation

The facies associations (FA) defined on outcrops were correlated using the lithological profiles of boreholes to investigate their distribution and stacking patterns in the basin fill (Fig. 14). The distinguishing criteria included in Table 2 of Šujan et al. (submitted) allowed only the correlation of (1) FA1: Alluvial fan, (2) FA4: Open lake, and (3) FA2 & FA3: Fan delta &

braider river. FA2 and FA3 could not be distinguished definitely due to the level of accuracy of the lithological profiles. Moreover, the blocky pattern of the basin syn- and post-depositional deformation leads to frequent fault contact in FA, which causes unclear correlation locally (Fig. 14A, E). The sections show the areas along the southern sub-basin and along the northern sub-basin separately (Figs. 2, 14F, G).

A clear spatial trend in the FA distribution could be seen in the section along the Slovany and Socovce sites (Fig. 14A), with the transition from alluvial fan deposits occurring in the northwest towards a braided river/fan delta FA. The connection with the open lake strata in the main depocenter and the southeast is not clear and likely disrupted by faults. Section B, across the Abramová site, shows only the first braided river/fan delta deposits, some tens of meters thick, below the present surface (Fig. 14B). A lateral transition from FA1 to FA2 & FA3 and finally to FA4 proceeding west to east is documented in section C along the Ondrašová and Blažovce sites (Fig. 14C), similarly to section A (Fig. 14A). The perpendicular section D solely reveals the transition from FA1 to FA2 & FA3 from north to south (Fig. 14D). This spatial pattern implies sourcing of sediment from the northwest towards the southeast.

The northern area (Fig. 14G) is investigated by the section E along the Valča, Turčiansky Peter, and Martin – claypit outcrops (Fig. 14E). The spatial distribution of lithotypes shows the dominance of alluvial fan deposits in the south, divided likely by a fault from an area of patchy presence of the braided river/fan delta FA interfingering with the open lacustrine strata. Again, the transition is not clear due to the absence of detailed data. Section E indicates a southern position for the clastic sediment source.

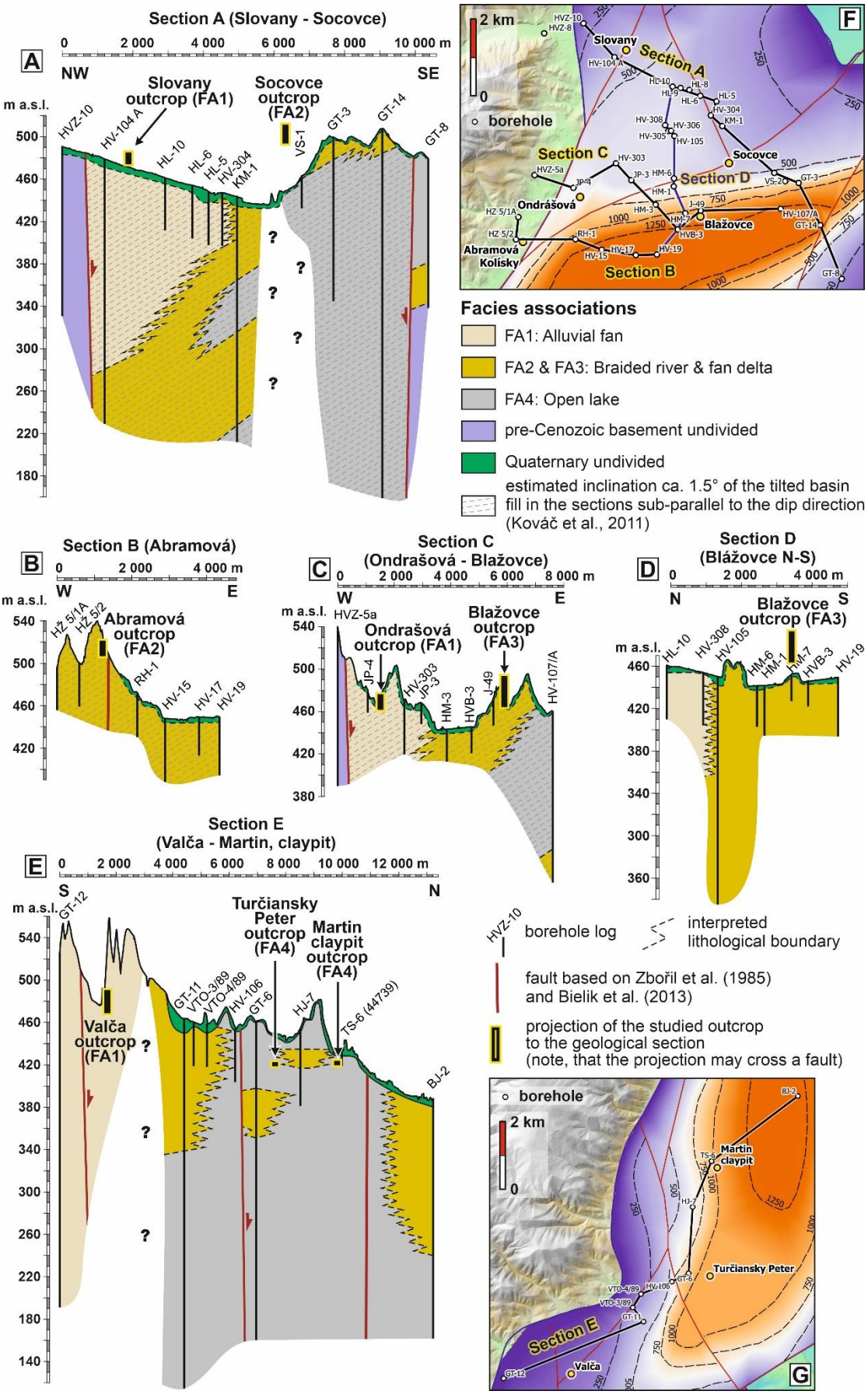
A
Section A (Slovany - Socovce)
NW
SE
m a.s.l.
Slovany outcrop (FA1)
Socovce outcrop (FA2)
HVZ-10
HV-104 A
HL-10
HL-6
HL-5
HV-304
KM-1
VS-1
GT-3
GT-14
GT-8
F
2 km
borehole
Section A
Section C
Section D
Section B
Slovany
Socovce
Ondrášová
Blažovce
Abramová
Kolísky
B
Section B (Abramová)
W
E
HZ 5/1A
HZ 5/2
Abramová outcrop (FA2)
RH-1
HV-15
HV-17
HV-19
C
Section C (Ondrašová - Blažovce)
HVZ-5a
Ondrašová outcrop (FA1)
Blažovce outcrop (FA3)
JP-4
HV-303
JP-3
HM-3
HVB-3
J-49
HV-107/A
D
Section D (Blážovce N-S)
N
S
Blažovce outcrop (FA3)
HL-10
HV-308
HV-105
HM-6
HM-1
HM-7
HVB-3
HV-19
E
Section E (Valča - Martin, claypit)
S
N
GT-12
Turčiansky Peter outcrop (FA4)
Martin claypit outcrop (FA4)
Valča outcrop (FA1)
GT-11
VTO-3/89
VTO-4/89
HV-106
GT-6
HJ-7
TS-6 (44739)
BJ-2
G
Facies associations
FA1: Alluvial fan
FA2 & FA3: Braided river & fan delta
FA4: Open lake
pre-Cenozoic basement undivided
Quaternary undivided
estimated inclination ca. 1.5° of the tilted basin fill in the sections sub-parallel to the dip direction (Kováč et al., 2011)
HVZ-10
borehole log
interpreted lithological boundary
fault based on Zbořil et al. (1985) and Bielik et al. (2013)
projection of the studied outcrop to the geological section (note, that the projection may cross a fault)

Fig. 14. Generalized and schematic geological sections showing the distribution of facies associations across the Turiec Basin, as defined at the outcrops. The locations on the maps and explanations may be seen in Fig. 2. Detailed versions of the sections, including borehole lithological logs, are included in Figs. 4–6 of Šujan et al. (submitted). References for the specific borehole data are included in Table 1 of Šujan et al. (submitted). The fault network is based on Zbořil et al. (1985). The tentative position of the faults relies on geophysical and geomorphological data. Note, that the outcrop position is a projection and that the basin fill comprises several blocks tilted towards the NWW with a dip estimated to 1.5° (Kováč et al., 2011).

Temporal trends recorded in vertical changes in FA distribution are less well-imaged due to the restricted thickness of the stratigraphic column penetrated by the existing boreholes. Nevertheless, a change upwards from FA2 & FA3 to FA1 is shown in borehole HV-104 A (section A), as well as a vertical transition from FA4 to FA2 & FA3 in boreholes KM-1, GT-3 and GT-14 (Fig. 14A). Changes upwards from open lake to braided river/fan delta FA are documented by section E in boreholes GT-11, GT-3, HJ-7 and BJ-2 (Fig. 14E). Generally, the observed pattern of vertical (temporal) changes of FA could be interpreted as a progradation of the alluvial fan-braided river-fan delta depositional system towards the open lake environment, despite the high-frequency fluctuations of the base level observed on the outcrop scale (Fig. 11). However, dominance of regressive facies was not recorded in the northern sub-basin and the presence of FA2 & FA3 could be aggradational since it is commonly overlain by open lacustrine FA4 (Fig. 14E).

4.3 Geochemistry and mineralogy

The XRF whole rock analyses of mud to sandy mud from alluvial fans (ValLom1, Ondr-1) are characterized by a high proportion of CaO (32–37 wt. %), MgO (14 wt. %), and a low oxide sum (63–67 wt. %) (Fig. 15, Table 6 in Šujan et al., submitted). This indicates a high proportion of carbonate minerals in the composition of the mud, and this is further confirmed by XRD analysis, indicating a 77–78 % dominance of dolomite in whole rock composition (Table 3). The low content of silicate minerals is shown by the amount of Al_2O_3 (2.7–5.6 wt. %), and SiO_2 (5.9–11.4 wt. %) (Fig. 15, Table 6 in Šujan et al., submitted). The Si/Al ratio (1.9) and K_2O/Al_2O_3 (0.15–0.18) point to the high content of clay minerals in the silicate fraction. This is consistent with XRD data (Quartz 5°%; phyllosilicates 17–18°%; Table 3), in which the clay fraction in Ondr-1 is dominated by illite, and both samples contain subordinate quantities of smectite and kaolinite. Samples also display a low content of Fe (0.4–0.6 wt.°% Fe_2O_3). The content of Fe is important due to the binding of Be in Fe-Mn oxyhydroxides. Considering the whole dataset, the amount of Fe is lowest in alluvial fan samples, although $Fe_{(ef)}$ varies from 0.2–0.7 (Table 7 in Šujan et al., submitted).

Samples from braided river mud to sandy mud (Kolísky-3, SocKos-1) document a small increase in the proportion of siliciclastic material (SiO_2 16–18 wt. %; Al_2O_3 6–8 wt. %) (Fig. 15, Table 6 in Šujan et al., submitted). The Si/Al (2.4–2.7) and K_2O/Al_2O_3 (0.14–0.21) proxies point to a lower content of clay (so, more silty grains) in the silicate fraction compared to the alluvial fan samples. The content of CaO (33–49 wt. %) and MgO (6 wt. %) shows a slight decrease in carbonate minerals and an increase in the calcite portion in comparison to alluvial fan samples. This agrees with the XRD analysis, which indicates a composition of 56–69 % carbonate minerals; 20–27 % phyllosilicates and 4 % quartz. The clay fraction is dominated by smectite and illite/smectite. The content of Fe_2O_3 is 2.2 wt. %, and that of $Fe_{(ef)}$ is 0.9–1.2 wt. %, which indicates an increase in Fe content compared to the alluvial fan.

The fan-delta mud to sandy mud of the Blaz-3 sample, as measured by XRF displays a further continual decreasing of carbonate content (CaO 20.7 wt. %; MgO 5.8 wt. %), accompanied by

an increase in the silicate fraction (SiO_2 24.45 wt. %; Al_2O_3 11.8 wt. %) (Fig. 15; Table 6 in Šujan et al., submitted). Si/Al (1.8) and K_2O/Al_2O_3 (0.15) are similar to those in braided rivers (Table 7 in Šujan et al., submitted). In mineral composition, carbonate minerals form only 43 %, with the remainder being made up of phyllosilicates 48 % and quartz 9 % (Table 3). The clay fraction is dominated by smectite.

More detailed mud analyses using ICP-MS and ICP ES were performed on the Blažovce section samples taken from several levels (Table 8 in Šujan et al., submitted; Fig. 11). These data document that the Blaz-1,2,3 samples have a lower content of carbonates (CO_2 16.2–17.8 wt. %) than the Blaz-5 and Blaz-7 samples (CO_2 22.6–24.3 wt. %). Meanwhile, the silicate materials display an opposite trend, in which Blaz-1,2,3 yield figures of 29.4–32.6 wt. % SiO_2 and 14.3–17 wt. % Al_2O_3, with Blaz-5 and Blaz-7 on 23.7–28.8 wt. % SiO_2 and 10.4–11.1 wt. % Al_2O_3 (Fig. 15, Table 8 in Šujan et al., submitted). The Si/Al ratio increases from Blaz-1 (1.8) to Blaz-7 (2.2), a phenomenon which pointed to a decrease in the clay proportion from the Blaz-1 to Blaz-7 samples. The lowermost K_2O/Al_2O_3 (illite proxy) is present in Blaz-5 (0.12), and the highest value (0.18) is in found in Blaz-7. These values are confirmed also by the CIA index and Rb (Table 9 in Šujan et al., submitted). This may be explained by a higher content of sandy/silty grains in Blaz-7. The content of Fe_2O_3 is highest in Blaz-1 and 2 (4.2–4.6 wt. %; $Fe_{(ef)}$ 0.9) and in Blaz-3,5,7 decreases from 2.7 to 1.8 wt. % ($Fe_{(ef)}$ 0.6–0.5), respectively.

The open lake mud to muddy sand (MarTeh-1; TurPet-1; Kudel-1) has the lowest proportion of carbonates (CaO = 5.2–8.5 wt. %; MgO 2.0–2.1 wt. %, Fig. 15, Table 6 in Šujan et al., submitted) and the highest proportion of silicate fraction in its composition (SiO_2 33.5–37.4 wt. %; Al_2O_3 8.9–12.4 wt. %). The Si/Al (2.7–3.3) and K_2O/Al_2O_3 (0.22–0.23) ratios imply that the clay mineral proportion in the silicate fraction is relatively low in comparison with the samples previously described. Kudel-1 probably contains the largest portion of sandy grains (Si/Al 3.3) and carbonate minerals (CaO 8.5 wt. %) of any of the open lake sites; the open lake samples contain 2.0–3.2 wt. % Fe_2O_3 ($Fe_{(ef)}$ 0.6–0.8). These data are consistent with the XRF analysis (MarTeh-1; Tur-Pet-1), in which phyllosilicates comprise 52–53 %, quartz 32–35 % and carbonate minerals 8–16 %. The clay fraction contains approximately the same proportion of illite and smectite, together with a subordinate amount of quartz, chlorite, and kaolinite (Table 3). The results of both analyses document that: (1) these mudstones are siliciclastic; and (2) probably contain the highest proportion of sandy/silty grains of all the measured samples.

Table 3. Quantitative mineral composition of whole rock sample and semi-quantitative mineral composition of the <2 μm fraction obtained by XRD. Phyllosilicate content was determined in the <2 μm fraction of insoluble rock residue. Qz – quartz; Pl – plagioclase; Cal – Calcite; Dol – dolomite; L.c.Vrm – low charge vermiculite/high charge smectite; Vrm – vermiculite; Ilt – illite; Sme – smectite; Sme + S-I – smectite and mixed layer illite-smectite; Kln – kaolinite which does not intercalate with DMSO; KlnD – kaolinite which forms intercalation compounds with DMSO; Chl – chlorite; Chl-S – mixed layer Chlorite – smectite; XXX – dominant (>50 %); XX – abundant (20–50 %); X – subordinate (1–20 %); + - traces (<1%), ? - mineral is probably present in the sample.

sample	**Environment**	**whole rock**					**fraction < 2 μm**									
		Qz	Pl	Cal	Dol	phyllo-silicates	L.c. Vrm	Vrm	Ilt	Sme	Sme + I-S	Kln	KlnD	Chl	Chl-S	Qz	Dol
MarTeh-1	open lake	32		11	5	52			XX	XX		X	-	X		X	
Tur-Pet-1	open lake	39		8		53		X	XX	XX		X	-	X		X	
Blaz-3	fan delta	9		16	27	48			XX	XXX		X	X	X		X	
SocKos-1	braided river	4		34	35	27		X	X		XXX	X	+			+	X
Kolisky-3	braided river	4		60	16	20			X		XXX	X	X			+	
Ondr-1	alluvial fan	5			78	17	X		XXX	+		X	X			?	X
ValLom-1	alluvial fan	5			77	18		X	XX	X		X	X			-	XX
Vel-Cep-2	alluvial fan	26	7			67			XX		XX	X	X		X	X	
Kost-Q-1	floodplain	31	5		38	26			XX		XXX	X	-	X		X	
Kalam-Q-1	floodplain	40	5			55			XX		X	XX	X	X		X	
MalCep-3	river terrace	34	8		35	23			XX	XX		X	-			X	

Four samples taken from initial ratio sites of Late Pleistocene to Holocene age were also analysed using XRF and XRD (MalCep-3; VelCep-2; Kalam-Q-1; Kost-Q-1). The samples vary in their content of carbonate minerals, over a range of 0–35 %, which is offset by an increase in the content of 23–67 % in phyllosilicates and 26–40 % in quartz (Table 3). The content of Fe_2O_3 (3–5 wt. %), $Fe_{(ef)}$ (0.7–1.3), Si/Al (2.2–3.1), and K_2O/Al_2O_3 (0.11–0.19) is similar to open lake samples (Table 7 in Šujan et al., submitted). From these samples, Vel-Cep-2 displayed the highest content of clay fraction (Si/Al 2.22; 67 % phyllosilicates) and $Al_{(UCC)}$ 1.05 (Table 3, Table 7 in Šujan et al., submitted). On the other hand, the clay fraction of VelCep-2 and MalCep-3 consists of approximately the same proportion of illitic material and smectite or mixed layer illite/smectite. KOS-Q-1 is dominated by smectite and illite/smectite; while Kalam-Q-1 contains an increased proportion of kaolinite.

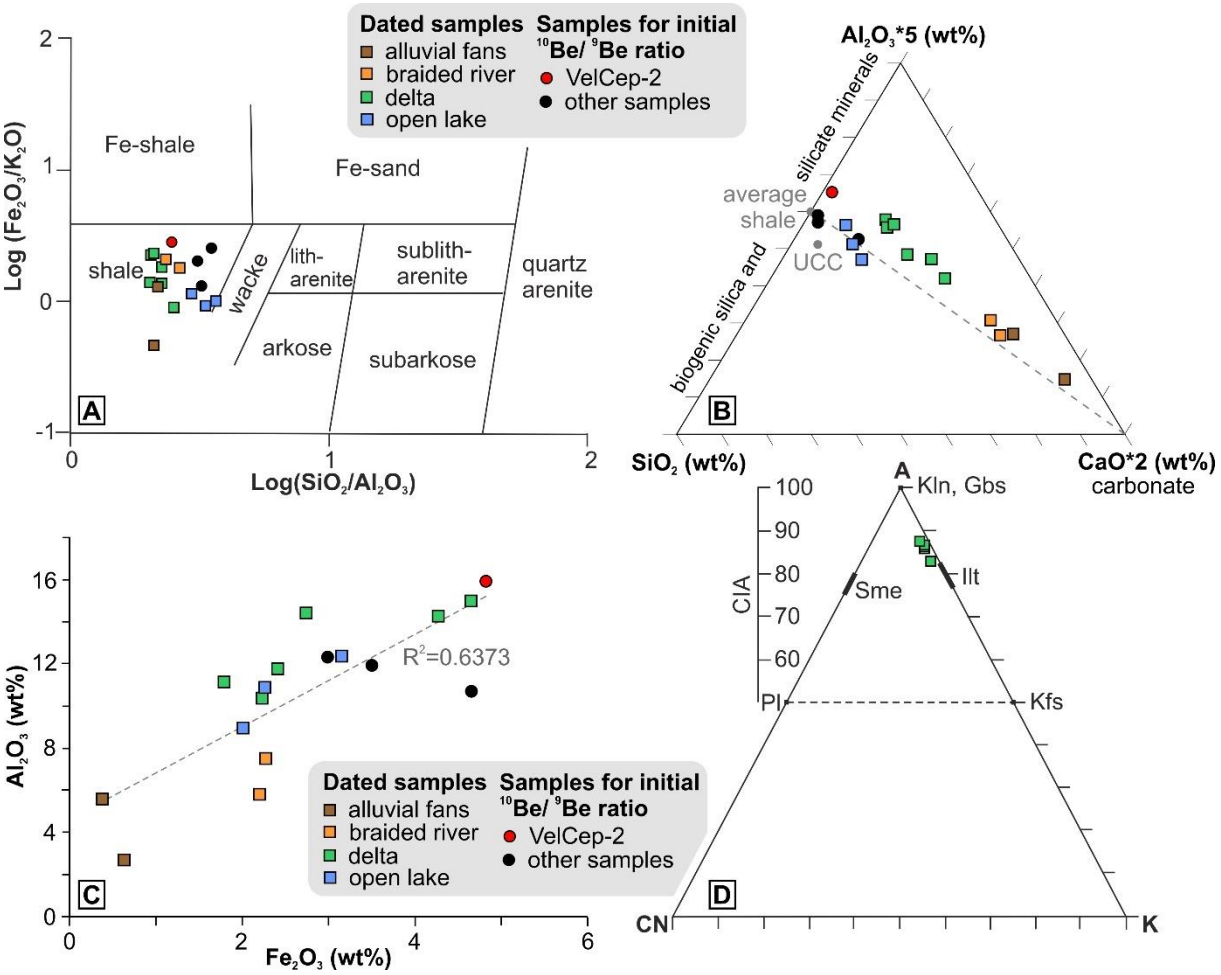

Fig. 15. Geochemical characterization of the samples selected from dated sites and sites evaluated for determination of the initial $^{10}Be/^{9}Be$ ratio. A. Classification of muddy samples according to Herron (1988). B. Composition of mud according to Brumsack (1989) shows a continuous decrease of carbonate component from alluvial fans towards the open lake environment. C. Relationship between Al_2O_3 and $Fe_2O_{3\ (tot)}$, showing an increase in Fe together with the siliciclastic fraction in the samples analysed. D. A-CN-K diagram showing degree of weathering in source area (Nesbitt and Young, 1982).

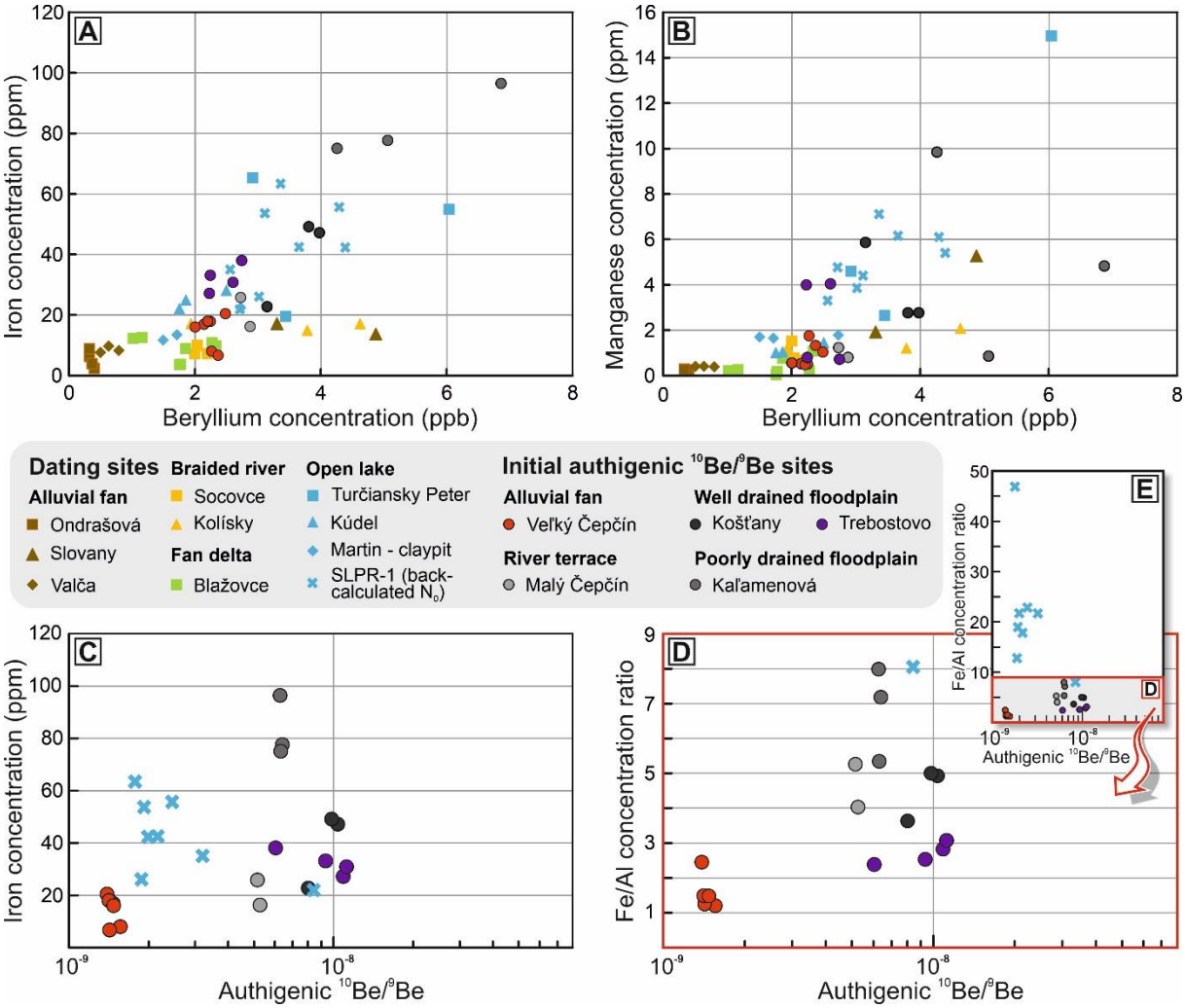

Fig. 16A,B. Concentrations of iron and manganese plotted against the beryllium concentrations in the authigenic phase for all analyzed samples. Note the divergence of the poorly and well drained floodplain sites (Kaľamenová and Košťany nad Turcom, partly Trebostovo) from the main set of dating site samples, as well as the consistency of the Veľký Čepčín site values with the main set of dating samples of the terrestrial origin. The measured values are included in Šujan et al. (2022). C,D. Authigenic $^{10}Be/^{9}Be$ of the sites sampled for initial ratio determination plotted against the concentration of iron and Fe/Al ratio. The increased concentration of iron in the authigenic phase generally correlates with increased authigenic $^{10}Be/^{9}Be$ (C). The different appearance of the sites is evident when concentration of iron is normalized to aluminum (D). The SLPR-1 open lacustrine samples show highly increased Fe/Al ratio (E) which means enhanced growth of the authigenic phase with only slightly increased $^{10}Be/^{9}Be$ due to the higher input of ^{10}Be to the lake from meteoric waters.

The ICP-MS analyzes of the authigenic phase were mainly focused on the comparison between the main batch of the dating samples of all studied sites, the samples taken from five sites selected for establishment of the authigenic $^{10}Be/^{9}Be$ initial ratio (Veľký Čepčín, Malý Čepčín, Košťany, Kaľamenová, Trebostovo) and the SLPR-1 samples aimed for back-calculation of the lacustrine initial ratio. The plots of beryllium concentrations against iron and manganese show a relatively homogeneous set of almost all samples of the dating sites. The lacustrine sites show generally higher values, especially in the case of the Turčiansky Peter site and SLPR-1 well (Fig. 16). When considering the sites selected for initial $^{10}Be/^{9}Be$ ratio determination, a

significant deviation of the floodplain samples taken from Kaľamenová and Košťany nad Turcom with correlating increased concentrations of Be and Fe could be established (Fig. 16A), while the Trebostovo show less pronounced deviation. Moreover, the values of Be against Mn concentrations show a similar but not so pronounced pattern. The Veľký Čepčín site appears to be consistent with the main set of dating samples (Fig. 16B). The open lacustrine samples show a relatively wide dispersal of values on both plots.

4.4 Authigenic $^{10}Be/^{9}Be$ dating

4.4.1 Initial $^{10}Be/^{9}Be$ ratios

The authigenic $^{10}Be/^{9}Be$ ratios calculated for the initial ratio samples taken from the Pleistocene-Holocene sites (<200 ka) range from $143.36 \pm 1.41 \times 10^{-11}$ to $1118.11 \pm 16.78 \times 10^{-11}$ (Table 4, Fig. 17). Despite this difference of one order of magnitude between sites, the variability of values within each site is low, except for the outlier appearing at the Košťany nad Turcom site (Kost-Q-1) and the Trebostovo site (Treb-1-2). Sample VelCep-1 was also considered an outlier during the calculation of weighted mean isotopic ratios using the KDX application by Spencer et al. (2017). The low degree of within-site variability allowed us to calculate weighted mean isotopic ratios for each site in the range of 143.40×10^{-11} to $1034.72 \pm 16.78 \times 10^{-11}$ (Table 4). The weighted mean values obtained from the five analyzed sites are used for age calculations as the initial authigenic $^{10}Be/^{9}Be$ ratio.

The sixth initial ratio was back-calculated using the samples of the lacustrine Martin Fm. from the borehole core SLPR-1 dated by magnetostratigraphy to 7.7–8.1 Ma (Márton et al., 2022). The measured natural $^{10}Be/^{9}Be$ values exhibit a low variability in the range of $3.43 \pm 0.19 \times 10^{-11}$ to $5.09 \pm 0.26 \times 10^{-11}$, except one outlier at the depth of 59.6 m (Fig. 18, Table 5). The back-calculated paleo-initial ratio based on the seven samples yielded the value of $205.83 \pm 10.27 \times 10^{-11}$.

Table 4: Concentrations of ^{9}Be and ^{10}Be, natural $^{10}Be/^{9}Be$ ratios and weighted mean initial ratios (N_0) determined in the Turiec Basin from late Middle Pleistocene and Holocene localities (<200 ka). Uncertainties are σ_1. Concentrations of ^{10}Be are corrected to the $^{10}Be/^{9}Be$ ratios of eight processing blanks reaching values in the range of 6.61×10^{-15} to 9.62×10^{-15}. * - Values considered as outliers (see text).

ID	Locality	^{9}Be (at × g^{-1}) × 10^{16}	AMS $^{10}Be/^{9}Be$ (× 10^{-14})	^{10}Be (at × g^{-1}) × 10^{6}	Natural $^{10}Be/^{9}Be$ (× 10^{-11})	Weghted mean initial $^{10}Be/^{9}Be$ ratio (× 10^{-11})
VelCep-1*	Veľký Čepčín - late Middle Pleistocene alluvial fan	5.232 ± 0.105	265.832 ± 4.141	81.654 ± 1.272	156.071 ± 3.957	143.36 ± 1.41
VelCep-2		5.817 ± 0.116	270.068 ± 4.369	82.75 ± 1.339	142.252 ± 3.659	
VelCep-3		6.448 ± 0.129	297.820 ± 4.693	89.708 ± 1.414	139.127 ± 3.543	
VelCep-4		6.237 ± 0.128	292.480 ± 3.601	89.165 ± 1.099	142.970 ± 3.358	
VelCep-5		6.003 ± 0.123	289.256 ± 3.545	88.146 ± 1.081	146.835 ± 3.444	
VelCep-6		6.365 ± 0.131	293.137 ± 3.627	90.023 ± 1.115	141.434 ± 3.326	
VelCep-7		5.443 ± 0.111	261.065 ± 3.246	80.249 ± 0.998	147.407 ± 3.471	
MalCep-3	Malý Čepčín - Late Pleistocene river terrace	6.725 ± 0.134	1155.94 ± 14.491	354.221 ± 4.441	526.744 ± 12.433	520.92 ± 8.69
MalCep-4		6.176 ± 0.124	1038.65 ± 12.951	318.267 ± 3.969	515.355 ± 12.146	
Kalam-Q-1	Kaľamenová - Holocene Turiec River floodplain	11.193 ± 0.224	2342.33 ± 29.157	715.313 ± 8.904	639.047 ± 15.054	632.81 ± 8.61
Kalam-Q-2		9.441 ± 0.189	1980.38 ± 24.796	596.148 ± 7.464	631.42 ± 14.899	
Kalam-Q-3		15.606 ± 0.312	3177.10 ± 39.294	980.336 ± 12.125	628.172 ± 14.772	
Kost-Q-1*	Košťany - Holocene Turiec River floodplain	7.715 ± 0.154	2026.705 ± 25.274	619.064 ± 7.72	802.433 ± 18.913	1007.56 ± 16.78
Kost-Q-2		9.339 ± 0.187	3264.765 ± 40.719	968.803 ± 12.083	1037.41 ± 24.452	
Kost-Q-3		8.664 ± 0.173	2759.251 ± 34.200	849.941 ± 10.535	980.968 ± 23.082	
Treb-1-1	Trebostovo - latest Pleistocene to Holocene alluvial fan	5.002 ± 0.053	1537.290 ± 22.786	466.380 ± 6.913	932.445 ± 23.212	1034.72 ± 29.26
Treb-1-2*		6.040 ± 0.105	1205.500 ± 17.827	364.410 ± 5.389	603.377 ± 15.009	
Treb-2-1		5.985 ± 0.062	2202.470 ± 29.877	669.210 ± 9.078	1118.110 ± 27.021	
Treb-2-2		4.992 ± 0.100	1791.900 ± 24.347	542.634 ± 7.373	1086.927 ± 26.281	

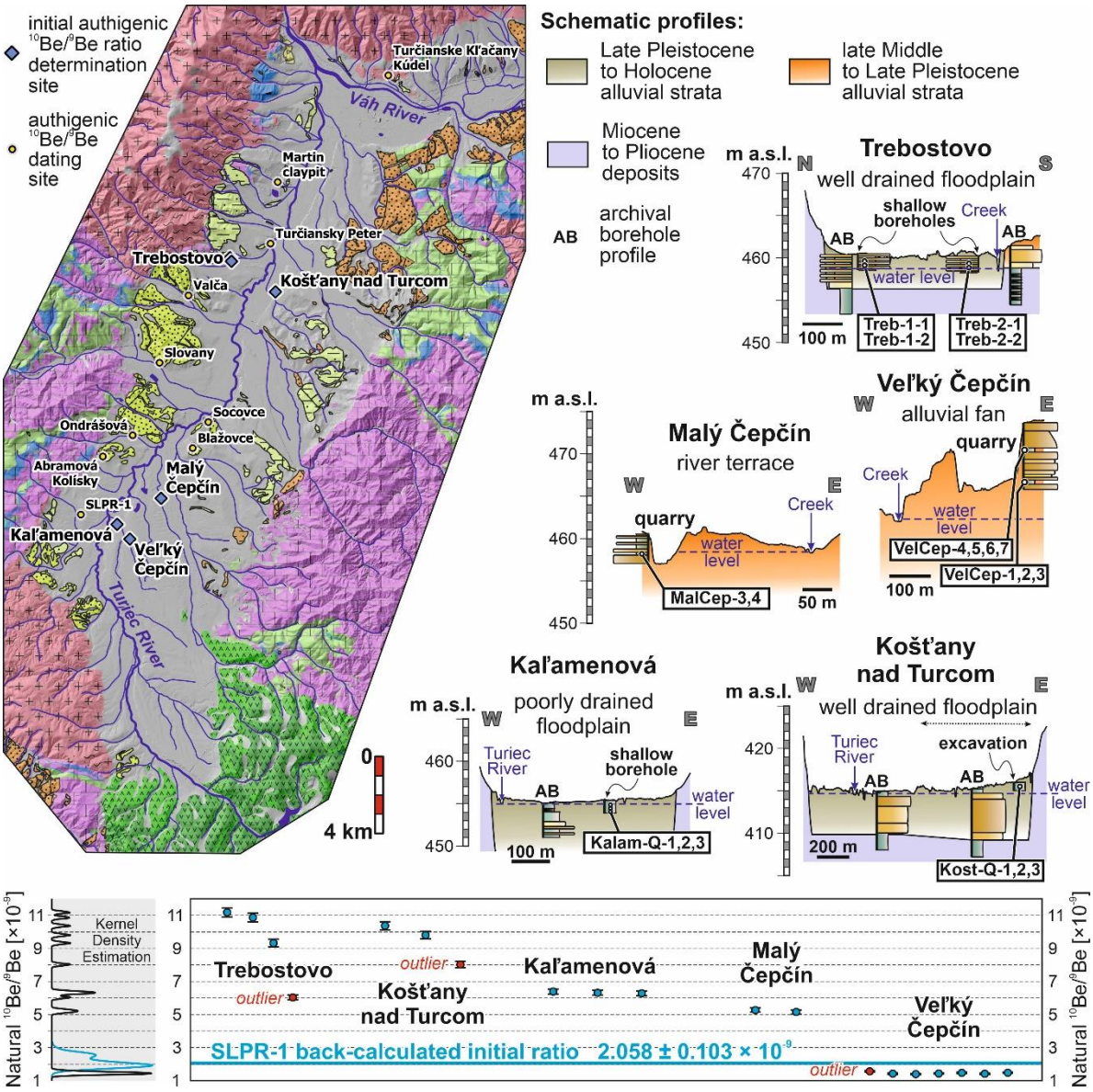

Fig. 17. Geological settings of the sites selected for determination of initial $^{10}Be/^{9}Be$ ratio, and distribution of natural authigenic $^{10}Be/^{9}Be$ values for all samples. The Kernel Density Estimation was produced by the KDX application (Spencer et al., 2017). Explanations of the simplified geological map of pre-Quaternary units is in Fig. 2B. An explanation of the lithological logs is in Fig. 2 of Šujan et al. (submitted) and in Fig. 18. Archival borehole lithological profiles were obtained from the Geofond archive of the State Geological Institute of Dionýz Štúr (Slovak Geological Survey).

Table 5: Concentrations of ^{9}Be and ^{10}Be, natural $^{10}Be/^{9}Be$ ratios, back-calculated $^{10}Be/^{9}Be$ using the age range constrained by magnetostratigraphy to 7.7.–8.1 Ma (Márton et al., 2022) and weighted mean paleo-initial ratio (N_0) determined in for the samples of the SLPR-1 borehole core. Uncertainties are σ_1. The uncertainty of paleo-N_0 values includes the $^{10}Be/^{9}Be$ range for 7.7–8.1 Ma and the analytical uncertainty. Concentrations of ^{10}Be are corrected to the $^{10}Be/^{9}Be$ ratios of one processing blanks reaching value in the range of 3.64×10^{-14}. * - Values considered as outliers (see text).

ID	Stratigraphy	^{9}Be (at × g^{-1}) × 10^{16}	AMS $^{10}Be/^{9}Be$ (× 10^{-14})	^{10}Be (at × g^{-1}) × 10^{6}	Natural $^{10}Be/^{9}Be$ (× 10^{-11})	Paleo-$^{10}Be/^{9}Be$ (7.7 Ma) (× 10^{-9})	Paleo-$^{10}Be/^{9}Be$ (8.1 Ma) (× 10^{-9})	Paleo-N_0 (× 10^{-9})	Weighted mean paleo-N_0 (× 10^{-11})
SLPR-1-19.7	Martin Fm.	9.883 ± 0.203	18.832 ± 0.565	4.644 ± 0.163	4.699 ± 0.190	2.693	2.213	2.453 ± 0.301	205.83 ± 10.27
SLPR-1-29.5		6.960 ± 0.139	11.923 ± 0.371	2.514 ± 0.115	3.613 ± 0.180	2.070	1.686	1.878 ± 0.248	
SLPR-1-39.4		9.755 ± 0.235	16.050 ± 0.533	3.731 ± 0.150	3.825 ± 0.172	2.192	1.793	1.993 ± 0.254	
SLPR-1-59.6*		5.765 ± 0.078	15.296 ± 0.480	3.539 ± 0.139	6.138 ± 0.271	3.517	2.880	3.198 ± 0.405	
SLPR-1-68.0		7.023 ± 0.140	12.130 ± 0.407	2.598 ± 0.121	3.699 ± 0.188	2.120	1.725	1.922 ± 0.256	
SLPR-1-78.1		7.661 ± 0.129	12.240 ± 0.475	2.627 ± 0.132	3.429 ± 0.186	1.965	1.593	1.779 ± 0.243	
SLPR-1-88.8		8.413 ± 0.160	15.184 ± 0.729	3.516 ± 0.189	4.179 ± 0.239	2.395	1.936	2.165 ± 0.303	
SLPR-1-99.5		6.243 ± 0.126	14.071 ± 0.546	3.177 ± 0.149	5.088 ± 0.260	2.387	3.058	2.651 ± 0.336	

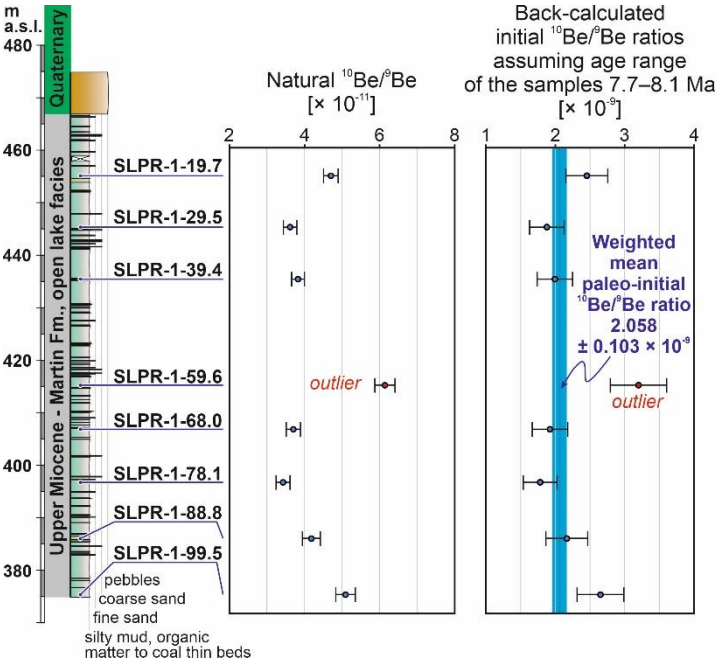

Fig. 18. Lithological profile of the SLPR-1 borehole core, dated independently to 7.7–8.1 Ma (Márton et al., 2022). The samples were used for back-calculation of the paleo-initial authigenic $^{10}Be/^{9}Be$ ratio. Values are present in Table 5.

4.4.2 Dating results

The authigenic $^{10}Be/^{9}Be$ isotopic ratios of the dating samples range from $0.87 \pm 0.06 \times 10^{-11}$ to $56.62 \pm 1.65 \times 10^{-11}$ (Table 6, Table 10 in Šujan et al., submitted). The depositional ages for all 31 samples using the five initial ratios are included in Table 10 of Šujan et al. (submitted). The age uncertainties propagate from the uncertainty of the corresponding initial ratio, analytical error of measured natural $^{10}Be/^{9}Be$ ratio, and uncertainty in the half-life of ^{10}Be. The within-site variability of $^{10}Be/^{9}Be$ isotopic ratios and calculation of weighted mean ages are further discussed in chapter 5.1, together with the reasoning for the initial ratio selection.

Table 6: Concentrations of ^{9}Be and ^{10}Be, natural $^{10}Be/^{9}Be$ ratios and authigenic $^{10}Be/^{9}Be$ ages for the analyzed samples, calculated using the Veľký Čepčín initial ratio (N_0) for alluvial fan, braider river and fan delta sites, and using the SLPR-1 back-calculated initial ratio for the open lake sites. The weighted mean ages were calculated using the KDX application (Spencer et al., 2017). Uncertainties are σ_1. Concentrations of ^{10}Be are corrected to the $^{10}Be/^{9}Be$ ratios of eight processing blanks reaching values in the range of 6.61×10^{-15} to 9.62×10^{-15}. * - Values considered as outliers (see text).

ID	Locality	Stratigraphy	^{9}Be (at × g^{-1}) × 10^{16}	AMS $^{10}Be/^{9}Be$ (× 10^{-14})	^{10}Be (at × g^{-1}) × 10^{6}	Natural $^{10}Be/^{9}Be$ (× 10^{-11})	Age (Ma) - Veľký Čepčín (1) or SLPR-1 (2) N_0	Weighted mean age (Ma)
Ondr-1	Ondrašová	Alluvial fan - Slovany Mb.	0.999 ± 0.020	2.372 ± 0.112	0.523 ± 0.030	5.236 ± 0.321	6.624 ± 0.429 (1)	n.a.
Ondr-2			0.777 ± 0.016	3.831 ± 0.145	0.970 ± 0.041	12.481 ± 0.581	4.885 ± 0.249 (1)	
Ondr-3			0.862 ± 0.017	2.464 ± 0.102	0.548 ± 0.029	6.357 ± 0.356	6.235 ± 0.373 (1)	
Ondr-4			0.777 ± 0.016	3.493 ± 0.115	0.860 ± 0.033	11.059 ± 0.482	5.127 ± 0.248 (1)	
Slov-1	Slovany		12.743 ± 0.255	36.980 ± 0.891	11.037 ± 0.267	8.662 ± 0.272	5.616 ± 0.211 (1)	n.a.
Slov-2			7.678 ± 0.154	46.427 ± 1.224	13.848 ± 0.366	18.036 ± 0.598	4.149 ± 0.162 (1)	
ValLom-1	Valča		1.461 ± 0.029	3.866 ± 0.167	0.939 ± 0.045	6.427 ± 0.331	6.214 ± 0.345 (1)	6.394 ± 0.195
ValLom-2			1.937 ± 0.039	4.485 ± 0.150	1.114 ± 0.042	5.753 ± 0.243	6.435 ± 0.304 (1)	
ValLom-3			1.178 ± 0.024	2.846 ± 0.116	0.640 ± 0.032	5.436 ± 0.294	6.549 ± 0.379 (1)	
SocKos-1	Socovce	Braided river - Abramová Mb.	5.079 ± 0.102	9.729 ± 0.309	2.675 ± 0.087	5.267 ± 0.202	6.612 ± 0.288 (1)	6.432 ± 0.162
SocKos-2			4.708 ± 0.094	9.605 ± 0.315	2.657 ± 0.089	5.643 ± 0.221	6.474 ± 0.287 (1)	
SocKos-3			4.672 ± 0.093	10.536 ± 0.329	2.966 ± 0.095	6.349 ± 0.239	6.238 ± 0.269 (1)	
Kolisky-1	Abramová - Kolísky		4.594 ± 0.092	5.205 ± 0.165	1.364 ± 0.047	2.968 ± 0.118	7.759 ± 0.349 (1)	7.469 ± 0.231
Kolisky-2*			10.721 ± 0.214	6.790 ± 0.213	1.846 ± 0.060	1.721 ± 0.066	8.849 ± 0.384 (1)	
Kolisky-3			8.719 ± 0.174	11.685 ± 0.361	3.348 ± 0.105	3.840 ± 0.142	7.244 ± 0.308 (1)	
Blaz-1*	Blážovce	Fan delta - Blážovce Mb.	2.065 ± 0.041	7.888 ± 0.245	2.101 ± 0.068	10.176 ± 0.389	5.294 ± 0.230 (1)	6.697 ± 0.135
Blaz-2			2.716 ± 0.054	5.042 ± 0.167	1.228 ± 0.045	4.523 ± 0.190	6.917 ± 0.325 (1)	
Blaz-3			4.387 ± 0.088	9.115 ± 0.316	2.508 ± 0.089	5.717 ± 0.233	6.448 ± 0.295 (1)	
Blaz-4*			4.076 ± 0.082	75.787 ± 1.620	23.079 ± 0.494	56.622 ± 1.659	1.859 ± 0.067 (1)	
Blaz-5			5.418 ± 0.108	11.134 ± 0.391	3.105 ± 0.111	5.731 ± 0.235	6.443 ± 0.296 (1)	
Blaz-6			5.187 ± 0.104	6.836 ± 0.212	2.490 ± 0.080	4.800 ± 0.181	6.798 ± 0.293 (1)	
Blaz-7			4.097 ± 0.082	6.826 ± 0.216	1.841 ± 0.062	4.494 ± 0.175	6.929 ± 0.306 (1)	
TurPet-1	Turčiansky Peter	Open lake - Turiec Fm.	8.108 ± 0.162	5.975 ± 0.193	1.605 ± 0.054	1.980 ± 0.077	9.233 ± 0.619 (2)	8.904 ± 0.343
TurPet-2			14.001 ± 0.280	11.741 ± 0.362	3.373 ± 0.105	2.409 ± 0.089	8.840 ± 0.582 (2)	
TurPet-3			7.203 ± 0.144	7.251 ± 0.233	1.882 ± 0.064	2.613 ± 0.103	8.677 ± 0.583 (2)	
Kudel-1	Kúdel		4.105 ± 0.082	2.648 ± 0.105	0.575 ± 0.027	1.401 ± 0.072	9.924 ± 0.745 (2)	9.871 ± 0.103

Kudel-2			4.328 ± 0.087	2.843 ± 0.100	0.638 ± 0.027	1.473 ± 0.069	9.824 ± 0.707 (2)	
Kudel-3*			5.879 ± 0.118	16.734 ± 0.522	4.886 ± 0.153	8.310 ± 0.309	6.362 ± 0.420 (2)	
MarTeh-1	Martin - claypit		6.185 ± 0.124	2.691 ± 0.097	0.591 ± 0.028	0.956 ± 0.050	10.690 ± 0.805 (2)	
MarTeh-2			3.352 ± 0.067	1.723 ± 0.075	0.295 ± 0.023	0.880 ± 0.070	10.856 ± 1.046 (2)	10.667 ± 0.518
MarTeh-3			3.850 ± 0.077	2.077 ± 0.084	0.404 ± 0.025	1.049 ± 0.068	10.503 ± 0.888 (2)	

5. Discussion

5.1 Authigenic $^{10}Be/^{9}Be$ geochronology

5.1.1 Initial ratio variability: (post-)depositional processes, provenance and depositional system complexity

The meteoric ^{10}Be concentration in an authigenic phase may change as a result of exposure of a soil profile to meteoric waters and will depend on the duration as well as intensity of the exposure due to the retention of beryllium and its possible mobility in positive water balance settings (Tsai et al., 2008; Graly et al., 2010; Willenbring and von Blanckenburg, 2010; Bacon et al., 2012; Dixon et al., 2018). The rate of burial of sedimentary strata provides a possible clue to resolve the observed initial $^{10}Be/^{9}Be$ ratio variability in the Turiec Basin across one order of magnitude, since it affects duration and magnitude of pedogenesis.

The lowest ratio of $143.36 \pm 1.41 \times 10^{-11}$ was measured at the Veľký Čepčín site (Table 4), a late Middle Pleistocene alluvial fan where the sediment supply was high, and therefore where strata were buried abruptly. The Malý Čepčín site, a Late Pleistocene river terrace, accumulated in conditions of lower sediment supply and exhibits a higher isotopic ratio of $520.92 \pm 8.69 \times 10^{-11}$. The highest isotopic ratios of $632.81 \pm 8.61 \times 10^{-11}$, $1007.56 \pm 16.78 \times 10^{-11}$ and $1034.72 \pm 29.26 \times 10^{-11}$ were established at the three sites of Holocene river floodplains (Košťany, Kaľamenová and Trebostovo), sites with low sediment supply to accommodation rate ratio (Fig. 17).

The five sites differ in their positions relative to the present-day groundwater level (Fig. 17), which is relevant to the intensity of pedogenesis and potential post-depositional precipitation of authigenic rims. The Veľký Čepčín alluvial fan forms a topographic elevation with reduced potential for post-depositional precipitation, in contrast to the floodplain and river terrace sites, which are within the range of the present groundwater level. Moreover, the Holocene floodplain samples contain a higher proportion of smectite and/or kaolinite at the expense of illite or illite/smectite in comparison to the Late Pleistocene ones, a phenomenon which implies a higher intensity of chemical weathering over the course of their existence in the sampled sedimentary profile. The Košťany nad Turcom, Kaľamenová and Trebostovo sites show increased concentrations of Fe and Mn in correlation with high Be content in the authigenic phase (Fig. 16A,B). Finally, the increased concentration of iron in the authigenic phase correlates with the increase of $^{10}Be/^{9}Be$ (Fig. 16C), and even more pronounced difference of the floodplain and alluvial fan sites is shown when normalizing the iron concentration using low-mobility aluminum (Fig. 16D).

Hence, the mentioned observations support the hypothesis of different authigenic rim growth history of the floodplain environment in comparison to the Veľký Čepčín alluvial fan due to the differences in the pace of burial and in the predisposition to post-depositional alteration of the authigenic $^{10}Be/^{9}Be$ ratio.

The relationship between the beryllium isotopic ratios and the sediment provenance could be evaluated from the present-day drainage pattern (Fig. 17) and the published petrography of the analyzed sites (Tužinský et al., 1967; Gašparík and Halouzka, 1993; Kováč et al., 2011; Holec and Braucher, 2014). The drainage basins are composed of carbonates with expected low ^{9}Be concentration, andesites which generally have higher ^{9}Be contend and granitoids usually most abundant on ^{9}Be (Ryan, 2002; Suhrhoff et al., 2019). In contrary to what would be expected if provenance is the main factor affecting the resulting authigenic $^{10}Be/^{9}Be$ ratio, the highest and

almost identical values were measured at the Trebostovo site with drainage basin formed purely by granitoids and at the Košťany nad Turcom site with prevalence of carbonates over granitoids. These are followed by somewhat lower value from the Kaľamenová site having granitoids and volcanites in its clast composition. The lowest value yielded the Veľký Čepčín site, and the $^{10}Be/^{9}Be$ ratio is stable along the profile despite the balanced proportion of carbonates and granitoids in the lower part and dominance of carbonates in the upper part of the section. Thus, the observed variability in the initial $^{10}Be/^{9}Be$ ratio does not exhibit a dependence on the provenance of the analyzed sediment. This notion is not unexpected, since the initial $^{10}Be/^{9}Be$ ratios of major river floodplains in the Danube Basin with various provenance yielded insignificant variability (Šujan et al., 2016).

The Veľký Čepčín site is considered to be a good equivalent to the Upper Miocene dated sites formed by alluvial fans, braided rivers and fan deltas, since the succession accumulated in similar conditions of high sediment supply to accommodation rate ratio. The high rate of deposition might be expected to decrease the intensity of post-depositional processes as well as the input of ^{10}Be from meteoric water and groundwater precipitation, and these conditions were likely similar to the Veľký Čepčín site and the dated alluvial fan, braided river and fan delta sites. Moreover, it was shown that the intensity of denudation significantly affects the authigenic $^{10}Be/^{9}Be$ ratio (Willenbring and von Blanckenburg, 2010; von Blanckenburg and Bouchez, 2014), and the FA1, FA2 and FA3 inventory implies similar denudation conditions for sources of sediment in the dated depositional systems and the Veľký Čepčín site. Hence, the Veľký Čepčín initial ratio was selected for age calculation of the Upper Miocene fan delta, alluvial fan and braided river outcrops.

Such an input of ^{10}Be enhanced by pedogenesis as is shown by the floodplain initial ratio sites could not be expected in the case of the dated open lacustrine strata, which experienced a relatively rapid deposition as well, with the accommodation rates in the range of 200–250 $m \cdot Ma^{-1}$. The back-calculated paleo-initial ratio based on the samples from SLPR-1 agrees well with this assumption, having the value of $205.83 \pm 10.27 \times 10^{-11}$ close to the one determined at the Veľký Čepčín site. A relatively wide dispersal of the concentrations of Be, Fe and Mn (Fig. 16A,B) indicates that the duration of the authigenic rim growth was variable in the case of the lacustrine samples. The very high SLPR-1 sample values of Fe/Al indicate a rim growth in basinal waters (Fig. 16E). Nevertheless, the low $^{10}Be/^{9}Be$ ratios and their reduced variability supports the assumption that the beryllium isotope concentrations in basinal waters were well mixed and not significantly different from the regressive alluvial depositional system environment (Fig. 16D,E). The SLPR-1 initial ratio was further used for age calculations in the case of open lacustrine sites (FA4).

A common approach established for the dating of the Upper Miocene successions of the Pannonian Basin System (PBS) relies on changes in the initial $^{10}Be/^{9}Be$ ratio due to (1) sediment source proximity affecting relative ^{9}Be delivery and (2) the depositional rate driving a penecontemporary relative increase of ^{10}Be from the basinal waters (Šujan et al., 2016; Magyar et al., 2019; Joniak et al., 2020; Šujan et al., 2020). The paleoenvironmental variability is projected in the usage of riverine and lacustrine initial ratios for different environments in PBS (Šujan et al., 2016). However, Lake Turiec represented a spatially restricted water mass, much less complex than Lake Pannon, which was, after all, several orders of magnitude larger and deeper (Magyar et al., 2013). Preliminary research on deltaic parasequences implies a low initial $^{10}Be/^{9}Be$ ratio variability in deltaic systems (Aherwar et al., 2022), in contrast with deep-water systems with a prograding shelf slope (Šujan et al., 2016; Wittmann et al., 2017). Therefore, we suggest that the degree of paleoenvironmental variability of the Late Miocene depositional systems filling the Turiec Basin was in all probability not high enough to produce significant spatial differences in the initial authigenic $^{10}Be/^{9}Be$ ratio, and that therefore the N_0 from Veľký

Čepčín for terrestrial deposits and SLPR-1 N_0 for lacustrine facies exhibit close values and are selected for age calculations.

5.1.2 Authigenic $^{10}Be/^{9}Be$ ages and independent age proxies

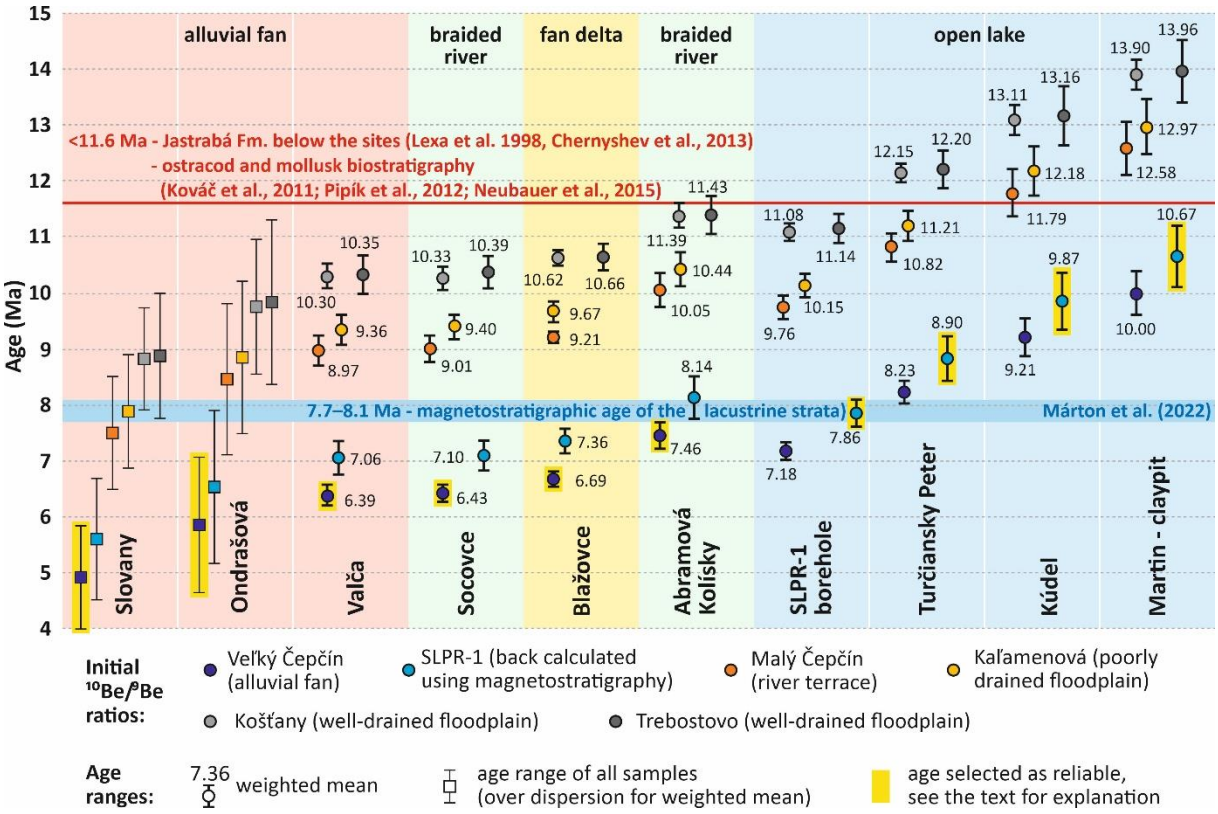

Fig. 19. Comparison of the independent age proxies with the weighted mean ages or age ranges of the dated sites using all six established initial ratios.

A comparison of the ages based on all six initial ratios (Fig. 19; Table 10 in Šujan et al., submitted) implies the suitability of the use of SLPR-1 initial ratio for lacustrine sites, because only this value (except the Veľký Čepčín N_0) yielded ages in agreement with independent age proxies indicating that the studied part of the Martin Formation cannot be older than 11.6 Ma. These proxies include ostracod biostratigraphy (Kováč et al., 2011; Pipík et al., 2012), mollusk biostratigraphy (Neubauer et al., 2015) and dating of the volcano-sedimentary Jastrabá Fm. (Lexa et al. 1998, Chernyshev et al., 2013). On the other hand, the Veľký Čepčín initial ratio allows the calculation of the age of deltaic sediments at the Blažovce site, which is younger than the SLPR-1 succession, in agreement with the observed stratigraphy and confirming the consistency of both initial ratios. The age of alluvial fan sites based on Veľký Čepčín N_0 is younger than the SLPR-1 succession and coeval and younger than the Blažovce deltaic site, consistent with their position within the basin fill.

Table 6 includes the 31 ages calculated using the Veľký Čepčín and SLPR-1 initial ratios, respectively, and Fig. 20 shows the distribution of these ages. The low variability within sites allowed us to calculate weighted mean ages using the KDX application (Spencer et al., 2017); this was done directly for the Valča, Socovce, Martin – claypit and Turčiansky Peter sites. Outliers appeared at the Kúdel (Kudel-3), Abramová - Kolísky (Kolisky-2) and Blažovce sites (Blaz-1 and Blaz-4), and weighted mean ages were calculated only after excluding these. The four samples from the Ondrašová site yielded ages with a wide scatter, which prevented a weighted mean age calculation and the same is valid for the two samples from the Slovany site.

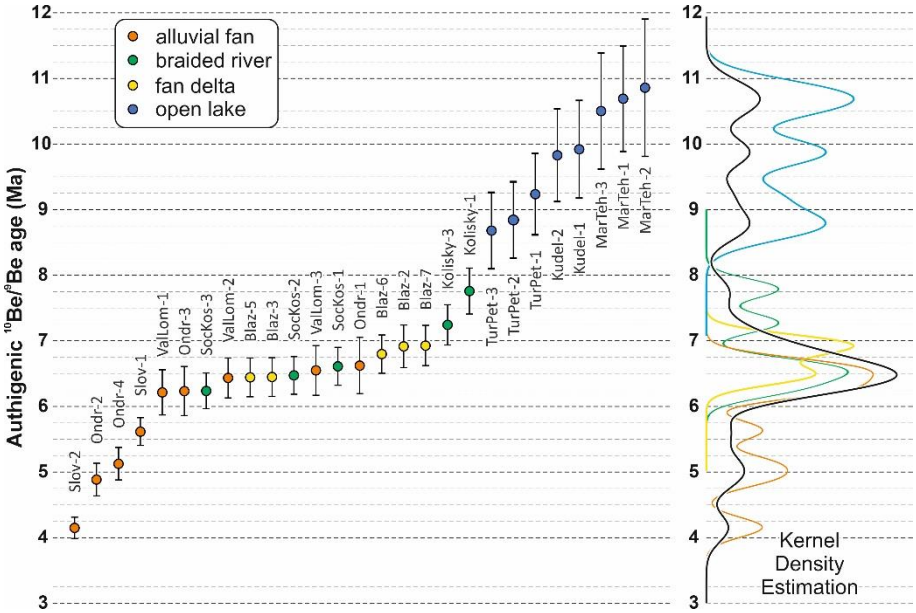

Fig. 20. Cumulative distribution of the authigenic $^{10}Be/^{9}Be$ ages of all dated localities with the absence of four excluded outliers (Blaz-1, Blaz-4, Kolisky-2, Kudel-3). The distribution of values indicates the culmination of the sediment supply at ~7.1–6.0 Ma with a peak at ~6.5 Ma. The samples from SLPR-1 well are not included due to their use for back-calculation of the lacustrine initial $^{10}Be/^{9}Be$ ratio. Kernel Density Estimation yielded by the KDX application (Spencer et al., 2017). The black line in the KDE plot represents the distribution of all samples.

5.1.3 Did hydrological separation of sub-basins with different provenance hinder the beryllium isotope mixing?

Although the initial ratios as well as the ages for all facies associations were established in the southern sub-basin, only the open lacustrine sites were dated in the northern one, and without a suitable initial ratio available in this area (Fig. 2; Fig. 17). The northern drainage with a higher proportion of granitoids could induce a higher input of ^{9}Be, which may lead to apparently older ages, especially in the case of poor mixing of waters between the sub-basins divided by a sill (Fig. 2A). The petrographic properties of the analyzed samples indicate a change in the provenance between the open lake sites. The age of the Martin Fm. increasing northwards can possibly point to such an effect.

Presence of the fan delta and/or braided river facies associations in the vicinity of the Turčiansky Peter (~8.7 Ma) and Martin – claypit (~10.7 Ma) (Fig. 14) could be proposed as another indication that the outcrops should have younger age, concurrent to the timing of the regression in the southern sub-basin. Nevertheless, these FA2 & FA3 deposits can represent an aggradational occurrence of the Abramová member along the margin, as it appeared for the whole Late Miocene cycle of the Turiec Basin (Fig. 3). This puzzle could not be resolved due to the absence of the regressive facies in the northern sub-basin caused by the subsequent denudation.

On the other hand, the low variability of the authigenic $^{10}Be/^{9}Be$ values along the SLPR-1 core (Fig. 18) despite the high variability of Sr data in the parallel HGB-3 core (Fig. 18 in Šujan et al, submitted) supports a stable input of Be isotopes even in the case of variable provenance, at least in the southern depocenter. Hence, the ages of the northern Turčiansky Peter, Martin – claypit and Turčianske Kľačany – Kúdel sites are further used as reliable, despite the chronostratigraphic model is much more robust in the southern sub-basin

5.2 Paleoenvironmental characteristics from inorganic proxies

The alluvial and braided river mud can be described as carbonate based on the classification by Herron (1988). The Blažovce delta consists of calcareous mud, and samples from open lake sites lie on the boundary between noncalcareous and calcareous mud to wacke (Herron, 1988). It documents the decrease in carbonate content from alluvial mud trough braided river and delta muds to open lake sediments, as the sediment pass through the source-to-sink system (Fig. 15). The loss of carbonate grains with an increase in transport length is also supported by XRD. The detritic origin of carbonate grains is indicated by the presence of dolomite together with calcite in their composition, and by the dominance of the silt fraction in grain size analyses (Table 3, Table 5 in Šujan et al., submitted). Moreover, the carbonate composition of gravel layers above and below these mud intercalations supports this assumption. It should be noted that samples from a single correlated level may well contain various proportions of carbonate (lateral variation: Blaz-3 and Blaz-5 yield 17 and 24 wt. % of CO_2, respectively) (Table 9 in Šujan et al., submitted), which further supports an assumption of the detritic origin of these carbonates.

On the other hand, in the case of open lake sediments, a change in provenance/source rocks needs to be considered, as it is implied by the higher Si/Al ratio in open lake mud, plus the fact that these samples are seen close to the shale/wacke boundary in a diagram on Fig. 15 according to Herron (1988). Despite the fact that open lake muds are more coarse-grained, they do contain a small proportion of carbonate grains, and this points to the presence of different, silicate source rocks during the deposition of open lake mud. This may, in turn, be explained by the spatial location of sites, in that the studied open lake outcrops are located in the northern depocenter of the Turiec Basin (Fig. 2A), while the latter are to be found in the elevated central sill dividing the two depressions, and difference in provenance is therefore likely. In the northern part of the basin, Paleozoic granitoids and gneiss, together with carbonates, and Paleogene turbiditic deposits build up the basin margin. The geochemical analysis also confirms that carbonate alluvial mud contains the lowest portion of Fe, and the content of Fe increases with the portion of silicate minerals which represent the primary source of Fe (Fig. 15).

The more detailed whole rock analyses of the Blažovce delta mud point to freshwater, oxic bottom water conditions via low values of sulfur content, TOC (total organic carbon), the C_{org}/P molar ratio and low values of the Mo and Ni enrichment factors (Berner, 1984; Raiswell and Berner, 1986; Jones and Manning, 1994; Algeo and Liu, 2020, and references therein; Wei and Algeo, 2020). The slightly increased U content (U_{ef} 1.1–1.7) can be explained by the presence of carbonates in the composition (Table 9 in Šujan et al., submitted). The CIA index (Nesbitt and Young, 1982), following the simplification found in McLennan (1993), reaches 82–86, and this range indicates a medium to high degree of chemical weathering in the source area and/or after mud accommodation (Fig. 15). Generally, the Si/Al ratio of the Blažovce samples documents increasing grain size as we proceed upwards, consistent with increasing carbonate clastic input due to the progradation of the deltaic system.

5.3 Evolution of the Turiec Basin

The obtained weighted mean ages indicate that the open lake environment of Lake Turiec persisted at least from 10.667 ± 0.518 Ma to 6.697 ± 0.135 Ma. The disappearance of the lake is evidenced by the progradation of the alluvial fan-braided river-fan delta depositional system and occurred at 6.697 ± 0.135 Ma, according to the age of the Blažovce site. The braided river environment existed parallel to the open lake (7.469 ± 0.231 Ma, Abramová - Kolísky) or later, in a similar period to the fan deltaic environment (6.432 ± 0.162 Ma, Socovce). The alluvial fan sites are coeval with or younger than the deltaic and braided river environment, reaching 6.394 ± 0.195 Ma (Valča), or the ages in the range of 7.03–4.64 Ma (Ondrašová) and 5.83–3.98

Ma (Slovany), which fit with the notion that the general stratigraphic position of the alluvial fan deposits represent the final part of the basin fill.

The ages generally confirm the earlier lithostratigraphic concept suggested by Kováč et al. (2011). Nevertheless, the integration of authigenic $^{10}Be/^{9}Be$ dating, sedimentology, geochemistry and basin analysis using lithological borehole logs implies the concurrent existence of alluvial fan-braided river-fan delta-open lake sedimentary environments as an interconnected source-to-sink system. This conception differs from the originally inferred spatio-temporal succession of these environments.

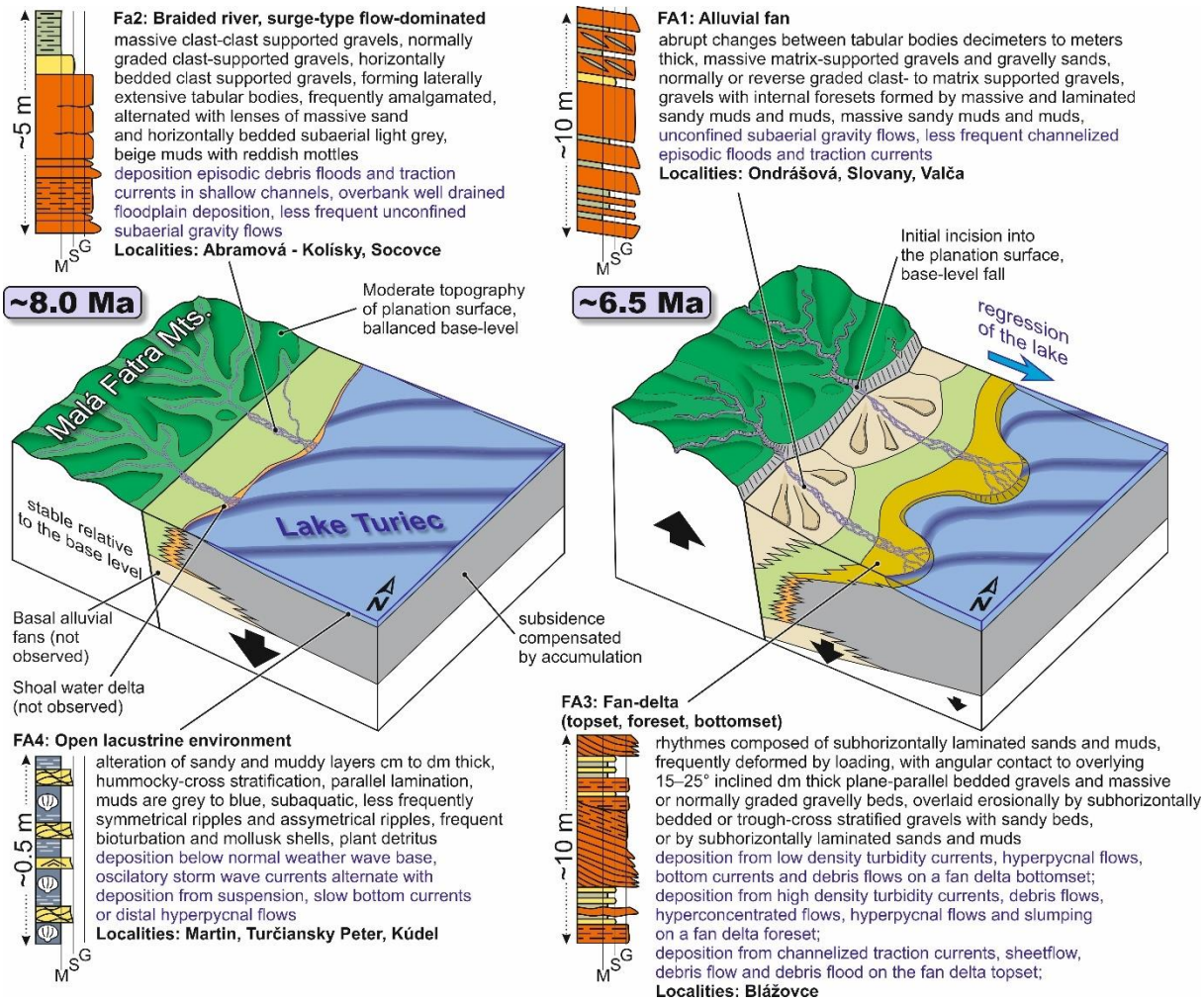

Fig. 21. Block diagrams showing the distribution of facies associations in the Turiec Basin concerning accommodation rate and sediment supply driven mainly by vertical motions. The period of balanced accommodation and sediment supply lasted during the existence of Lake Turiec (left), when endemic fauna evolved and the surrounding mountains formed only a moderate hilly landscape without intense incision. The changed tectonic regime led to an increased rate of uplift of the mountains on the western margin of the basin and a consequent increase in the ratio of sediment supply to accommodation rate, which caused the regression and disappearance of Lake Turiec and the extinction of the endemic fauna.

Despite the very restricted size of Lake Turiec (~10 × 40 km), its lacustrine environment persisted for at least ~4.0 Myr, and likely for an even longer period, since this study provides only ages of the surface exposures of the Martin Formation. These lacustrine deposits reach a thickness of up to 900 m, hence, the accommodation rate reached the order of ~200–250 m/Myr. Although subsidence was relatively high, the surrounding subaerially exposed blocks did not

yield enough sediment supply to cause regression of the lake during the period ~10.7–6.7 Ma. The lake was surrounded by a moderate topography at that time, as assumed from the paleoecological proxies, which indicate the existence of marshes, coastal wetlands, and humid forests, inconsistent with concurrent high sediment supply at the basin margin (Chapter 2.2). This then implies that the base level was balanced on the marginal blocks without significant incision and streams flowing to the Turiec Basin did not form large alluvial fans (Fig. 21). The floodplains of small rivers likely entered the lake as shoal-water deltas (García-García et al., 2006; Ghinassi, 2007), but these were not observed in the exposed depositional record.

The situation changed significantly at ~6.7 Ma (Blažovce site), or ~6.5 Ma (peak of the KDE distribution, Fig. 21), when sediment supply from the western margin of the basin (Malá Fatra Mts.) significantly increased relative to the accommodation rate. A system of alluvial fans started to feed the rivers, which entered the lake as sandy-gravelly fan deltas (Fig. 21). Turiec Lake was shallow from the sedimentological point of view, estimated to below 40 m in the northern sub-basin and in the range of 40–100 m in the southern sub-basin, hence, only delta-scale clinoforms prograded across its water body (Patruno and Helland-Hansen, 2018). The regression therefore appeared relatively abruptly, in <100 kyr, as a result of increased sediment supply (sensu Catuneanu, 2006), despite the delta progradation being affected by flooding events of a high order of cyclicity (Fig. 11). The disturbance of the previously stable sediment supply to accommodation ratio must have been caused by the uplift of the Malá Fatra Mts. and incision of rivers into the massif due to the relative base level fall, although a decrease in the subsidence rate might have played a role. The prevailing direction of the delta progradation towards the southwest at the Blažovce site corresponds generally with the orientation to the main depocenter of the southern Turiec Basin (Fig. 13 in Šujan et al., submitted). Nevertheless, the course of the fan delta lobe progradation is mainly moderated by autogenic processes (Van Dijk et al., 2009). The demand for a more spatially distributed dataset to underpin robustness of the paleotransport assumption is limited by absence of further exposures of the deltaic succession.

An alluvial fan environment likely covered most of the studied area in the period following the regression of Lake Turiec, as is indicated by the distribution of this facies association across the southern sub-basin (Fig. 14). However, subsequent basin inversion (Kováč et al., 2011) and erosion of the basin fill caused surface exposure of 6–10 Ma old successions, and the specific history of the basin just after the regression of Lake Turiec is a conundrum because of the missing depositional record, especially in the northern sub-basin.

5.4 Implications for geodynamic processes and paleogeography

The timing of the major change in the accommodation rate to sediment supply ratio in the Turiec Basin is similar to the timing of the inversion of the Pannonian Basin System (PBS), which happened time transgressively across the region at ~8–4 Ma (Fodor et al., 2005; Horváth et al., 2006; Bada et al., 2007; Ruszkiczay-Rüdiger et al., 2007; Uhrin et al., 2009) and around 6 Ma in its northwesternmost part, the Danube Basin (Šujan et al., 2021b). The basin inversion of the PBS was related to several processes, such as the push of the Adria lithospheric microplate, topography-induced gravitational stress, differential loading of syn-inversion sediments that caused the elastic flexure of a weakened lithosphere, as well as the general heterogeneous contraction of the rheologically layered lithosphere exposed to temporal thermomechanical changes after rifting (Burov and Cloetingh, 1997; Bada et al., 2001; Jarosinski et al., 2011; Ruszkiczay-Rüdiger et al., 2020; Tari et al., 2020). This resulted in lithospheric-scale folding associated with a major reduction in accommodation of the affected basins, their uplift, and the denudation of basin fill.

The coincidence in the timing of the PBS inversion with the termination of Lake Turiec's existence by a rapid increase of sediment supply from the uplifting mountains is likely linked to a common geodynamic cause. The regional change in the geodynamic regime would be expected to affect the local stress field and kinematics of the faults, which were driving the subsidence of the Turiec Basin (Kováč et al., 2011). It is a matter for future research to implement the new geochronological data obtained in this study to resolve changes in the of the basin formation regime.

The thermochronological data obtained from the Malá Fatra Mts. (Kráľ et al., 2007; Danišík et al., 2010; Králiková et al., 2014b) (Fig. 2) imply that a phase of intense exhumation appeared within the time constraints ~15–7 Ma. It was associated with the tectonic escape of the ALCAPA microplate towards the northeast and its collision with the European platform (Ratschbacher et al., 1991; Kováč et al., 2017b). This evolutionary stage likely preceded the period of relative tectonic quiescence documented by the low intensity of denudation of the morphostructures surrounding Lake Turiec, and formation of the so called "Mid-mountain level" planation surface (Mazúr, 1963; Minár et al., 2011).

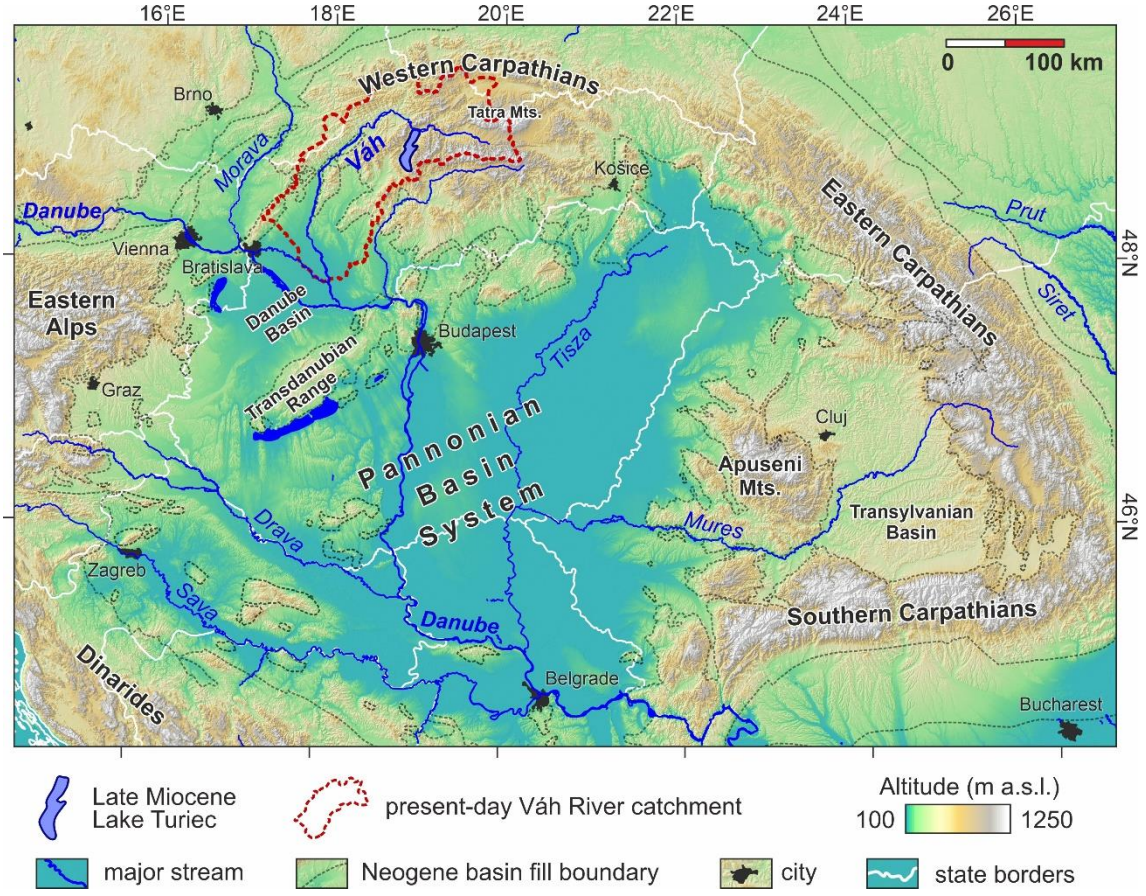

Fig. 22. Location of the present-day Váh River catchment within the Carpathian-Pannonian source-to-sink-system, which ultimately fills the Black Sea Basin at the Danube delta. Lake Turiec acted as a transient storage for the sediment denudated upstream during its endorheic period at ~10.0–6.7 Ma, and system connectivity was established only later. The upstream area includes the recently most topographically exposed mountains of the Western Carpathians, like the Tatra Mts.

Given the moderate humidity expected in the region during the Late Miocene (van Dam, 2006; Böhme et al., 2008; Kováčová et al., 2011; Utescher et al., 2017), the long-lived and only <40 m deep lake (northern sub-basin) might have persisted only in an endorheic basin, since outflowing streams would have broken topographic barriers and disrupted its landlocked

storage (Bridgland et al., 2020), especially in the conditions of low uplift rates and moderate relief surrounding the lake during the period of ~10.6–6.7 Ma (Sobel et al., 2003). Very similar settings of a mosaic of endorheic basins in humid climate with lack of paleo-relief in the region was described for the Miocene-Pliocene period of the Northeastern Sierra Nevada, USA (Trexler et al., 2012).

The drainage of the Váh river in its present extent, draining a significant part of the Western Carpathians, and flowing through the Turiec Basin (Fig. 22), might have been formed only after ~6.7 Ma, because its sediment supply would cause a rapid regression of Lake Turiec. However, a stream providing major coarse-sediment supply with the characteristics of a distant provenance appeared in the northern Danube Basin at ~9 Ma, forming the fluvial fan of the Piešťany Member (Šujan et al., 2017). Despite the fact that it was considered an equivalent of the present Váh river, the extent of this stream paleo-drainage network was restricted by Lake Turiec and remains to be fully uncovered.

The most exposed morphostructures of the Western Carpathians, like the Tatra Mts., are presently located upstream of the Turiec Basin, and sediment delivery within the source-to-sink system towards the Pannonian Basin might have been established only after the regression and disappearance of Lake Turiec (Fig. 22). This implies a limited sediment supply from these parts of the orogenic belt during the period ~10.0–6.7 Ma. The thermochronological estimate of accelerated uplift of the Tatra Mts. after ~7 Ma (Králiková et al., 2014c) is in agreement with the inferred low input of sediment towards Lake Turiec from this area.

The endorheic Turiec Basin formed a transient storage for sediment eroded from surrounding mountains. The establishment of drainage network connectivity by the overfilling of the basin after the lake regression likely led to an incision, and to a decrease in accommodation rates (Schildgen et al., 2016; Geurts et al., 2018). Loading by the ~1000 m thick Upper Miocene succession related to the existence of Lake Turiec would be expected to have enhanced the accommodation rates, and the termination of the endorheic period further amplified incision by unloading the area of the basin (Ballato et al., 2019). These processes correspond to the stratigraphic architecture of the Turiec Basin, since the post-Late Miocene incision led to the surficial exposure of sediments up to ~10 Ma old (Fig. 3). Future dating of the Pliocene-Quaternary successions overlying the Lake Turiec tectonic sequence (*sensu* Matenco and Haq, 2020), e.g., the Diviaky Member (Fig. 3) may help to resolve whether younger periods of endorheic basin character did indeed appear, and will reveal a younger history of base-level variations.

6. Conclusions

This study provides a complex analysis of the Upper Miocene tectonic sequence (*sensu* Matenco and Haq, 2019) in the Turiec Basin, Western Carpathians (Central Europe), in order to reveal the timing and mode of regression of the long-lived Lake Turiec in this intermontane basin. The sedimentological analysis of nine outcrops served to identify alluvial fan, braided river, fan delta and open lake facies associations, which were correlated across the basin using borehole profiles. Authigenic $^{10}Be/^{9}Be$ dating implies that a period of relatively rapid subsidence and low sediment supply from surrounding morphostructures to Lake Turiec occurred between ~10.7–6.7 Ma. The lake persisted until it was filled by a significant increase in sediment supply to accommodation rate ratio at ~6.7 Ma, when extensive alluvial fans associated with fan deltas appeared. The newly formed depositional systems were fed by the uplifted Malá Fatra Mts. from the west. The lake regression after ~6.7 Ma led to the termination of the endorheic period of the Turiec Basin, allowing the establishment of drainage network

connectivity within the Western Carpathians and the formation of the present-day Váh river drainage, which delivers sediment from the most topographically exposed mountains of the orogenic belt towards the Pannonian Basin and the Danube watershed. Hence, the established model of the Turiec Basin evolution significantly contributes to the overall understanding of the temporal evolution of the Carpathian-Pannonian-Black Sea source-to-sink system (Matenco et al., 2016).

The analysis of Late Pleistocene to Holocene alluvial strata uncovered a one order of magnitude variation in initial authigenic $^{10}Be/^{9}Be$ ratios, and this is relevant to the applicability of this dating method. Sedimentological, geochemical and mineralogical proxies indicate that the analyzed sites differ in accommodation rates, in the pace of burial of the sampled strata, and in the connectivity to groundwater. These differences affect the intensity of ^{10}Be input from meteoric waters before a bed is buried and the preserved authigenic $^{10}Be/^{9}Be$ ratio is attained. Therefore, the alluvial fan site with highest rate of sediment supply and strata burial, and lowest degree of connectivity to groundwater level was selected as representative for the purposes of age calculations of the Upper Miocene alluvial fan, braided river and fan delta deposits, since its depositional conditions were similar to those sites. The initial ratio for dating of the lacustrine sites was back-calculated using analysis of magnetostratigraphically dated well-core (Márton et al., 2022), and the obtained value is comparable to the one selected for the terrestrial facies associations. Interestingly, the analysis of $^{10}Be/^{9}Be$ variability in the Pleistocene to Holocene alluvial strata indicates that post-depositional alteration and the pace of burial is much more important control on the resulting value relative to changes in sediment provenance.

The study implies that fills of intermontane basins with relatively high accommodation rates might serve as targets suitable for the application of authigenic $^{10}Be/^{9}Be$ dating. The favorable factors in these settings are the low probability of post-depositional alteration of the authigenic $^{10}Be/^{9}Be$ record and the limited recycling of the basin fill by redeposition of mud with an older $^{10}Be/^{9}Be$ signature, similar to that observed in the back-arc settings of the Danube Basin (Šujan et al., 2020; Šujan et al., 2023). The understanding of depositional history of a basin is essential for proper application of the method and for careful determination of initial authigenic $^{10}Be/^{9}Be$ ratio.

Acknowledgement

The study was supported by the Slovak Research and Development Agency (APVV) under contracts Nos. APVV-16-0121, APVV-20-0120 and APVV-21-0281, and by the Scientific Grant Agency of the Ministry of Education, Science, Research and Sport of the Slovak Republic and the Slovak Academy of Sciences (VEGA) under the contract No. 1/0346/20. The free availability of the Lidar DEM data owned by the Geodesy, Cartography and Cadaster Authority of the Slovak Republic (ÚGKK SR) and distributed by the Geodetic and Cartographic Institute, Bratislava (GKÚ) is acknowledged with gratitude. The ASTER AMS national facility (CEREGE, Aix-en-Provence, France) is supported by the INSU/CNRS, the ANR through the "Projets thématiques d'excellence" program for the "Equipements d'excellence" ASTER-CEREGE action, and IRD. Paul Thatcher is thanked for his efforts made during the language correction. The reviewers Joseph Graly and Arjan de Leeuw are thanked for their precise insights and detailed comments, which significantly contributed to the final version of the paper.

References

Algeo, T.J. and Liu, J., 2020. A re-assessment of elemental proxies for paleoredox analysis. Chemical Geology, 540, 119549.

Allen, J.R.L., 1982. Sedimentary Structures: Their Character and Physical Basis. Elsevier, Amsterdam, 593 pp.

Amoudry, L.O., Bell, P.S., Thorne, P.D. and Souza, A.J., 2013. Toward representing wave-induced sediment suspension over sand ripples in RANS models. Journal of Geophysical Research: Oceans, 118(5), 2378-2392.

Aslan, A. and Autin, W.J., 1999. Evolution of the Holocene Mississippi River floodplain, Ferriday, Louisiana: Insights on the origin of fine-grained floodplains. Journal of Sedimentary Research, 69(4), 800-815.

Baas, J.H., Best, J.L. and Peakall, J., 2016. Predicting bedforms and primary current stratification in cohesive mixtures of mud and sand. Journal of the Geological Society, 173(1), 12-45.

Bacon, A.R., Richter, D.d., Bierman, P.R. and Rood, D.H., 2012. Coupling meteoric ^{10}Be with pedogenic losses of ^{9}Be to improve soil residence time estimates on an ancient North American interfluve. Geology, 40(9), 847-850.

Bada, G., Horváth, F., Cloetingh, S., Coblentz, D.D. and Tóth, T., 2001. Role of topography-induced gravitational stresses in basin inversion: The case study of Pannonian basin. Tectonics, 20(3), 343-363.

Bada, G., Horváth, F., Dövényi, P., Szafián, P., Windhoffer, G. and Cloetingh, S., 2007. Present-day stress field and tectonic inversion in the Pannonian basin. Global and Planetary Change, 58(1–4), 165-180.

Ballato, P., Brune, S. and Strecker, M.R., 2019. Sedimentary loading–unloading cycles and faulting in intermontane basins: Insights from numerical modeling and field observations in the NW Argentine Andes. Earth and Planetary Science Letters, 506, 388-396.

Barg, E., Lal, D., Pavich, M.J., Caffee, M.W., Southon, J.R., 1997. Beryllium geochemistry in soils: evaluation of ^{10}Be/^{9}Be ratios in authigenic minerals as a basis for age models. Chemical Geology, 140, 237-258.

Benvenuti, M., 2003. Facies analysis and tectonic significance of lacustrine fan-deltaic successions in the Pliocene-Pleistocene Mugello Basin, Central Italy. Sedimentary Geology, 157(3-4), 197-234.

Berner, R.A., 1984. Sedimentary pyrite formation: An update. Geochimica et Cosmochimica Acta, 48, 605-615.

Bielik, M., Krajňák, M., Makarenko, I., Legostaeva, O., Starostenko, V.I., Bošanský, M., Grinč, M. and Hók, J., 2013. 3D gravity interpretation of the pre-Tertiary basement in the intramontane depressions of the Western Carpathians: A case study from the Turiec Basin. Geologica Carpathica, 64(5), 399-408.

Blikra, L.H. and Nemec, W., 1998. Postglacial colluvium in western Norway: depositional processes, facies and palaeoclimatic record. Sedimentology, 45(5), 909-959.

Böhme, M., Ilg, A. and Winklhofer, M., 2008. Late Miocene "washhouse" climate in Europe. Earth and Planetary Science Letters, 275(3–4), 393-401.

Boothroyd, J.C. and Ashley, G.M., 1975. Processes, Bar Morphology, and Sedimentary Structures on Braided Outwash Fans, Northeastern Gulf of Alaska. In: A.V. Jopling and B.C. McDonald (Eds.), Glaciofluvial and Glaciolacustrine Sedimentation. SEPM Society for Sedimentary Geology, pp. 193-222.

Boulesteix, K., Poyatos-Moré, M., Flint, S.S., Taylor, K.G., Hodgson, D.M. and Hasiotis, S.T., 2019. Transport and deposition of mud in deep-water environments: Processes and stratigraphic implications. Sedimentology, 66(7), 2894-2925.

Bourlès, D., Raisbeck, G. and Yiou, F., 1989. ^{10}Be and ^{9}Be in marine sediments and their potential for dating. Geochimica et Cosmochimica Acta, 53(2), 443-452.

Braucher, R., Guillou, V., Bourlès, D.L., Arnold, M., Aumaître, G., Keddadouche, K. and Nottoli, E., 2015. Preparation of ASTER in-house ^{10}Be/^{9}Be standard solutions. Nuclear Instruments and Methods in Physics Research Section B: Beam Interactions with Materials and Atoms, 361, 335-340.

Brenna, A., Surian, N., Ghinassi, M. and Marchi, L., 2020. Sediment–water flows in mountain streams: Recognition and classification based on field evidence. Geomorphology, 371, 107413.

Bridgland, D.R., Westaway, R. and Hu, Z., 2020. Basin inversion: A worldwide Late Cenozoic phenomenon. Global and Planetary Change, 193, 103260.

Brown, E.T., Measures, C.I., Edmond, J.M., Bourlès, D.L., Raisbeck, G.M. and Yiou, F., 1992. Continental inputs of beryllium to the oceans. Earth and planetary science letters, 114(1), 101-111.

Brumsack, H.J., 1989. Geochemistry of recent TOC-rich sediments from the Gulf of California and the Black Sea. Geologische Rundschau, 78, 851- 882.

Budai, S., Colombera, L. and Mountney, N.P., 2021. Quantitative characterization of the sedimentary architecture of Gilbert-type deltas. Sedimentary Geology, 426, 106022.

Buday, T., 1962. Neogene of the Turiec Basin. Sborník Ústředního Ústavu Geologického – Geológia, 27, 475-502 (in Slovak).

Burbank, D.W., 1983. The chronology of intermontane-basin development in the northwestern Himalaya and the evolution of the Northwest Syntaxis. Earth and Planetary Science Letters, 64(1), 77-92.

Burov, E. and Cloetingh, S., 1997. Erosion and rift dynamics: new thermomechanical aspects of post-rift evolution of extensional basins. Earth and Planetary Science Letters, 150(1–2), 7-26.

Carcaillet, J., Bourlès, D.L., Thouveny, N. and Arnold, M., 2004. A high resolution authigenic $^{10}Be/^{9}Be$ record of geomagnetic moment variations over the last 300 ka from sedimentary cores of the Portuguese margin. Earth and Planetary Science Letters, 219(3–4), 397-412.

Cartigny, M.J.B., Ventra, D., Postma, G. and van Den Berg, J.H., 2014. Morphodynamics and sedimentary structures of bedforms under supercritical-flow conditions: New insights from flume experiments. Sedimentology, 61(3), 712-748.

Catuneanu, O., 2006. Principles of Sequence Stratigraphy. Elsevier, Amsterdam, 375 pp.

Danišík, M., Kohút, M., Broska, I. and Frisch, W., 2010. Thermal evolution of the Malá Fatra Mountains (Central Western Carpathians): Insights from zircon and apatite fission track thermochronology. Geologica Carpathica, 61(1), 19-27.

International Centre for Diffraction Data, 2022. PDF-4/Minerals, SN: MIND 220124-5612, https://www.icdd.com/pdf-4-minerals/.

Deng, K., Wittmann, H., von Blanckenburg, F., 2020. The depositional flux of meteoric cosmogenic ^{10}Be from modeling and observation. Earth and Planetary Science Letters, 550, 116530.

Dixon, J.L., Chadwick, O.A. and Pavich, M.J., 2018. Climatically controlled delivery and retention of meteoric ^{10}Be in soils. Geology, 46(10), 899-902.

Dumas, S. and Arnott, R.W.C., 2006. Origin of hummocky and swaley cross-stratification - The controlling influence of unidirectional current strength and aggradation rate. Geology, 34(12), 1073-1076.

Dumas, S., Arnott, R.W.C. and Southard, J.B., 2005. Experiments on oscillatory-flow and combined-flow bed forms: Implications for interpreting parts of the shallow-marine sedimentary record. Journal of Sedimentary Research, 75(3), 501-513.

Fendek, M., Gašparik, J., Gross, P., Janči, J., Kohút, M., Kráľ, J., Kullmanová, A., Planderová, E., Raková, J., Rakús, M., Snopková, P., Tuba, Ľ., Vass, D. and Vozárová, A., 1990. Technical report on geothermal borehole ZGT-3 Turiec in Martin and prognostic resources of geothermal energy in the area of Martin. Manuscript, Geofond Nr.: 75501, 86 pp. available online: https://da.geology.sk/navigator/?desktop=Public.

Fielding, C.R., 2006. Upper flow regime sheets, lenses and scour fills: Extending the range of architectural elements for fluvial sediment bodies. Sedimentary Geology, 190(1-4), 227-240.

Fielding, C.R., Alexander, J. and Allen, J.P., 2018. The role of discharge variability in the formation and preservation of alluvial sediment bodies. Sedimentary Geology, 365, 1-20.

Fodor, L., Bada, G., Csillag, G., Horváth, E., Ruszkiczay-Rüdiger, Z., Palotás, K., Síkhegyi, F., Timár, G., Cloetingh, S. and Horváth, F., 2005. An outline of neotectonic structures and morphotectonics of the western and central Pannonian Basin. Tectonophysics, 410(1–4), 15-41.

Folk, R.L. and Ward, W.C., 1957. A Study in the Significance of Grain-Size Parameters. Journal of Sedimentary Petrology, 27, 3-26.

Freitas, M.M.D., Paixão, R.W., Salgado, A.A.R., Eirado Silva, L.G., Cunha, P.P., Gomes, A.A.T., Martins, A.A., Almeida, J.C.H., Tupinambá, M.A., Dantas, M., 2022. The endorheic – Exorheic transition and later stage of fluvial incision in a wet tropical margin setting: The Atlantic draining Paraíba do Sul River basin (Brazil). Journal of South American Earth Sciences 115, 103742.

Froitzheim, N., Plašienka, D. and Schuster, R., 2008. Alpine tectonics of the Alps and Western Carpathians. In: T. McCann (Ed.), The Geology of Central Europe Volume 2: Mesozoic and Cenozoic. Geological Society of London, pp. 1141-1232.

Garcia-Castellanos, D., 2006. Long-term evolution of tectonic lakes: Climatic controls on the development of internally drained basins. In: Willett, S.D., Hovius, N., Brandon, M,T., Fisher, D.M. (Eds.). Tectonics, Climate, and Landscape Evolution. Geological Society of America, pp. 283-294.

García-García, F., Fernández, J., Viseras, C. and Soria, J.M., 2006. Architecture and sedimentary facies evolution in a delta stack controlled by fault growth (Betic Cordillera, southern Spain, late Tortonian). Sedimentary Geology, 185(1-2), 79-92.

Gašparik, J., 1972. Záverečná správa o vyhodnotení štruktúrneho vrtu GHŠ-1 Horná Štubňa. Manuscript, Geofond Nr: 31218, 57 pp. Available online: https://da.geology.sk/navigator/?desktop=Public.

Gašparík, J. and Halouzka, R., 1993. Explanatory notes to the geological map of the Turiec Basin, scale 1 : 50 000. State Geological Institute of Dionýz Štúr, Bratislava, 196 pp.

Geological map of Slovakia, 2013. Geological map of Slovakia at a scale of M 1:50 000 [online]. State Geological Institute of Dionýz Štúr, Bratislava. Available online: http://mapservergeology.sk/gm50js

Geurts, A.H., Cowie, P.A., Duclaux, G., Gawthorpe, R.L., Huismans, R.S., Pedersen, V.K. and Wedmore, L.N.J., 2018. Drainage integration and sediment dispersal in active continental rifts: A numerical modelling study of the central Italian Apennines. Basin Research, 30(5), 965-989.

Ghinassi, M., 2007. The effects of differential subsidence and coastal topography on high-order transgressive-regressive cycles: Pliocene nearshore deposits of the Val d'Orcia Basin, Northern Apennines, Italy. Sedimentary Geology, 202(4), 677-701.

Gibling, M.R., Ukakimaphan, Y. and Srisuk, S., 1985. Oil shale and coal in intermontane basins of Thailand. American Association of Petroleum Geologists Bulletin, 69(5), 760-766.

Gobo, K., Ghinassi, M. and Nemec, W., 2015. Gilbert-type deltas recording short-term base-level changes: Delta-brink morphodynamics and related foreset facies. Sedimentology.

Graham, I., Ditchburn, R. and Whitehead, N., 2001. Be isotope analysis of a 0–500 ka loess–paleosol sequence from Rangitatau East, New Zealand. Quaternary International, 76, 29-42.

Graly, J.A., Bierman, P.R., Reusser, L.J. and Pavich, M.J., 2010. Meteoric ^{10}Be in soil profiles – A global meta-analysis. Geochimica et Cosmochimica Acta, 74(23), 6814-6829.

Hajek, E.A. and Straub, K.M., 2017. Autogenic Sedimentation in Clastic Stratigraphy. Annual Review of Earth and Planetary Sciences, 45(1), 681-709.

Harzhauser, M. and Mandic, O., 2008. Neogene lake systems of Central and South-Eastern Europe: Faunal diversity, gradients and interrelations. Palaeogeography, Palaeoclimatology, Palaeoecology, 260(3–4), 417-434.

Havrila, M., 2011. Hronikum: paleogeografia a stratigrafia (vrchný pelsón – tuval), štrukturalizácia a stavba. Geologické práce, Správy, 117, 7-103 (in Slovak).

Henken-Mellies, W., Beer, J., Heller, F., Hsü, K., Shen, C., Bonani, G., Hofmann, H., Suter, M. and Wölfli, W., 1990. ^{10}Be and ^{9}Be in South Atlantic DSDP Site 519: Relation to geomagnetic reversals and to sediment composition. Earth and Planetary Science Letters, 98(3-4), 267-276.

Herron, M.M., 1988. Geochemical classification of terrigenous sands and shales from core or log data. Journal of Sedimentary Petrology, 58, 820-829.

Hók, J., Šujan, M. and Šipka, F., 2014. Tectonic division of the Western Carpathians: An overview and a new approach. Acta Geologica Slovaca, 6(2), 135-143.

Holec, J. and Braucher, R., 2014. Cosmogenic chlorine dating of alluvial fan (Veľký Čepčín, Turčianska kotlina basin). In: J. Novotný (Ed.), Geomorfológia a environmentálne výzvy. Zborník abstraktov Bratislava, SAV, 2014, pp. 20.

Horváth, F., Bada, G., Szafián, P., Tari, G., Ádám, A. and Cloetingh, S., 2006. Formation and deformation of the Pannonian Basin: Constraints from observational data, Geological Society Memoir, pp. 191-206.

Chaimov, T.A., Barazangi, M., Al-Saad, D., Sawaf, T. and Gebran, A., 1992. Mesozoic and Cenozoic deformation inferred from seismic stratigraphy in the southwestern intracontinental Palmyride fold-thrust belt, Syria. Geological Society of America Bulletin, 104(6), 704-715.

Chernyshev, I.V., Konečný, V., Lexa, J., Kovalenker, V.A., Jeleň, S., Lebedev, V.A. and Goltsman, Y.V., 2013. K-Ar and Rb-Sr geochronology and evolution of the Štiavnica Stratovolcano (Central Slovakia). Geologica Carpathica, 64(4), 327-351.

Church, M. and Jakob, M., 2020. What Is a Debris Flood? Water Resources Research, 56(8), e2020WR027144.

Inoue, T., Huang, Z.-Y., Imamura, M., Tanaka, S. and Usui, A., 1983. ^{10}Be and ^{10}Be/^{9}Be in manganese nodules. Geochemical Journal, 17(6), 307-312.

Jarosinski, M., Beekman, F., Matenco, L. and Cloetingh, S., 2011. Mechanics of basin inversion: Finite element modelling of the Pannonian Basin System. Tectonophysics, 502(1–2), 121-145.

Jelby, M.E., Grundvåg, S.A., Helland-Hansen, W., Olaussen, S. and Stemmerik, L., 2020. Tempestite facies variability and storm-depositional processes across a wide ramp: Towards a polygenetic model for hummocky cross-stratification. Sedimentology, 67(2), 742-781.

Jones, B. and Manning, D.A.C., 1994. Comparison of geochemical indices used for the interpretation of palaeoredox conditions in ancient mudstones. Chemical Geology, 111(1), 111-129.

Joniak, P., Šujan, M., Fordinál, K., Braucher, R., Rybár, S., Kováčová, M., Kováč, M., Aumaître, G., Bourlès, D.L. and Keddadouche, K., 2020. The age and paleoenvironment of a late Miocene floodplain alongside Lake Pannon: Rodent and mollusk biostratigraphy coupled with authigenic ^{10}Be/^{9}Be dating in the northern Danube Basin of Slovakia. Palaeogeography, Palaeoclimatology, Palaeoecology, 538.

Kilényi, E. and Šefara, J., 1991. Pre-Tertiary basement contour map of the Carpathian Basin Beneath Austria, Czechoslovakia and Hungary. Geophysical Transactions, 36(1-2), 15-36.

Konečný, V., Kováč, M., Lexa, J. and Šefara, J., 2002. Neogene evolution of the Carpatho-Pannonian region: an interplay of subduction and back-arc diapiric uprise in the mantle. EGS Stephan Mueller Special Publication, 1, 105-123.

Konečný, V., Lexa, J. and Hojstričová, V., 1995. The Central Slovakia Neogene volcanic field: a review. Acta Volcanologica, 7, 63-78.

Konečný, V., Lexa, J. and Planderová, E., 1983. Stratigraphy of the Central Slovakia volcanic field. Západné Karpaty, Séria Geológia, 9, 1-203 (in Slovak with English summary).

Kong, W., Zhou, L. and AsterTeam, 2021. Tracing Water Masses and Assessing Boundary Scavenging Intensity With Beryllium Isotopes in the Northern South China Sea. Journal of Geophysical Research: Oceans, 126(7), e2021JC017236.

Kováč, M., Halásová, E., Hudáčková, N., Holcová, K., Hyžný, M., Jamrich, M. and Ruman, A., 2018. Towards better correlation of the Central Paratethys regional time scale with the standard geological time scale of the Miocene Epoch. Geologica Carpathica, 69(3), 283-300.

Kováč, M., Hók, J., Minár, J., Vojtko, R., Bielik, M., Pipík, R., Rakús, M., Kráå, J., Åujan, M. and Králiková, S., 2011. Neogene and Quaternary development of the Turiec Basin and landscape in its catchment: A tentative mass balance model. Geologica Carpathica, 62(4), 361-379.

Kováč, M., Hudáčková, N., Halásová, E., Kováčová, M., Holcová, K., Oszczypko-Clowes, M., Báldi, K., Less, G., Nagymarosy, A., Ruman, A., Klučiar, T. and Jamrich, M., 2017a. The Central Paratethys palaeoceanography: A water circulation model based on microfossil proxies, climate, and changes of depositional environment. Acta Geologica Slovaca, 9(2), 75-114.

Kováč, M., Márton, E., Oszczypko, N., Vojtko, R., Hók, J., Králiková, S., Plašienka, D., Klučiar, T., Hudáčková, N. and Oszczypko-Clowes, M., 2017b. Neogene palaeogeography and basin evolution of the Western Carpathians, Northern Pannonian domain and adjoining areas. Global and Planetary Change, 155, 133-154.

Kováč, M., Plašienka, D., Soták, J., Vojtko, R., Oszczypko, N., Less, G., Ćosović, V., Fügenschuh, B. and Králiková, S., 2016. Paleogene palaeogeography and basin evolution of the Western Carpathians, Northern Pannonian domain and adjoining areas. Global and Planetary Change, 140, 9-27.

Kováč, P. and Hók, J., 1993. The Central Slovak Fault System - the field evidence of a strike slip. Geologica Carpathica, 44(3), 155-159.

Kováčová, M., Doláková, N. and Kováč, M., 2011. Miocene vegetation pattern and climate change in the northwestern Central Paratethys domain (Czech and Slovak Republic). Geologica Carpathica, 62(3), 251-256.

Kráľ, J., Hók, J., Kotulová, J. and Rakús, M., 2007. Apatite fission-track data interpretation from the Lúčanská Fatra Mts. (Western Carpathians). Mineralia Slovaca, Geovestník, 39(4), 5-6.

Králiková, S., Vojtko, R., Andriessen, P., Kováč, M., Fuegenschuh, B., Hók, J. and Minár, J., 2014a. Late Cretaceous-Cenozoic thermal evolution of the northern part of the Central Western Carpathians (Slovakia): revealed by zircon and apatite fission track thermochronology. Tectonophysics, 615, 142-153.

Králiková, S., Vojtko, R., Andriessen, P., Kováč, M., Fügenschuh, B., Hók, J. and Minár, J., 2014b. Late Cretaceous-Cenozoic thermal evolution of the northern part of the Central Western Carpathians (Slovakia): Revealed by zircon and apatite fission track thermochronology. Tectonophysics, 615-616, 142-153.

Králiková, S., Vojtko, R., Sliva, L., Minár, J., Fuegenschuh, B., Kováč, M. and Hók, J., 2014c. Cretaceous-Quaternary tectonic evolution of the Tatra Mts (Western Carpathians): constraints from structural, sedimentary, geomorphological, and fission track data. Geologica Carpathica, 65(4), 307-326.

Krishnaswami, S., Mangini, A., Thomas, J., Sharma, P., Cochran, J., Turekian, K. and Parker, P., 1982. ^{10}Be and Th isotopes in manganese nodules and adjacent sediments: nodule growth histories and nuclide behavior. Earth and Planetary Science Letters, 59(2), 217-234.

Krumm, S., 1994. Centrifuge, Erlangen. http://www.ccp14.ac.uk/ccp/web-mirrors/krumm/html/software/winsoft.html.

Ku, T., Kusakabe, M., Measures, C., Southon, J., Cusimano, G., Vogel, J., Nelson, D. and Nakaya, S., 1990. Beryllium isotope distribution in the western North Atlantic: a comparison to the Pacific. Deep Sea Research Part A. Oceanographic Research Papers, 37(5), 795-808.

Ku, T., Kusakabe, M., Nelson, D., Southern, J., Korteling, R., Vogel, J. and Nowikow, I., 1982. Constancy of oceanic deposition of ^{10}Be as recorded in manganese crusts. Nature, 299(5880), 240-242.

Kusakabe, M., Ku, T., Southon, J., Liu, S., Vogel, J., Nelson, D., Nakaya, S. and Cusimano, G., 1991. Be isotopes in rivers/estuaries and their oceanic budgets. Earth and Planetary Science Letters, 102(3-4), 265-276.

Kusakabe, M., Ku, T., Southon, J., Vogel, J., Nelson, D., Measures, C. and Nozaki, Y., 1987. Distribution of ^{10}Be and ^{9}Be in the Pacific Ocean. Earth and Planetary Science Letters, 82(3-4), 231-240.

Lachner, J., Christl, M., Synal, H.-A., Frank, M. and Jakobsson, M., 2013. Carrier free ^{10}Be/^{9}Be measurements with low-energy AMS: Determination of sedimentation rates in the Arctic Ocean. Nuclear Instruments and Methods in Physics Research Section B: Beam Interactions with Materials and Atoms, 294, 67-71.

Langereis, G., Krijgsman, W., Muttoni, G. and Menning, M., 2010. Magnetostratigraphy-concepts, definitions, and applications. Newsletters on Stratigraphy, 43(3), 207-233.

Lebatard, A.-E., Bourlès, D.L., Braucher, R., Arnold, M., Duringer, P., Jolivet, M., Moussa, A., Deschamps, P., Roquin, C. and Carcaillet, J., 2010. Application of the authigenic ^{10}Be/^{9}Be dating method to continental sediments: reconstruction of the Mio-Pleistocene sedimentary sequence in the early hominid fossiliferous areas of the northern Chad Basin. Earth and Planetary Science Letters, 297(1-2), 57-70.

Lebatard, A.-E., Bourlès, D.L., Duringer, P., Jolivet, M., Braucher, R., Carcaillet, J., Schuster, M., Arnaud, N., Monié, P. and Lihoreau, F., 2008. Cosmogenic nuclide dating of Sahelanthropus tchadensis and Australopithecus bahrelghazali: Mio-Pliocene hominids from Chad. Proceedings of the National Academy of Sciences, 105(9), 3226-3231.

Leclair, S.F. and Bridge, J.S., 2001. Quantitative interpretation of sedimentary structures formed by river dunes. Journal of Sedimentary Research, 71(5), 713-716.

Lexa, J., Halouzka, R., Havrila, M., Hanzel, V., Kubeš, P., Liščák, P. and Hojstričová, V., 1998. Explanatory notes to the geological map of the Kremnické Vrchy Hills, scale 1 : 50 000. State Geological Institute of Dionýz Štúr, Bratiaslava, 308 pp.

Longhitano, S.G., 2008. Sedimentary facies and sequence stratigraphy of coarse-grained Gilbert-type deltas within the Pliocene thrust-top Potenza Basin (Southern Apennines, Italy). Sedimentary Geology, 210(3–4), 87-110.

Lowe, D.R., 1976. Grain flow and grain flow deposits. Journal of Sedimentary Research, 46, 188-199.

Lukniš, M., 1962. Die Reliefentwicklung der Westkarpaten. Wissenschaftliche Zeitschrift der Martin–Luther–Universit¨at Halle–Wittenberg. Mathematik–Naturwissenschaften, 11, 1235-1244.

Magyar, I., 2021. Chronostratigraphy of clinothem-filled non-marine basins: Dating the Pannonian Stage. Global and Planetary Change, 205, 103609.

Magyar, I., Radivojevic, D., Sztano, O., Synak, R., Ujszaszi, K. and Pocsik, M., 2013. Progradation of the paleo-Danube shelf margin across the Pannonian Basin during the Late Miocene and Early Pliocene. Global and Planetary Change, 103, 168-173.

Magyar, I., Sztanó, O., Sebe, K., Katona, L., Csoma, V., Görög, Á., Tóth, E., Szuromi-Korecz, A., Šujan, M., Braucher, R., Ruszkiczay-Rüdiger, Z., Koroknai, B., Wórum, G., Sant, K., Kelder, N. and Krijgsman,

W., 2019. Towards a high-resolution chronostratigraphy and geochronology for the Pannonian stage: Significance of the Paks cores (central Pannonian basin). Foldtani Kozlony, 149(3-4), 351-370.

Manville, V. and White, J.D.L., 2003. Incipient granular mass flows at the base of sediment-laden floods, and the roles of flow competence and flow capacity in the deposition of stratified bouldery sands. Sedimentary Geology, 155(1), 157-173.

Martini, I., Ambrosetti, E. and Sandrelli, F., 2017. The role of sediment supply in large-scale stratigraphic architecture of ancient Gilbert-type deltas (Pliocene Siena-Radicofani Basin, Italy). Sedimentary Geology, 350, 23-41.

Márton, E., Pipík, R., Starek, D., Kovács, E., Vidhya, M., Świerczewska, A., Tokarski, A.K., Vojtko, R. and Schlögl, S., 2022. Enhancing the reliability of the magnetostratigraphic age assignment of azimuthally nonoriented drill cores by the integrated application of palaeomagnetic analysis, field tests, anisotropy of magnetic susceptibility, and the evolution of the endemic fauna as documented on the upper Miocene limnic deposits of the Turiec Basin (Western Carpathians). AAPG Bulletin, 106(4), 803-827.

Matenco, L., Munteanu, I., ter Borgh, M., Stanica, A., Tilita, M., Lericolais, G., Dinu, C. and Oaie, G., 2016. The interplay between tectonics, sediment dynamics and gateways evolution in the Danube system from the Pannonian Basin to the western Black Sea. Science of The Total Environment, 543, 807-827.

Matenco, L.C. and Haq, B.U., 2020. Multi-scale depositional successions in tectonic settings. Earth-Science Reviews, 200, 102991.

Mazúr, E., 1963. Žilinská Kotlina Basin and Adjacent Mountains. Vydavateľstvo SAV, Bratislava.

McConnico, T.S. and Bassett, K.N., 2007. Gravelly Gilbert-type fan delta on the Conway Coast, New Zealand: Foreset depositional processes and clast imbrications. Sedimentary Geology, 198(3), 147-166.

McLennan, S.M., 1993. Weathering and global denudation. Journal of Geology, 101(2), 295-303.

McLennan, S.M., 2001. Relationships between the trace element composition of sedimentary rocks and upper continental crust. Geochemistry, Geophysics, Geosystems, 2(4).

Measures, C. and Edmond, J., 1982. Beryllium in the water column of the central North Pacific. Nature, 297(5861), 51-53.

Measures, C. and Edmond, J., 1983. The geochemical cycle of ^{9}Be: A reconnaissance. Earth and Planetary Science Letters, 66, 101-110.

Measures, C., Ku, T., Luo, S., Southon, J., Xu, X. and Kusakabe, M., 1996. The distribution of ^{10}Be and ^{9}Be in the South Atlantic. Deep Sea Research Part I: Oceanographic Research Papers, 43(7), 987-1009.

Merchel, S., Beutner, S., Opel, T., Rugel, G., Scharf, A., Tiessen, C., Weiß, S. and Wetterich, S., 2019. Attempts to understand potential deficiencies in chemical procedures for AMS. Nuclear Instruments and Methods in Physics Research Section B: Beam Interactions with Materials and Atoms, 456, 186-192.

Merchel, S., Braucher, R., Lachner, J. and Rugel, G., 2021. Which is the best ^{9}Be carrier for ^{10}Be/^{9}Be accelerator mass spectrometry? MethodsX, 8, 101486.

Merchel, S. and Herpers, U., 1999. An update on radiochemical separation techniques for the determination of long-lived radionuclides via accelerator mass spectrometry. Radiochimica acta, 84(4), 215-220.

Miall, A.D., 2006. The geology of fluvial deposits: Sedimentary facies, basin analysis, and petroleum geology. Springier, Berlin, 582 pp.

Minár, J., 2003. Midmountain level in the West Carpathians as tectoplain: outline of the work hypothesis. Geografický Časopis, 55(2), 141-158 (in Slovak).

Minár, J., Bielik, M., Kováč, M., Plašienka, D., Barka, I., Stankoviansky, M. and Zeyen, H., 2011. New morphostructural subdivision of the Western Carpathians: An approach integrating geodynamics into targeted morphometric analysis. Tectonophysics, 502(1–2), 158-174.

Minár, J. and Bizubová, M., 1994. Georelief evolution in southern part of Turčianska kotlina (Basin). Acta Facultatis Rerum Naturalium Universitatis Comenianae, Geographica, 35, 25-33 (in Slovak).

Moore, D.M. and Reynolds, R.C., 1997. X-ray diffraction and the identification and analysis of clay Minerals. Oxford University Press, Oxford, 1-378.

Mulder, T. and Alexander, J., 2001. The physical character of subaqueous sedimentary density flow and their deposits. Sedimentology, 48(2), 269-299.

Mulder, T., Syvitski, J.P.M., Migeon, S., Faugeres, J.C. and Savoye, B., 2003. Marine hyperpycnal flows: initiation, behavior and related deposits. A review. Marine and Petroleum Geology, 20(6-8), 861-882.

Nemčok, M. and Lexa, J., 1990. Evolution of the basin and range structure around the Žiar mountain range. Geologica Carpathica, 41, 229-258.

Nemec, W. and Kazanci, N., 1999. Quaternary colluvium in west-central Anatolia: sedimentary facies and palaeoclimatic significance. Sedimentology, 46(1), 139-170.

Nemec, W. and Postma, G., 1993. Quaternary alluvial fans in southwestern Crete: sedimentation processes and geomorphic evolution. Alluvial sedimentation, 235-276.

Nemec, W. and Steel, R.J., 1984. Alluvial and coastal conglomerates: their signifcant features and some comments on gravelly mass flow deposits. In: E.H. Koster and R.J. Steel (Eds.), Sedimentology of Gravels and Conglomerates. Memories of the Canadian Society of Petroleum Geologists, pp. 1-30.

Nesbitt, H.W. and Young, G.M., 1982. Early proterozoic climates and plate motions inferred from major element chemistry of lutites. Nature, 299(5885), 715-717.

Neubauer, T.A., Harzhauser, M. and Pipík, R., 2015. Upper Miocene endemic lacustrine gastropod fauna of the Turiec Basin: Addressing taxonomic, paleobiogeographic and stratigraphic issues. Geologica Carpathica, 66(2), 139-156.

North, C.P. and Davidson, S.K., 2012. Unconfined alluvial flow processes: Recognition and interpretation of their deposits, and the significance for palaeogeographic reconstruction. Earth-Science Reviews, 111(1), 199-223.

Novello, A., Lebatard, A.E., Moussa, A., Barboni, D., Sylvestre, F., Bourlès, D.L., Paillès, C., Buchet, G., Decarreau, A., Duringer, P., Ghienne, J.F., Maley, J., Mazur, J.C., Roquin, C., Schuster, M. and Vignaud, P., 2015. Diatom, phytolith, and pollen records from a 10 Be/ 9 Be dated lacustrine succession in the chad basin: Insight on the miocene-pliocene paleoenvironmental changes in Central Africa. Palaeogeography, Palaeoclimatology, Palaeoecology, 430, 85-103.

Ognjanova-Rumenova, N. and Pipík, R., 2015. Stratigraphic and taxonomic significance of siliceous microfossils collected from the Turiec Basin, Western Carpathians (Slovakia). Acta Botanica Croatica, 74, 345–361.

Olariu, C., Steel, R.J. and Petter, A.L., 2010. Delta-front hyperpycnal bed geometry and implications for reservoir modeling: Cretaceous Panther Tongue delta, Book Cliffs, Utah. Aapg Bulletin, 94(6), 819-845.

Paknia, M., Ballato, P., Heidarzadeh, G., Cifelli, F., Hassanzadeh, J., Vezzoli, G., Mirzaie Ataabadi, M., Ghassemi, M.R. and Mattei, M., 2021. Neogene Tectono-Stratigraphic Evolution of the Intermontane Tarom Basin: Insights Into Basin Filling and Plateau Building Processes Along the Northern Margin of the Iranian Plateau (Arabia-Eurasia Collision Zone). Tectonics, 40(3).

PANalytical, B.V., 2016. X-Pert High Score Plus Software, The Netherlands.

Paola, C., 2016. A Mind of Their Own: Recent Advances in Autogenic Dynamics in Rivers and Deltas. In: D.A. Budd, E.A. Hajek and S.J. Purkis (Eds.), Autogenic Dynamics and Self-Organization in Sedimentary Systems. SEPM Society for Sedimentary Geology, pp. 5-17.

Paseban, E., Khodabakhsh, S., Gharibreza, M., Bahiraei, N., Maleki, M. and HosseiniAsgarabadi, Z., 2018. A sedimentary model of mountainous rivers with application to Alamutrud and Shahrud rivers, N Qazvin, Iran. Arabian Journal of Geosciences, 11(24), 788.

Patruno, S. and Helland-Hansen, W., 2018. Clinoforms and clinoform systems: Review and dynamic classification scheme for shorelines, subaqueous deltas, shelf edges and continental margins. Earth-Science Reviews, 185, 202-233.

Pécskay, Z., Lexa, J., Szakács, A., Seghedi, I., Balogh, K., Konečný, V., Zelenka, T., Kovacs, M., Póka, T., Fülöp, A., Márton, E., Panaiotu, C. and Cvetković, V., 2006. Geochronology of Neogene magmatism in the Carpathian arc and intra-Carpathian area. Geologica Carpathica, 57(6), 511-530.

Pierson, T.C., 2005. Distinguishing between debris flows and floods from field evidence in small watersheds. US Geological Survey, Fact Sheet 2004-3142, DOI: 10.3133/fs20043142.

Pierson, T.C. and Costa, J.E., 1987. A rheologic classification of subaerial sediment-water flows. In: J.E. Costa and G.F. Wieczorek (Eds.), Debris Flows/Avalanches: Process, Recognition, and Mitigation. Reviews in Engineering Geology. Geological Society of America, pp. 1-12.

Pipík, R., 2002. Ostracod fauna of the Blažovce and Martin Formations (Turiec Basin). Mineralia Slovaca, 34, 105-112 (in Slovak with English abstract).

Pipík, R., 2004. Freshwater ostracods (Ostracoda) and Upper Miocene paleobiotopes of the northern part of the Turiec Depression (Slovakia). Mineralia Slovaca, 87-100 (in Slovak with English abstract).

Pipík, R., 2005. Upper Miocene freshwater ostracods (Ostracoda) of the littoral deposits of the Turiec Formation). Mineralia Slovaca, 37, 27-40.

Pipík, R. and Bodergat, A.-M., 2007. Candoninae trapézoïdales (Crustacea, Ostracoda) du Bassin de Turiec (Slovaquie) du Miocène supérieur : systématique, écologie et évolution. Geobios, 40(5), 645-676.

Pipík, R., Bodergat, A.M., Briot, D., Kováč, M., Král, J. and Zielinski, G., 2012. Physical and biological properties of the late Miocene, long-lived Turiec Basin, Western Carpathians (Slovakia) and its paleobiotopes. Journal of Paleolimnology, 47(2), 233-249.

Plašienka, D., 2003. Development of basement-involved fold and thrust structures exemplified by the Tatric–Fatric–Veporic nappe system of the Western Carpathians (Slovakia). Geodinamica Acta, 16(1), 21-38.

Plašienka, D., 2018. Continuity and Episodicity in the Early Alpine Tectonic Evolution of the Western Carpathians: How Large-Scale Processes Are Expressed by the Orogenic Architecture and Rock Record Data. Tectonics, 37(7), 2029-2079.

Plašienka, D., Grecula, P., Putiš, M., Kováč, M. and Hovorka, D., 1997. Evolution and structure of the Western Carpathians: an overview. Geological evolution of the Western Carpathians, 1-24.

Plink-Björklund, P., 2021. Distributive Fluvial Systems: Fluvial and Alluvial Fans. In: D. Alderton and S.A. Elias (Eds.), Encyclopedia of Geology (Second Edition). Academic Press, Oxford, pp. 745-758.

Postma, G., 1984. Slumps and their deposits in fan delta front and slope. Geology, 12(1), 27-30.

Postma, G. and Cartigny, M.J.B., 2014. Supercritical and subcritical turbidity currents and their deposits - A synthesis. Geology, 42(11), 987-990.

Potter, P.E., Maynard, J. and Pryor, W.A., 1980. Sedimentology of Shale. Springer Verlag, New York.

Potter, P.E., Maynard, J.B. and Depetris, P.J., 2005. Mud and Mudstones: Introduction and Overview. Springer Verlag, New York.

Pulišová, Z. and Hók, J., 2015. The palaeostress analysis of the fault rupture of the Žiarska kotlina Basin. Acta Geologica Slovaca, 7(2), 103-111.

Raisbeck, G., Yiou, F., Fruneau, M., Loiseaux, J., Lieuvin, M. and Ravel, J., 1981. Cosmogenic $^{10}Be/^{7}Be$ as a probe of atmospheric transport processes. Geophysical Research Letters, 8(9), 1015-1018.

Raiswell, R. and Berner, R.A., 1986. Pyrite and organic matter in Phanerozoic normal marine shales. Geochimica et Cosmochimica Acta, 50, 1967-1976.

Ratschbacher, L., Frisch, W., Linzer, H.G. and Merle, O., 1991. Lateral extrusion in the eastern Alps, PArt 2: Structural analysis. Tectonics, 10(2), 257-271.

Ryan, J. G., 2002. Trace-element systematics of beryllium in terrestrial materials. Reviews in Mineralogy and Geochemistry, 50(1), 121-146.

Ruszkiczay-Rüdiger, Z., Balázs, A., Csillag, G., Drijkoningen, G. and Fodor, L., 2020. Uplift of the Transdanubian Range, Pannonian Basin: How fast and why? Global and Planetary Change, 192, 103263.

Ruszkiczay-Rüdiger, Z., Fodor, L.I. and Horváth, E., 2007. Neotectonics and Quaternary landscape evolution of the Gödöllő Hills, Central Pannonian Basin, Hungary. Global and Planetary Change, 58(1–4), 181-196.

Sharma, P., Mahannah, R., Moore, W., Ku, T. and Southon, J., 1987. Transport of ^{10}Be and ^{9}Be in the ocean. Earth and Planetary Science Letters, 86(1), 69-76.

Sharma, P. and Somayajulu, B., 1982. ^{10}Be dating of large manganese nodules from world oceans. Earth and Planetary Science Letters, 59(2), 235-244.

Schildgen, T.F., Robinson, R.A.J., Savi, S., Phillips, W.M., Spencer, J.Q.G., Bookhagen, B., Scherler, D., Tofelde, S., Alonso, R.N., Kubik, P.W., Binnie, S.A. and Strecker, M.R., 2016. Landscape response to late Pleistocene climate change in NW Argentina: Sediment flux modulated by basin geometry and connectivity. Journal of Geophysical Research: Earth Surface, 121(2), 392-414.

Schmid, S.M., Bernoulli, D., Fügenschuh, B., Matenco, L., Schefer, S., Schuster, R., Tischler, M. and Ustaszewski, K., 2008. The Alpine-Carpathian-Dinaridic orogenic system: Correlation and evolution of tectonic units. Swiss Journal of Geosciences, 101(1), 139-183.

Simon, Q., Ledru, M.P., Sawakuchi, A.O., Favier, C., Mineli, T.D., Grohmann, C.H., Guedes, M., Bard, E., Thouveny, N., Garcia, M., Tachikawa, K. and Rodríguez-Zorro, P.A., 2020. Chronostratigraphy of a

1.5±0.1 Ma composite sedimentary record from Colônia basin (SE Brazil): Bayesian modeling based on paleomagnetic, authigenic $^{10}Be/^{9}Be$, radiocarbon and luminescence dating. Quaternary Geochronology, 58, 101081.

Singleton, A.A., Schmidt, A.H., Bierman, P.R., Rood, D.H., Neilson, T.B., Greene, E.S., Bower, J.A., Perdrial, N., 2017. Effects of grain size, mineralogy, and acid-extractable grain coatings on the distribution of the fallout radionuclides ^{7}Be, ^{10}Be, ^{137}Cs, and ^{210}Pb in river sediment. Geochimica et Cosmochimica Acta, 197, 71-86.

Sládek, J., Vitovič, L., Holec, J. and Hók, J., 2022. Results of the Morphotectonics and Fluvial Activity of Intramountain Basins: The Turčianska Kotlina and Žiarska Kotlina Basins, World Geomorphological Landscapes, pp. 207-233.

Sobel, E.R., Hilley, G.E. and Strecker, M.R., 2003. Formation of internally drained contractional basins by aridity-limited bedrock incision. Journal of Geophysical Research: Solid Earth, 108(7), 6-23.

Spencer, C.J., Yakymchuk, C. and Ghaznavi, M., 2017. Visualising data distributions with kernel density estimation and reduced chi-squared statistic. Geoscience Frontiers, 8(6), 1247-1252.

Starkey, H.C., Blackmon, P.D. and Hauff, P.L., 1984. The Routine Mineralogical Analysis of Clay-Bearing Samples. U. S. Geological Survey Bulletin 1563, 1-31.

Stow, D.A., 2005. Sedimentary Rocks in the Field. A Colour Guide. Manson Publishing, London, 320 pp.

Streit, R.L., Burbank, D.W., Strecker, M.R., Alonso, R.N., Cottle, J.M. and Kylander-Clark, A.R.C., 2017. Controls on intermontane basin filling, isolation and incision on the margin of the Puna Plateau, NW Argentina (~23°S). Basin Research, 29, 131-155.

Šujan, M., 2021. Klastická sedimentológia: procesy ukladania a analýza fácií. Univerzita Komenského v Bratislave, Bratislava.

Šujan, M., Aherwar, K., Braucher, R., Šarinová, K., Chyba, A., Lalinská-Voleková, B. and Vojtko, R., 2022. Data for granulometric, geochemical and authigenic $^{10}Be/^{9}Be$ geochronological analysis of Upper Miocene outcrops in the Turiec Basin, Western Carpathians (Central Europe). Mendeley Data, https://doi.org/10.17632/sdvpm9mf6m.

Šujan, M., Aherwar, K., Vojtko, R., Braucher, R., Šarinová, K., Chyba, A., Hók, J., Grizelj, A., Pipík, R., Voleková, B., Rózsová, B. and AsterTeam, submitted. Stratigraphic, sedimentological, geochemical, mineralogical and geochronological data characterizing the Upper Miocene sequence of the Turiec Basin, Western Carpathians (Central Europe). Data in Brief.

Šujan, M., Braucher, R. and ASTER, T., 2018. A test of reproducibility of authigenic beryllium extraction from clay sediment in the facility of the Dept. of Geology and Palaeontology, Comenius University in Bratislava (Slovakia). Acta Geologica Slovaca, 10(2), 165-169.

Šujan, M., Braucher, R., Chyba, A., Vlačiky, M., Aherwar, K., Rózsová, B., Fordinál, K., Maglay, J., Nagy, A., Moravcová, M. and AsterTeam, 2023. Mud redeposition during river incision as a factor affecting authigenic $^{10}Be/^{9}Be$ dating: Early Pleistocene large mammal fossil-bearing site Nová Vieska, eastern Danube Basin. Journal of Quaternary Science, 38(3), 347-364.

Šujan, M., Braucher, R., Kováč, M., Bourlès, D.L., Rybár, S., Guillou, V. and Hudáčková, N., 2016. Application of the authigenic $^{10}Be/^{9}Be$ dating method to Late Miocene–Pliocene sequences in the northern Danube Basin (Pannonian Basin System): Confirmation of heterochronous evolution of sedimentary environments. Global and Planetary Change, 137, 35-53.

Šujan, M., Braucher, R., Tibenský, M., Fordinál, K., Rybár, S. and Kováč, M., 2020. Effects of spatially variable accommodation rate on channel belt distribution in an alluvial sequence: Authigenic $^{10}Be/^{9}Be$-based Bayesian age-depth models applied to the upper Miocene Volkovce Fm. (northern Pannonian Basin System, Slovakia). Sedimentary Geology, 397, 105566.

Šujan, M., Fordinál, K., Šarinová, K., Rybár, S. and Pelech, O., 2021a. Upper Miocene colluvial and alluvial fan deposits of the Modrová Mb.: A window to palaeogeography of the Považský Inovec Mts. (Western Carpathians). Acta Geologica Slovaca, 13(1), 27-47.

Šujan, M., Kováč, M., Hók, J., Šujan, M., Braucher, R., Rybár, S. and de Leeuw, A., 2017. Late Miocene fluvial distributary system in the northern Danube Basin (Pannonian Basin System): Depositional processes, stratigraphic architecture and controlling factors of the Piešťany Member (Volkovce Formation). Geological Quarterly, 61(3), 521-548.

Šujan, M., Rybár, S., Kováč, M., Bielik, M., Majcin, D., Minár, J., Plašienka, D., Nováková, P. and Kotulová, J., 2021b. The polyphase rifting and inversion of the Danube Basin revised. Global and Planetary Change, 196, 103375.

Suhrhoff, T.J., Rickli, J., Crocket, K., Bura-Nakic, E., Vance, D., 2019. Behavior of beryllium in the weathering environment and its delivery to the ocean. Geochimica et Cosmochimica Acta 265, 48-68.

Talling, P.J., Masson, D.G., Sumner, E.J. and Malgesini, G., 2012. Subaqueous sediment density flows: Depositional processes and deposit types. Sedimentology, 59(7), 1937-2003.

Tan, S.H. and Horlick, G., 1987. Matrix-effect observations in inductively coupled plasma mass spectrometry. Journal of Analytical Atomic Spectrometry, 2(8), 745-763.

Tari, G., Arbouille, D., Schléder, Z. and Tóth, T., 2020. Inversion tectonics: A brief petroleum industry perspective. Solid Earth, 11(5), 1865-1889.

Trexler, J., Cashman, P. and Cosca, M., 2012. Constraints on the history and topography of the northeastern Sierra Nevada from a Neogene sedimentary basin in the Reno-Verdi area, Western Nevada. Geosphere, 8(3), 548-561.

Tsai, H., Maejima, Y. and Hseu, Z.-Y., 2008. Meteoric ^{10}Be dating of highly weathered soils from fluvial terraces in Taiwan. Quaternary International, 188(1), 185-196.

Tužinský, Á., Banský, V., Potyš, Z., 1967. Povodie Turca - orientačný hydrogeologický prieskum riečnych náplavov. IGHP, Žilina. Manuscript, Geofond Nr.: 18205, pp. 117 (in Slovak). Available online at: https://da.geology.sk/navigator/?desktop=Public.

Uhrin, A., Magyar, I. and Sztanó, O., 2009. Control of the Late Neogene (Pannonian s.l.) sedimentation by basement deformation in the Zala Basin. Foldtani Kozlony, 139(3), 273-282.

Utescher, T., Erdei, B., Hably, L. and Mosbrugger, V., 2017. Late Miocene vegetation of the Pannonian Basin. Palaeogeography, Palaeoclimatology, Palaeoecology, 467, 131-148.

van Dam, J.A., 2006. Geographic and temporal patterns in the late Neogene (12–3 Ma) aridification of Europe: The use of small mammals as paleoprecipitation proxies. Palaeogeography, Palaeoclimatology, Palaeoecology, 238(1–4), 190-218.

Van Dijk, M., Postma, G. and Kleinhans, M.G., 2009. Autocyclic behaviour of fan deltas: an analogue experimental study. Sedimentology, 56(5), 1569-1589.

Van Dine, D.F., 1985. Debris flows and debris torrents in the Southern Canadian Cordillera. Canadian Geotechnical Journal, 22(1), 44-68.

von Blanckenburg, F. and Bouchez, J., 2014. River fluxes to the sea from the ocean's ^{10}Be/^{9}Be ratio. Earth and Planetary Science Letters, 387, 34-43.

von Blanckenburg, F., O'nions, R., Belshaw, N., Gibb, A. and Hein, J., 1996. Global distribution of beryllium isotopes in deep ocean water as derived from Fe-Mn crusts. Earth and Planetary Science Letters, 141(1-4), 213-226.

Wei, W. and Algeo, T.J., 2020. Elemental proxies for paleosalinity analysis of ancient shales and mudrocks. Geochimica et Cosmochimica Acta, 287, 341-366.

Willenbring, J.K. and von Blanckenburg, F., 2010. Meteoric cosmogenic Beryllium-10 adsorbed to river sediment and soil: Applications for Earth-surface dynamics. Earth-Science Reviews, 98(1-2), 105-122.

Wittmann, H., von Blanckenburg, F., Bouchez, J., Dannhaus, N., Naumann, R., Christl, M. and Gaillardet, J., 2012. The dependence of meteoric ^{10}Be concentrations on particle size in Amazon River bed sediment and the extraction of reactive ^{10}Be/^{9}Be ratios. Chemical Geology, 318, 126-138.

Wysocka, A., Łoziński, M., Śmigielski, M., Czarniecka, U. and Bojanowski, M., 2018. New data on the age of the sedimentary infill of the Orava-Nowy targ basin - A case study of the Bystry stream succession (Middle/upper Miocene, Western Carpathians). Geological Quarterly, 62(2), 327-343.

Yawar, Z. and Schieber, J., 2017. On the origin of silt laminae in laminated shales. Sedimentary Geology, 360, 22-34.

Yokoyama, Y., Guichard, F., Reyss, J.-L. and Van, N.H., 1978. Oceanic residence times of dissolved beryllium and aluminum deduced from cosmogenic tracers ^{10}Be and ^{26}Al. Science, 201(4360), 1016-1017.

Zbořil, L., Šefara, J. and Halmešová, S., 1985. Geofyzikálny výskum Turčianskej kotliny, čiastková záverečná správa. Manuscript, Geofond Nr.: 60638, pp. 29 (in Slovak). Available online at: https://da.geology.sk/navigator/?desktop=Public.